

Design of a Multi-Array Radio-Frequency Coil for Interventional MRI of the Female Breast

by

Peter J. Serano

A Master's Thesis

Submitted to the Faculty

of the

WORCESTER POLYTECHNIC INSTITUTE

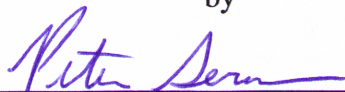
in partial fulfillment of the requirements for the

Degree of Master of Science

in

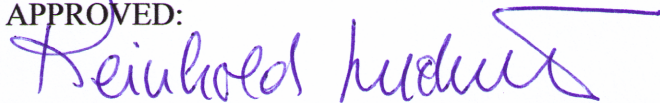
Electrical and Computer Engineering

by



April 16, 2009

APPROVED:



Prof. Reinhold Ludwig, PhD, Thesis Advisor
ECE Department, Worcester Polytechnic Institute



Prof. Sergey Makarov, PhD, Committee Member
ECE Department, Worcester Polytechnic Institute



Prof. Craig Ferris, PhD, Committee Member
Northeastern University

Abstract

A new method for the simulation of radio frequency (RF) coils has been developed. This method utilizes the FEM simulation package Ansoft HFSS as a base for the modeling of RF coils with complex biological loading effects. The abilities of this software have been augmented with custom MATLAB code to enable the fast prediction of lumped element values needed to properly tune and match the coil structure as well as to perform the necessary post processing of simulation data in order to quickly generate and evaluate field data of the resonating coil and compare design variations. This method was evaluated for accuracy and implemented in the re-design of an existing four channel breast coil array for clinical imaging of the female breasts.

Based on the simulation results, a commercially viable printed circuit board (PCB) implementation was developed and tested in a clinical 1.5 T MR scanner. The new design allows for wide open bilateral access to the breast regions in order to accommodate various interventional procedures. The layout has also increased axillary B_1 field coverage with minor penalty to the signal-to-noise ratio of the coil array, enabling high-resolution imaging over a wide field-of-view.

Acknowledgments

I would like to first thank my advisor Prof. Reinhold Ludwig for giving me the opportunity to work as a Research Assistant in the RF and Medical Imaging Laboratory at WPI and for the opportunity to work on this project. I am also grateful for all of his time given to bestow to me his extensive knowledge of RF coil and circuit design that guided me through this thesis.

Next, I would like to thank Prof. Sergey Makarov for noticing my academic potential in my senior year at WPI, and whose recommendation helped me to receive funding for my graduate education as a Teaching Assistant during my first year of study. I am also grateful to him for the introduction and extensive training of the Ansoft simulation tools, and his guidance and expertise in developing my simulation models and methodology.

I would also like to thank Dr. Craig Ferris and Dr. Jean King of InsightMRI for funding my thesis work and the amazing job opportunity I have received at InsightMRI.

Many thanks are due to all of my colleagues at InsightMRI; Mathew Brevard for his extensive knowledge of the world of MRI and for his time running the test scans and analysis of that data for my prototype coil; Rosti Lemdiasov for all of his time and many insights into the development of my simulation methodology and his extensive programming skills; Steven Toddes for his time and expertise in developing and building the coil housing used for my prototype; and Bill Nastri for his expertise in advising me on the proper techniques of circuit and coil construction.

Finally, I would like to thank my family for all of the love, support, and encouragement they've given me throughout my life.

Table of Contents

Abstract.....	i
Acknowledgments	ii
Table of Contents	iii
List of Figures.....	v
List of Tables	vii
1 Introduction.....	1
1.1 Medical Imaging.....	1
1.2 Thesis Objectives.....	2
2 Background Research.....	3
2.1 Clinical MRI Systems	3
2.1.1 Main Magnet	6
2.1.2 Gradient Coils	7
2.1.3 RF Transmit Coil	8
2.1.4 RF Receive Coils	8
2.1.5 RF Power Amplifiers	9
2.1.6 MR Console	9
2.1.7 Pulse Sequencing.....	9
2.2 Previous Coil Design.....	10
2.3 New Mechanical Former	12
2.4 Circuit Design.....	15
2.4.1 Resonant Coil Structure.....	15
2.4.2 Preamplifiers and Active Detune Circuitry.....	18
2.4.3 Passive Detune Circuitry and Fuses.....	20
2.4.4 Baluns.....	22
2.5 Interfacing with the Siemens 1.5T Clinical Scanner.....	23
3 Simulation Methodology	25
3.1 Overview	25
3.2 Coil Structure Modeling in HFSS	29
3.2.1 Creating Models.....	29
3.2.2 Defining Structure Parameters.....	31
3.2.3 Defining Simulation Parameters	37
3.2.4 Running and Monitoring Simulations	39
3.3 Human Body Load Modeling.....	41
3.3.1 Augmenting the Model	42
3.3.2 Dielectric and Conductivity Data	44
3.4 Circuit Modeling with MATLAB.....	45
3.4.1 Circuit Modeling	45
3.4.2 Matlab S-Parameter Accuracy	50
3.4.3 Modifying the HFSS Solution with Circuit Data from MATLAB.....	53
3.4.4 HFSS Field Data Accuracy	55
3.5 Generating Array Field Data.....	57
3.6 Analyzing Simulation Results	60
3.6.1 B1 Field and SNR.....	60
3.6.2 Surface Current Density.....	61

3.6.3	Axillary Field Coverage.....	62
3.6.4	Quadrature Field Performance	63
4	Simulation Models	66
4.1	Prototype Simulation	66
4.1.1	HFSS Model.....	66
4.1.2	Simulation Results	69
4.1.3	S-Parameters	70
4.1.4	Field Data.....	71
4.2	New Design Simulation.....	75
4.2.1	HFSS Model.....	75
4.2.2	Simulation Results	77
4.2.3	S-Parameters	78
4.2.4	Field Data.....	79
4.3	Simulation Results	83
4.3.1	B1 Field Strength Comparison	83
4.3.2	Axillary Coverage Comparison	84
4.3.3	Quadrature Performance Comparison.....	85
5	Prototype Construction	86
5.1	PCB Design	86
5.2	Construction	88
5.3	Bench Testing and Parameter Recording.....	89
6	Results	91
6.1	Measured SNR Data	91
6.1.1	Prototype Coil.....	91
6.1.2	New Coil Design	91
6.2	Comparing Simulation to Measured Data.....	92
7	Conclusion	93
7.1	Summary.....	93
7.2	Further Research	94
8	Bibliography	95
Appendices.....		97
Appendix A: Issues found with the HFSS Lumped RLC Boundary		97
Appendix B: Human Body Model Datasets.....		105
Appendix C: Simulation Power Scaling Values		108

List of Figures

Figure 2.1: Clinical 1.5T MRI Scanner.....	3
Figure 2.2: MRI System Block Diagram.....	5
Figure 2.3: Magnetic Field Gradient for an Image Slice.....	7
Figure 2.4: Coil Configuration.....	10
Figure 2.5: Coil Placement on Body.....	10
Figure 2.6: Ring Mode Current Flow I_0	10
Figure 2.7: Strap Mode Current Flow I_1	10
Figure 2.8: Four Channel Prototype Design.....	11
Figure 2.9: Single Ring-Strap Coil Prototype.....	11
Figure 2.10: Dual Ring-Strap Coil Prototype.....	11
Figure 2.11: New Mechanical Former Which Meets Clinical Specifications.....	12
Figure 2.12: Interventional Grid Accessory Placement.....	13
Figure 2.13: CAD Model of New Coil Structure.....	13
Figure 2.14: New Mechanical Former Dimensions – Top View.....	14
Figure 2.15: New Mechanical Former Dimensions – Side View.....	14
Figure 2.16: Simplified Coil Circuit Schematic.....	15
Figure 2.17: Complete Coil Circuit Schematic.....	17
Figure 2.18: Preamp PCB Schematic with Active Detune Circuit.....	19
Figure 2.19: Passive Detune Circuit and Fuse Schematic.....	21
Figure 2.20: (a) Cable Trap Balun, (b) PCB Balun.....	22
Figure 2.21: Siemens MAGNATOM Symphony 1.5T Clinical MRI Scanner.....	23
Figure 2.22: Siemens Symphony Connector Interface.....	24
Figure 3.1: HFSS GUI Interface.....	26
Figure 3.2: Simulation Method Block Diagram.....	28
Figure 3.3: Object Command Window.....	31
Figure 3.4: Object Properties Window.....	32
Figure 3.5: Design Properties Window.....	32
Figure 3.6: Defining a Lumped Port.....	34
Figure 3.7: Defined Radiation Boundary Encompassing the Coil Structure.....	35
Figure 3.8: Material Properties Window.....	36
Figure 3.9: Simulation Setup Window.....	38
Figure 3.10: HFSS Solver Options Window.....	39
Figure 3.11: Simulation Validation Check Window.....	39
Figure 3.12: Solution Data Window.....	40
Figure 3.13: Ansoft Human Body Model.....	41
Figure 3.14: Human Body Model with Added Breasts.....	42
Figure 3.15: Human Body Model used for Simulation.....	43
Figure 3.16: Dimensions of Augmented Breasts.....	43
Figure 3.17: Relative Dielectric Constant of Fat vs. Frequency.....	44
Figure 3.18: Single Loop Surface Coil.....	45
Figure 3.19: Coil and Lumped Element Interconnections, Port Definitions.....	46
Figure 3.20: Lumped Element Terminations and S-Matrices.....	46
Figure 3.21: Single Loop Coil Model.....	50
Figure 3.22: Coil Loop Circuit Schematic.....	50

Figure 3.23: Single Point S-Parameter Approximation	51
Figure 3.24: Ansoft Designer Circuit Schematic.....	52
Figure 3.25: MATLAB vs. Ansoft Designer S-Parameter Comparison	52
Figure 3.26: HFSS Edit Sources Window.....	53
Figure 3.27: Single Loop Coil Model.....	55
Figure 3.28: Comparison of Theoretical vs. Simulated Value of the B Field	56
Figure 3.29: Example Individual Field Plots per Channel.....	59
Figure 3.30: Example Combined Array Field Plot	59
Figure 3.31: Calculated Surface Current Density and Expected Current Flow.....	61
Figure 3.32: Human Axilla.....	62
Figure 3.33: B1 Field on the Surface of the Human Body Model.....	62
Figure 3.34: Vector Plots of the Magnetic Field within the ROI.....	63
Figure 3.35: Example Quadrature Field Difference Plot	65
Figure 4.1: Creating the HFSS Model of the Existing Prototype	67
Figure 4.2: Completed HFSS Model of Existing Prototype	68
Figure 4.3: Mesh Plots of the Prototype Simulation	69
Figure 4.4: S-Parameters of the Prototype Coil Array	70
Figure 4.5: Prototype Coil – Surface Current Density per Channel.....	71
Figure 4.6: Prototype Coil – B1 Field per Channel – Transverse Plane.....	72
Figure 4.7: Prototype Coil – Combined B1 Field – Transverse Plane	72
Figure 4.8: Prototype Coil – B1 Field on the Surface of the Body	73
Figure 4.9: Prototype Coil – Quadrature Combined Field Increase.....	74
Figure 4.10: Former CAD Model used as a Basis for HFSS Model Building	75
Figure 4.11: HFSS Model of the New Coil Design	76
Figure 4.12: Completed HFSS Model with Human Body Load	76
Figure 4.13: Mesh Plots of the New Design Simulation.....	77
Figure 4.14: S-Parameters of the New Coil Design.....	78
Figure 4.15: New Coil Design – Surface Current Density per Channel	79
Figure 4.16: New Coil Design – B1 Field per Channel – Transverse Plane	80
Figure 4.17: New Coil Design – Combined B1 Field – Transverse Plane.....	80
Figure 4.18: New Coil Design – B1 Field on the Surface of the Body	81
Figure 4.19: New Coil Design – Quadrature Combined Field Increase	82
Figure 4.20: B1 Field Comparison – Transverse Plane.....	83
Figure 4.21: Axillary Coverage Comparison.....	84
Figure 4.22: Quadrature Field Comparison.....	85
Figure 5.1: Main PCB Layout.....	86
Figure 5.2: Strap PCB Layout	86
Figure 5.3: Manufactured Main PCB	87
Figure 5.4: Manufactured Strap PCB.....	87
Figure 5.5: Building the New Design Prototype.....	88
Figure 5.6: S-Parameters of the Two Adjacent Ring Channels.....	89
Figure 5.7: S-Parameters of the Left Ring and Strap Channels.....	90
Figure 0.1: Defined Lumped Element Boundary	97
Figure 0.2: Initial Simulation Strategy Block Diagram	99
Figure 0.3: HFSS Frequency Sweep Results	100
Figure 0.4: MATLAB Frequency Sweep Results.....	101

Figure 0.5: Ansoft Designer Circuit Schematic.....	102
Figure 0.6: Ansoft Designer Simulation Result – Single Frequency Point	102
Figure 0.7: Ansoft Designer Simulation Result – Frequency Sweep.....	103
Figure 0.8: Convergence Comparison of Simulation Methods.....	104
Figure 0.9: Relative Dielectric Constant of Fat vs. Frequency	105
Figure 0.10: Conductivity of Fat vs. Frequency	105
Figure 0.11: Relative Dielectric Constant of the Heart vs. Frequency	106
Figure 0.12: Conductivity of the Heart vs. Frequency	106
Figure 0.13: Relative Dielectric Constant of Muscle vs. Frequency.....	107
Figure 0.14: Conductivity of Muscle vs. Frequency	107

List of Tables

Table 2.1: Gyromagnetic Ratio of Common Nuclei.....	6
Table 4.1: Simulation Data of Prototype Design.....	69
Table 4.2: Simulation Data for the New Coil Design.....	77
Table 4.3: B1 Field Strength Comparison – Prototype vs. New Coil Design	83
Table 6.1: Prototype Coil Scan Results.....	91
Table 6.2: New Design Scan Results.....	91
Table 6.3: Simulation and Measured Data Summary	92

1 Introduction

1.1 Medical Imaging

Medical imaging has evolved over the years to become a standard of care in clinical medicine for the diagnosis of various diseases and ailments from broken bones to cancer detection. “Seeing” inside the human body is necessary to aid physicians in performing many interventional medical procedures such as guided biopsy that otherwise could not have been completed in the past. Medical imaging is also used extensively in medical research applications for both human and animal research from learning about how the brain functions to the effectiveness of new drugs being developed.

There are a variety of imaging methods that are based on different scientific principles such as X-Ray, Ultrasound, and Magnetic Resonance Imaging (MRI), all with advantages and disadvantages in diagnosing particular illnesses or studying the human body. X-Ray technology is most often used for the imaging of calcified tissue, as it can achieve the optimal imaging resolution of 128 shades of grey for bone imaging. [1]

X-Ray is also the basis of Computed Tomography (CT), an algorithm that makes use of multiple X-Ray projections that are digitally processed to form 3D images. Ultrasound is also another widely used imaging modality with many applications. Besides the more commonly known use in obstetric imaging, ultrasound is also used for soft tissue imaging of cardiac, renal, and liver tissues as well as muscular-skeletal imaging of muscles, ligaments and tendons. [2]

This thesis focuses on the topic of the design and simulation of an RF receive coil array for use within MRI systems. Unlike CT, MRI uses no ionizing radiation, but instead uses a powerful magnetic field to align the nuclear magnetization of hydrogen atoms in water in the body. Radiofrequency pulses are used to systematically alter the alignment of this magnetization, causing the hydrogen nuclei to produce a rotating magnetic field detectable by the scanner. This signal can be manipulated by additional magnetic fields to build up enough information to construct an image of the body. [3]

1.2 Thesis Objectives

This thesis aims to address a precise and efficient numerical modeling approach to arrive at a new RF coil configuration suitable for breast imaging. This includes the ability to model complex coil geometries and heterogeneous and lossy biological tissue interactions in 3D and at high frequencies. This modeling approach also takes into account circuit design parameters such as lumped element components and their effect on the structure's electromagnetic field simulations.

Based on these theoretical model predictions, additional thesis objectives were established to address the engineering aspects of designing and constructing a clinical MRI coil. This encompasses the electromagnetic and circuit simulations of the design, the development of a PCB layout that is made for a newly designed coil housing, and the interfacing of the system to a clinical Siemens 1.5T Scanner.

2 Background Research

2.1 Clinical MRI Systems

A clinical MRI scanner is a complex system encompassing many aspects of science and engineering. These clinical systems include many large components, requiring approximately 25 square feet of space in order to house all of the necessary electrical and mechanical components that comprise the system. A typical clinical MRI system is shown in Figure 2.1. The major external components are utilized by the patient and technician, which are the magnet bore, patient table and external controls. The magnet bore is the large access in the center of the MRI system. The patient lies on a patient table which will slide into the magnet bore. The position of this table in the scanner is controlled by a technician operating the controls located on the exterior of the machine.



Figure 2.1: Clinical 1.5T MRI Scanner [4]

Figure 2.2 shows a block diagram of typical MRI system components. Enclosed in the box in the upper half of the figure are the components that are housed in what is known as the magnet room. This includes the main magnet and all of the coils. This room is shielded to provide isolation from all of the outside electromagnetic energy that could cause interference with the magnetic fields or RF signals used inside the MRI system. Outside this box are the components used to generate signals and to control the MRI system. This includes the amplifiers used to generate the high power signals used for the gradient and RF transmit coils, as well as those for amplifying the received RF signal from the RF receive coils. Also included is the digitizer used as an Analog-to-Digital (A/D) converter employed to convert the analog received RF pulses to digital information that can be processed by the computer system. Along with processing the received RF signals into image data, the computer system is used to orchestrate the function of the entire MRI system. The following sections will explore more in depth the functions of the main magnet, gradient coil system, RF coils, RF amplifiers and the MR computer system.

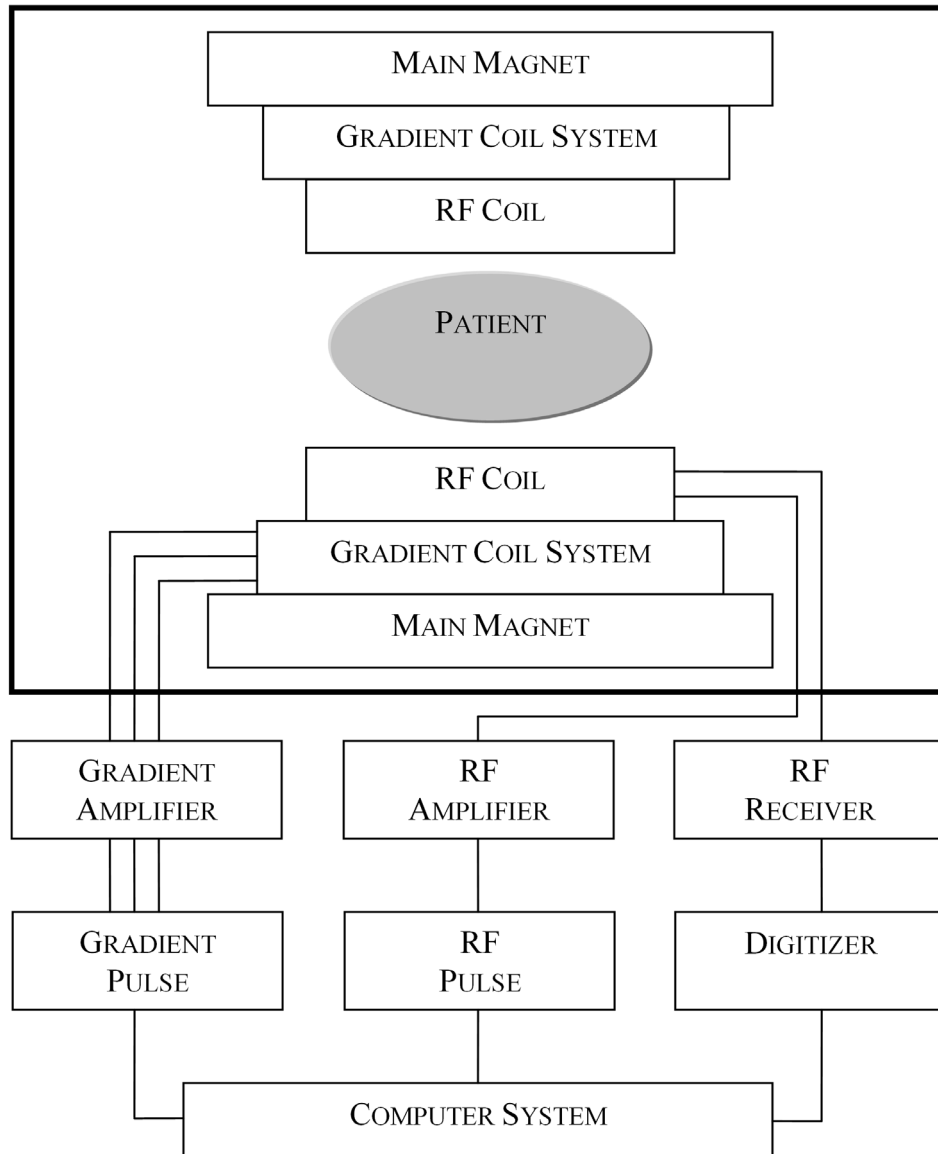


Figure 2.2: MRI System Block Diagram [5]

2.1.1 Main Magnet

The main magnet is the source of the static magnetic field known as the B_0 field. Typical clinical magnets have field strengths of 1.5 or 3.0 Tesla (T), while special magnets for scientific research can be as strong as 11.7T. Typical main magnets are nitrogen super cooled electromagnets, while low strength magnets (<1T) are usually permanent magnets. For this project, the RF coil will be used in conjunction with a Siemens 1.5T Clinical System.

The main magnet field strength is integral in determining the RF frequency that all of the RF coils in the system will be designed for. Determining this frequency is the first design parameter one must determine to begin to design a RF coil. The equation used to find this frequency is known as the Larmor Equation and is defined as:

$$f_0 = \frac{\gamma}{2\pi} \cdot B_0 \quad (2.1)$$

where f_0 is the RF frequency in MHz, B_0 is the strength of the main magnetic field in Tesla, and γ is the gyromagnetic ratio. The gyromagnetic ratio is a constant that can be derived for a particular atomic nucleus using classical physics. Table 2.1 lists the most common types of nuclei used in MRI.

Table 2.1: Gyromagnetic Ratio of Common Nuclei [6]

Nucleus	Gyromagnetic Ratio ($\frac{\text{MHz}}{\text{T}}$)
1H	267.51
^{17}O	36.26
^{23}Na	70.76

Using Table 2.1 and (2.1), one can calculate the frequency needed for an RF coil for the most commonly imaged nuclei, hydrogen in a $B_0 = 1.5T$ MRI system. This results in an RF frequency of 63.87MHz. In reality magnetic strengths are often not exactly accurate as advertised. For the Siemens 1.5T clinical scanner, the field strength is actually 1.495T. To this end a RF frequency of 63.65MHz will be used as the solution frequency for all electromagnetic and circuit simulations, as well as the frequency that all prototype coils will be tuned and matched.

2.1.2 Gradient Coils

In order to provide spatial information from the MR signal, as well as to control the active imaging slice, the main magnetic B_0 field is modified through a spatial gradient field. This means that the B field in the bore of the magnet will only be equal to B_0 for a small length along a given axis within the bore. In Figure 2.3, the magnetic gradient G_z is plotted along the z axis along with a patient for illustrative purposes. The active imaging slice will be the area defined by $B_0 \pm G_z z$ and thus the nuclei of the tissue in this region will be exposed to the proper magnetic field strength that correlates to the Larmor frequency that the RF receive coil is tuned.

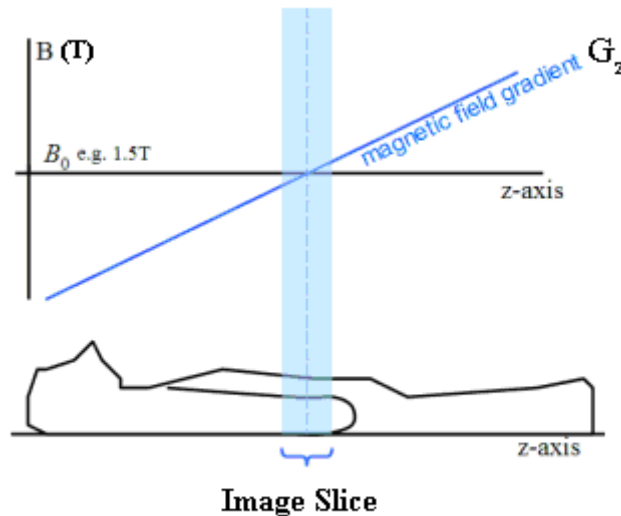


Figure 2.3: Magnetic Field Gradient for an Image Slice [7]

The MRI system uses a set of 3 orthogonal gradient coils, one for each axis, known as the G_x , G_y , and G_z coils, thus spatial gradients of the main magnetic field may be applied in the X, Y, and Z axes within the bore of the MRI magnet. Gradient strength is expressed in units of field strength per length, for example, $10 \frac{\mu T}{cm}$, which means that the magnetic field changes by $10 \mu T$ over each centimeter [8].

2.1.3 RF Transmit Coil

This coil, traditionally a volume coil that is most often built into the main magnet bore of the MRI system, is used for the transmission of RF energy into the subject. The frequency of this RF pulse is determined by the Larmor equation, so that the energy in the RF pulse can be absorbed by the spinning nuclei and thus alter their alignments. When the RF pulse is turned off, the atoms will begin to return to their aligned state with the main magnetic field. As these nuclei return to their originally aligned state, they emit energy, which can be received as an induced voltage signal by the RF receive coil. The induced coil voltage forms the basis of this Nuclear Magnetic Resonance (NMR) signal. [9]

2.1.4 RF Receive Coils

After the energy has been transmitted and absorbed by the nuclei of the subject, the nuclei will begin to re-align itself with the main magnetic field. As they do, they emit energy at the same Larmor frequency, and the time varying flux induces a voltage in the RF receive coil.

There are two general types of RF receiving coils, volume and surface coils. Volume coils have coil element configurations with long conductors spaced around a cylindrical structure. They are known for their extremely high field homogeneity, but because of their size, they do not have as high a Signal-to-Noise Ratio (SNR) as a typical surface coil given the same imaging ROI. Surface coils on the other hand, are known for their typically high SNR, but lower field homogeneity and field of view than a volume coil. [10]

2.1.5 RF Power Amplifiers

Powerful amplifiers are required to produce an RF signal used to modify the alignment of the nuclei being imaged. The amplifiers power the RF transmit coil in order to produce a strong homogenous B1 field. Typical clinical MR scanners transmit approximately 10 kW into their large body RF coil which is housed within the bore.

2.1.6 MR Console

All of the hardware components of the MRI system are controlled by the main MRI console. Typically this task is done using a dedicated PC running specialized software to interface with the MRI hardware. It is here that the proper signals are generated for particular imaging sequences as well as the processing of data being received by the RF coils to create the images used for diagnoses.

2.1.7 Pulse Sequencing

One major advantage of MRI over other imaging modalities is the use of different pulse sequences used to excite the nuclei within the body via the gradient and RF transmit coils. This allows for the control of what types of tissue parameters to accentuate or hide in order to enhance diagnoses. For example pulse sequences can be designed to null out fatty tissue of the breast in order to better view the internal blood vessels. Pulse sequences are comprised of various types of sinc function pulses, most commonly known as “90 degree” and “180 degree” pulses that are used to modify the flip angle of the nuclei imaged by 90 or 180 degrees. It is the time duration of these signals that determines the flip angle. The combination of these pulses and time delay between these multiple 90 and 180 degree pulses create a pulse sequence. There are many types of pulse sequences such as the spin echo, gradient echo, and inversion recovery. The spin echo sequence is the most commonly used sequence as it can be used to quickly produce a wide variety of images that accentuate or null the desired tissue being imaged.

2.2 Previous Coil Design

One of the goals of this thesis is to apply the newly developed simulation technique to re-design an existing four channel breast coil array which was developed as part of a PhD thesis at Worcester Polytechnic Institute (WPI) [11]. This design features dual ring and strap coil loops which conform to the female breast. A single pair of ring and strap loops can be seen in Figure 2.4 and its placement on the body is seen in Figure 2.5. This ring-strap design is covered under US Patent 7084630.

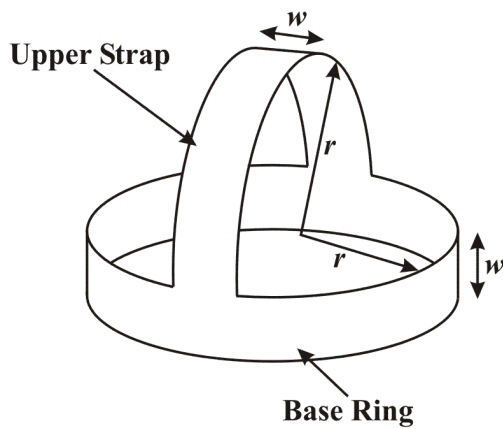


Figure 2.4: Coil Configuration

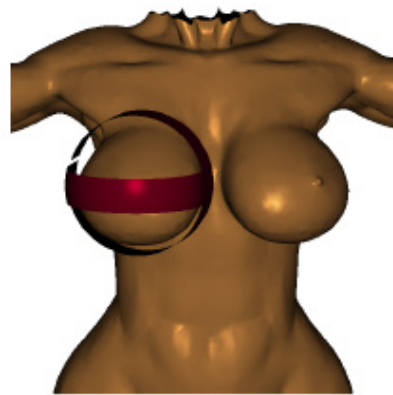


Figure 2.5: Coil Placement on Body

Figure 2.6 shows the general current flow for the ring channel; for this loop, current only flows around the base ring. Figure 2.7 shows the current flow for the strap channel. For this loop, current flows through the upper strap, splits across the base ring and recombines back into the upper strap.

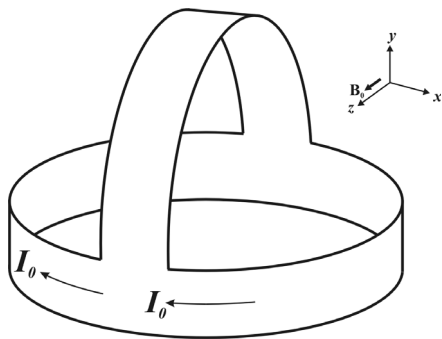


Figure 2.6: Ring Mode Current Flow I_0

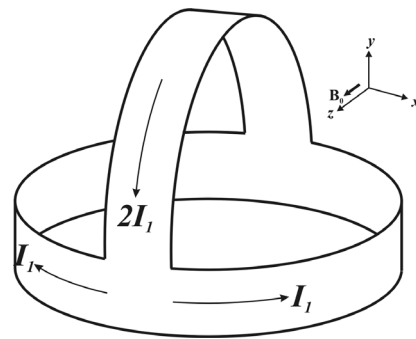


Figure 2.7: Strap Mode Current Flow I_1

Two pairs of these ring-strap coil loops will be used to create four independent receive channels that are combined by the MR console to enable a larger image field of view without drop in SNR. A CAD model of the configuration can be seen in Figure 2.8. Channels are defined as Left Ring: Ch. 1, Left Strap: Ch. 2, Right Ring: Ch. 3, and Right Strap: Ch. 4.

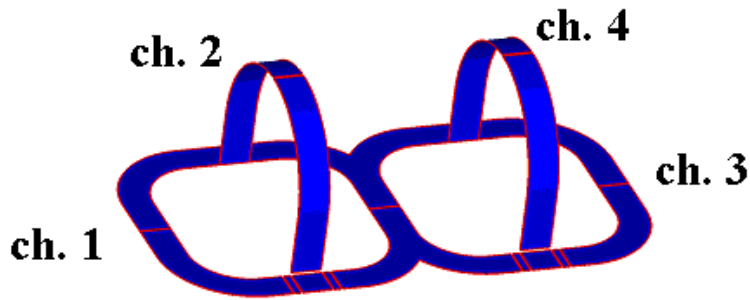


Figure 2.8: Four Channel Prototype Design

A complete prototype was built by Aghogho Obi under sponsorship by InsightMRI. Figure 2.9 shows a single ring-strap pair. Figure 2.10 shows a four channel receive array comprised of two ring-strap loop pairs. The four channel design is interfaced to a Siemens 1.5T clinical scanner. The goal of this thesis is to use new modeling tools as developed in Section 3 to redesign and optimize this four channel array to fit into a new ergonomic former for improved patient comfort and professional appearance, while maintaining electrical and imaging performance.



Figure 2.9: Single Ring-Strap Coil Prototype



Figure 2.10: Dual Ring-Strap Coil Prototype

2.3 New Mechanical Former

The main constraint on the new coil design is a new ergonomic housing; see Figure 2.11, used to provide improved patient comfort and to maximize access for interventional equipment. The strap loops, previously implemented with copper tape, have been replaced with more rigid copper tubes that will connect to a smaller PCB in the base of the former for each strap. These copper tubes are placed inside four support structure legs. This design can also support up to 1300lbs of weight in accordance with IEC 60601 standards. The new design still features the open access available for the breasts.

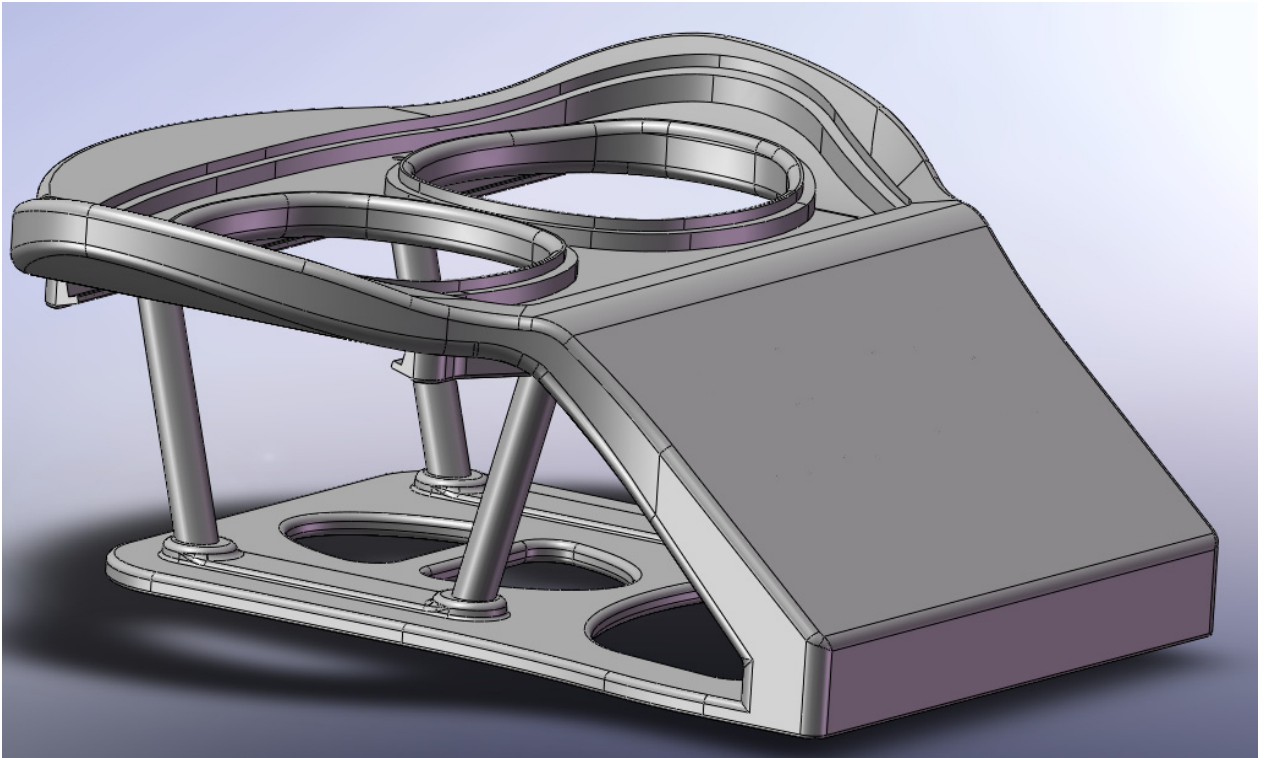


Figure 2.11: New Mechanical Former

This design also features the necessary mechanical features to attach special accessories known as “interventionals”, seen in Figure 2.12 , which are special plastic grids that can be placed in the open space parallel with the breast to aid the physician with biopsy procedures.

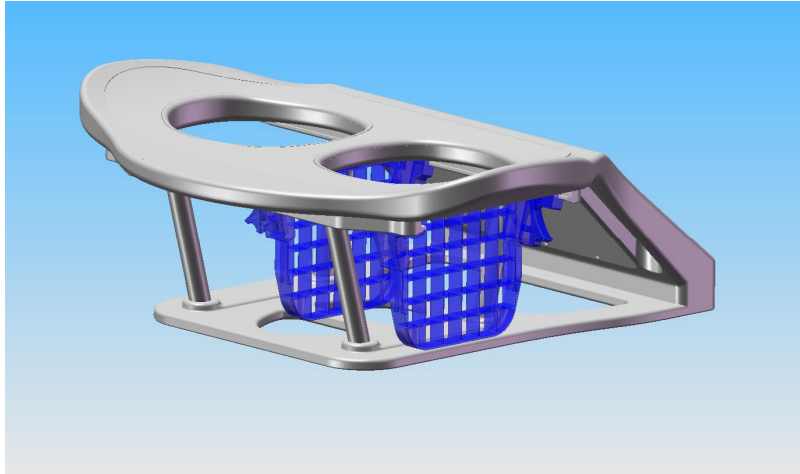


Figure 2.12: Interventional Grid Accessory Placement

The new coil topology is the same as the original prototype; the major differences are mechanical in order to fit the new former. Dimensions for the new PCB, coil loops and strap tubes are determined by the free space available within the new former.

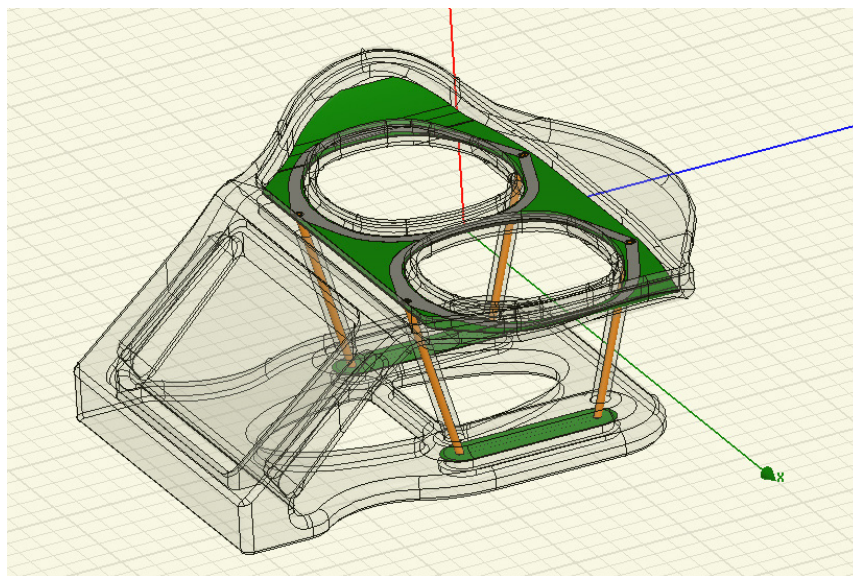


Figure 2.13: CAD Model of New Coil Structure

Dimensions for the new coil former reported in Figure 2.11 to Figure 2.13 can be seen in Figure 2.14 and Figure 2.15.

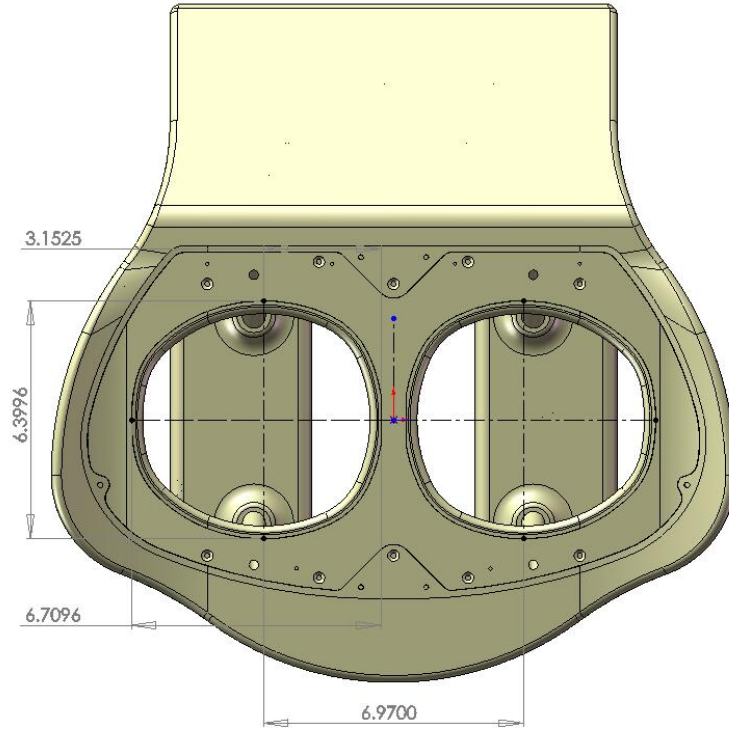


Figure 2.14: New Mechanical Former Dimensions – Top View

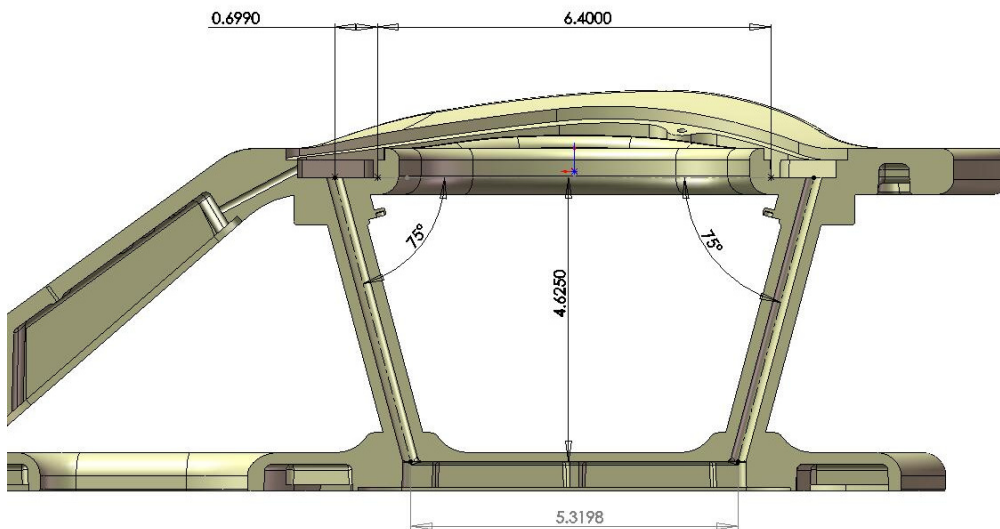


Figure 2.15: New Mechanical Former Dimensions – Side View

2.4 Circuit Design

2.4.1 Resonant Coil Structure

A simplified circuit schematic can be seen in Figure 2.16. This structure is that of Figure 2.8. The two largest loops (those containing capacitors C_1 , C_2 , and C_3), comprise the two ring loops. The traces running down the centers of each of these two loops (those containing capacitors C_4 and C_5) are the conductors that comprise the strap loops.

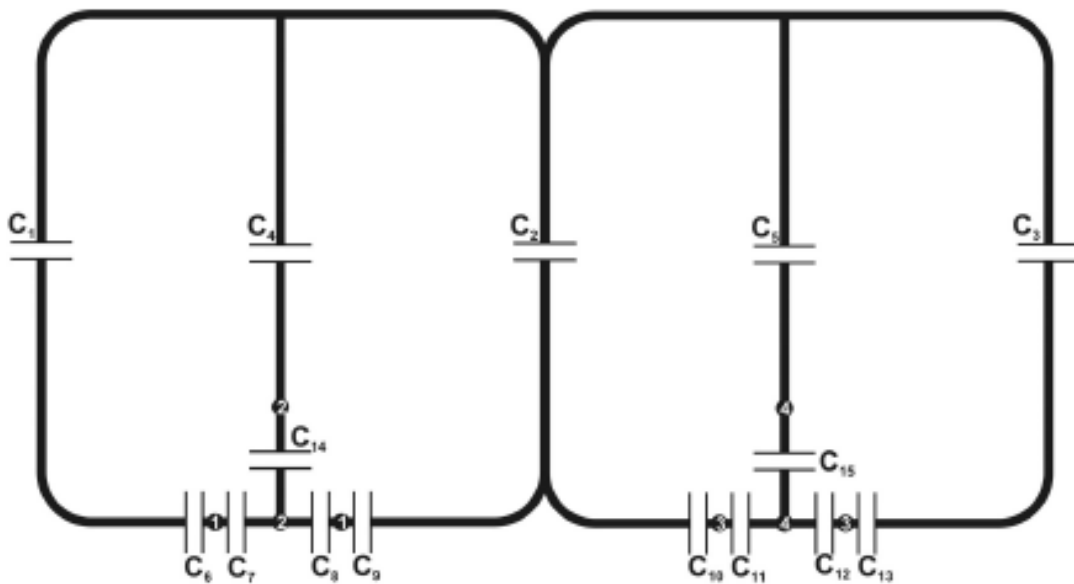


Figure 2.16: Simplified Coil Circuit Schematic

The output ports are labeled with black dots, numbered 1 – 4. There are two black dots for each port that specify which two points comprise the output port voltage. It is from these four ports that the signals for each channel will be output to the preamplifiers and then the MR console. Not shown in Figure 2.16 are the matching inductors placed in series after the port output used in each channel to complete the output matching network. A complete circuit schematic can be seen in Figure 2.17.

The various capacitors distributed around the loops are employed for three purposes. There are capacitors used for decoupling, tuning, and matching. Capacitors C_1 , C_2 , and C_3 are used for decoupling. Decoupling is done to ensure that currents from one channel are not flowing in any other so that each channel may simultaneously operate independently from another. Capacitor C_2 decouples the two adjacent base ring loops, while C_1 and C_3 help to decouple the ring channels from the strap channels. These capacitors are chosen so that they resonate with the inductance of the adjacent loops to create a high impedance path between adjacent channels for isolation. Decoupling in this manner is known as “Capacitive Decoupling”. These capacitors should be the same value to ensure a proper balance of decoupling between both ring channels.

Capacitors are employed for tuning and matching. Tuning capacitors are used to adjust the resonant frequency of the coil structure to the proper Larmor frequency, while matching capacitors are used to match the impedance of the coil to allow maximum signal reception. Capacitors C_4 and C_5 adjust the tuning of the strap channels, while C_6 , C_9 , C_{10} , C_{11} adjust the tuning of the ring channels. Capacitors C_{14} and C_{15} function as matching capacitors for the strap channels, and C_7 , C_8 , C_{11} , C_{12} function as matching capacitors for the ring channels. The actual values for these capacitors will be determined later after the EM simulation has been completed.

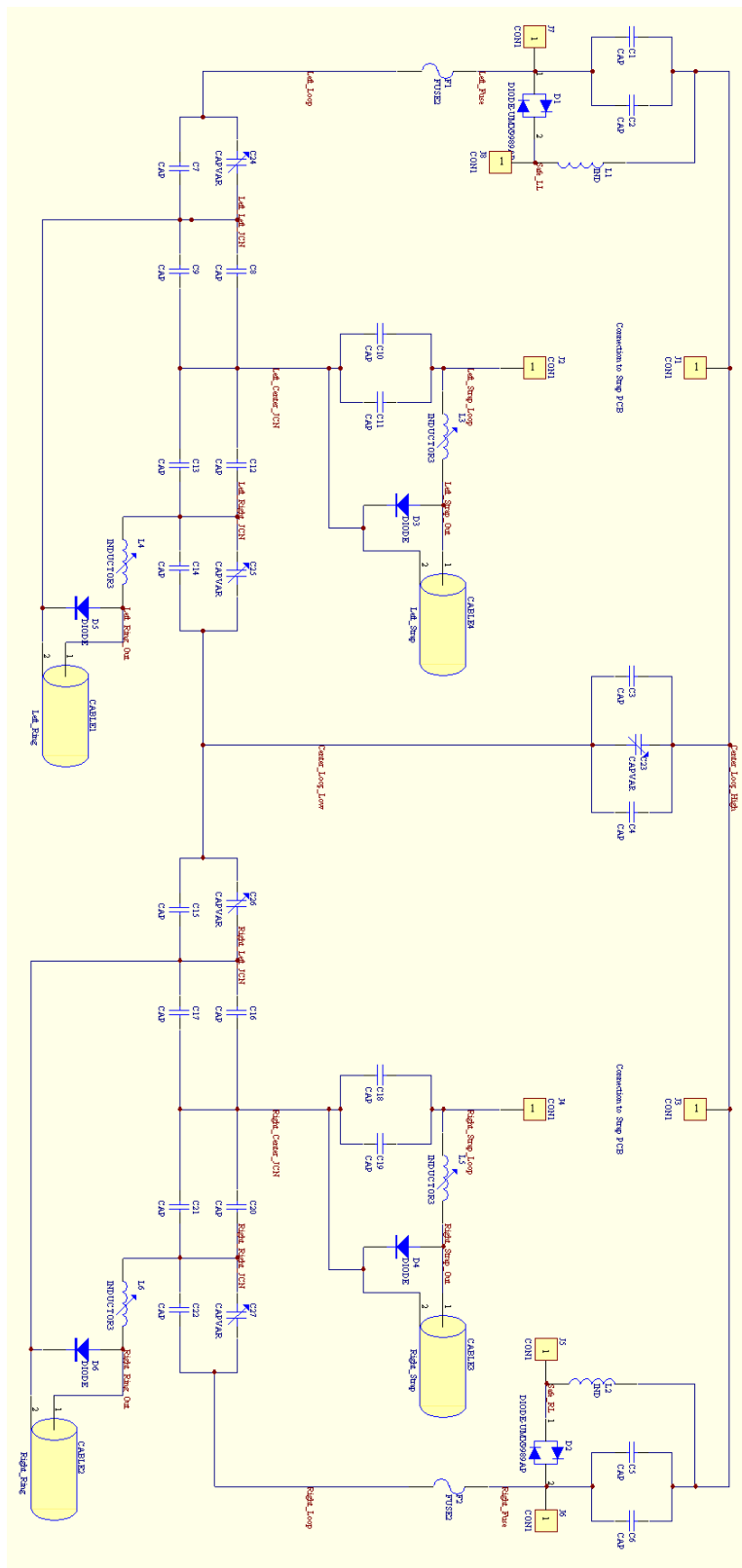


Figure 2.17: Complete Coil Circuit Schematic

2.4.2 Preamplifiers and Active Detune Circuitry

Each of the four channels are terminated into a preamplifier circuit used to boost the received signal to levels required by the MR console to process the data. The preamplifiers used in this design are specially made for use in MR systems. The MicroWave Technology MPH Series preamp contains nonmagnetic components and can provide a gain of 25dB at 63.6 MHz. It is also able to operate by utilizing the DC voltage and current provided by the MR console. Unlike an average low frequency amplifier, where it is desirable to have very high input impedance, or an average RF amplifier where it is desirable to have a 50Ω input impedance, these amplifiers have much lower complex input impedance, typically $Z_{in} = 1.5 - j0.5\Omega$. This low input impedance is used for a decoupling technique known as “Preamp Decoupling”. In preamp decoupling, the low input impedance of the preamplifiers forces the majority of the currents in each respective channel to be drawn by the preamp. This minimizes the ability of the current to flow into adjacent channels.

This circuit, seen in Figure 2.18, also includes the active detune circuitry. Active detune circuitry is used to turn each channel on or off. The active detune is necessary because every coil in the receive array must be detuned when the high power RF transmit signal is generated by the external RF transmit coil. If the coil were to be tuned during the transmit phase, damage could occur to the coil since it is designed only to receive the low power NMR signal generated by the nuclei of the subject returning to their aligned state with the static magnetic field.

The main component of the active detune circuit is the PIN diode D1. This diode is different from a typical PN junction diode, as it has an additional semiconductor layer called the “Intrinsic” layer. At RF frequencies the PIN diode can be used as a variable resistance and thus is used as a switch. When the PIN diode is reversed biased with a -30V “PIN Bias” voltage from the MR console, it acts as an open circuit. When the PIN diode is forward biased, it acts as a short, causing the LC output matching network described in the previous section to resonate with high impedance.

Other components in this circuit include inductors L1 and L2, and Capacitor C2, which create a low pass filter for the DC PIN Bias voltage. Capacitor C1 is utilized to block the DC PIN voltage from the input of the preamp. Inductor L3 and capacitor C3 are used to filter RF from the DC power input to the preamp. Anti-parallel diode pair D2 is employed as an additional safety measure to prevent damage to the preamplifier in case high currents are present at the input.

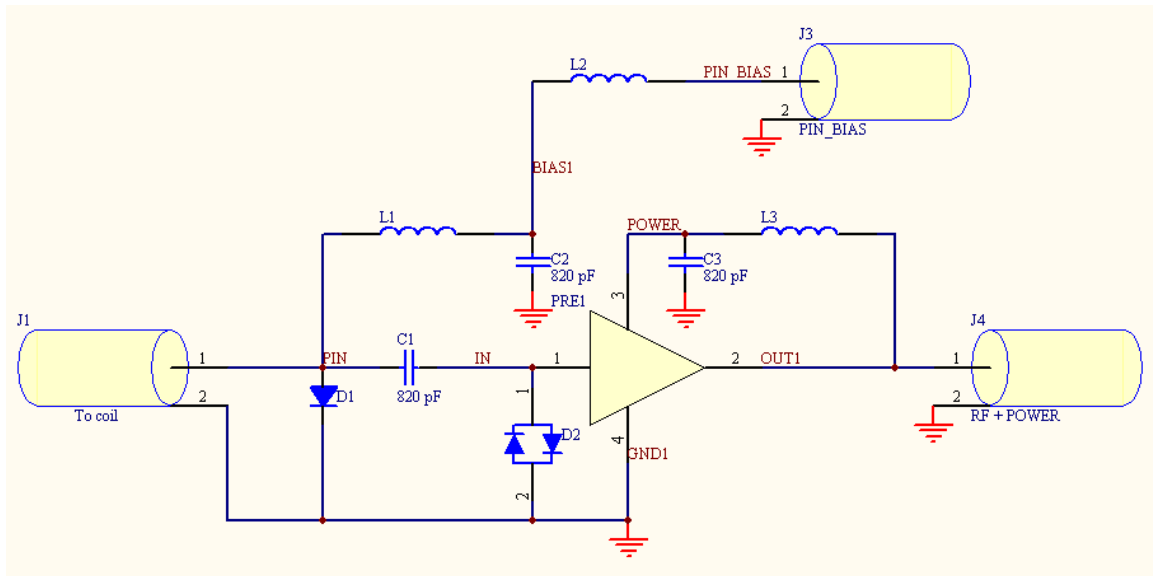


Figure 2.18: Preamp PCB Schematic with Active Detune Circuit

2.4.3 Passive Detune Circuitry and Fuses

The existing circuit design was also augmented to include the necessary features for safety. Passive detune circuits and fuses are added onto each channel. Passive detune circuits are used for the same purpose as active detune circuits, to detune the coil so that it is not resonating. The difference here is that passive detune circuits are uncontrolled by the MR Console and are used as a safety mechanism that is transparent to the end user as well as self-regulating, in that it is only activated when currents are too high and can return to normal operation after currents are reduced. Anti-parallel diodes are used in conjunction with a parallel LC circuit. If currents in the coil become too high, the diodes will create a short, allowing the LC circuit to resonate at the Larmor frequency and create high impedance and thus stop the receiving action of the coil. The capacitors used in this circuit are existing capacitors that are used for decoupling in the ring channels, and the tuning capacitors of the strap channels. For example, shown in Figure 2.19, is a passive detune circuit comprised of L_1 and D_1 added around the existing capacitors C_1 and C_2 which are the decoupling capacitors for the left ring loop.

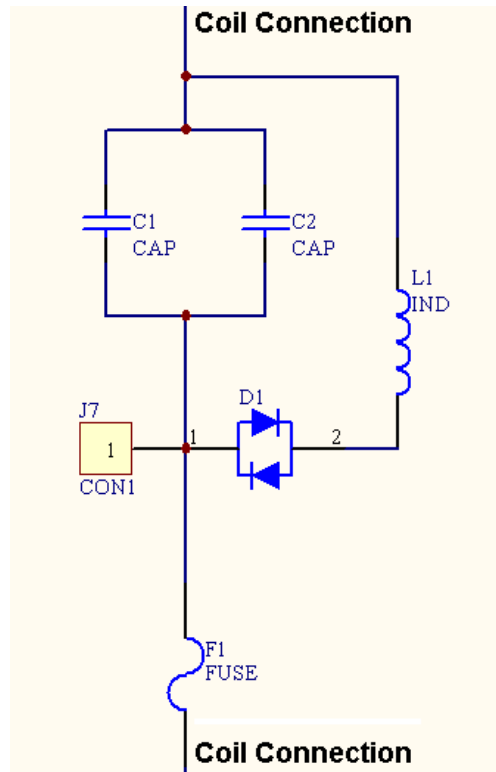


Figure 2.19: Passive Detune Circuit and Fuse Schematic

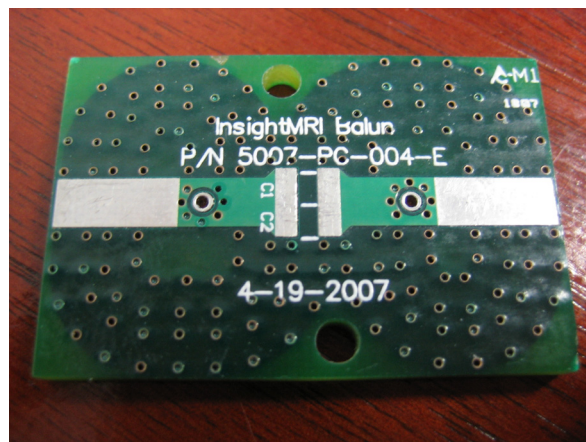
Along with the passive detune circuitry; fuses are used to physically break the coil loop if currents become too high. These fuses are made by Siemens and required for all clinical coil designs. These safety features are necessary to reduce risk of electrical shock for the safety of the patient as well as to prevent damage to the coil components.

2.4.4 Baluns

Two different baluns are used in the design. The term “balun” is a combination of the words balanced and unbalanced, as the function is to convert signals that are balanced or differential to those that are unbalanced or single ended, or vice-versa. The balun helps to improve performance of the receiver coils by providing a high impedance path for common-mode currents induced by noise on the shields of the coaxial transmission lines. A cable trap balun, seen in Figure 2.20a, is used on the cable connecting the coil to the MR scanner. This main cable contains all four coaxial lines for each channel. The cable balun is used to force currents to flow on the inner side of each coaxial cable’s shield. The balun’s cylindrical structure creates an inductance which is then terminated by capacitors to cause high impedance for RF currents at the Larmor frequency. Forcing the currents to flow on the inside of the coaxial cable shields adds resilience to noise that could couple from other signals. A cable trap balun is required for every 40cm of cable length as per Siemens clinical coil requirements. Each channel also has its own PCB Balun positioned directly after the output of the preamplifier. The PCB Balun, seen in Figure 2.20b, is also used to force shield currents to flow on the inside of the coaxial cable for each channel. These Baluns also add another layer of protection to the patient from high voltage shock due to exposed cable shields.



(a) Cable Trap Balun



(b) PCB Balun

Figure 2.20: Cable Trap and PCB Balun

2.5 Interfacing with the Siemens 1.5T Clinical Scanner

The coil designed in this thesis will be interfaced with a Siemens MAGNATOM Symphony 1.5T clinical scanner, shown in Figure 2.21. This MRI system allows for the acquisition of up to four RF channels of MR data. The coil will be interfaced using the Siemens Symphony Receive Connector seen in Figure 2.22. It is a 20 pin connector that is similar in dimensions to the standard D-SUB-25 connector but with an additional coaxial pin in the center for high power RF signal transmission.

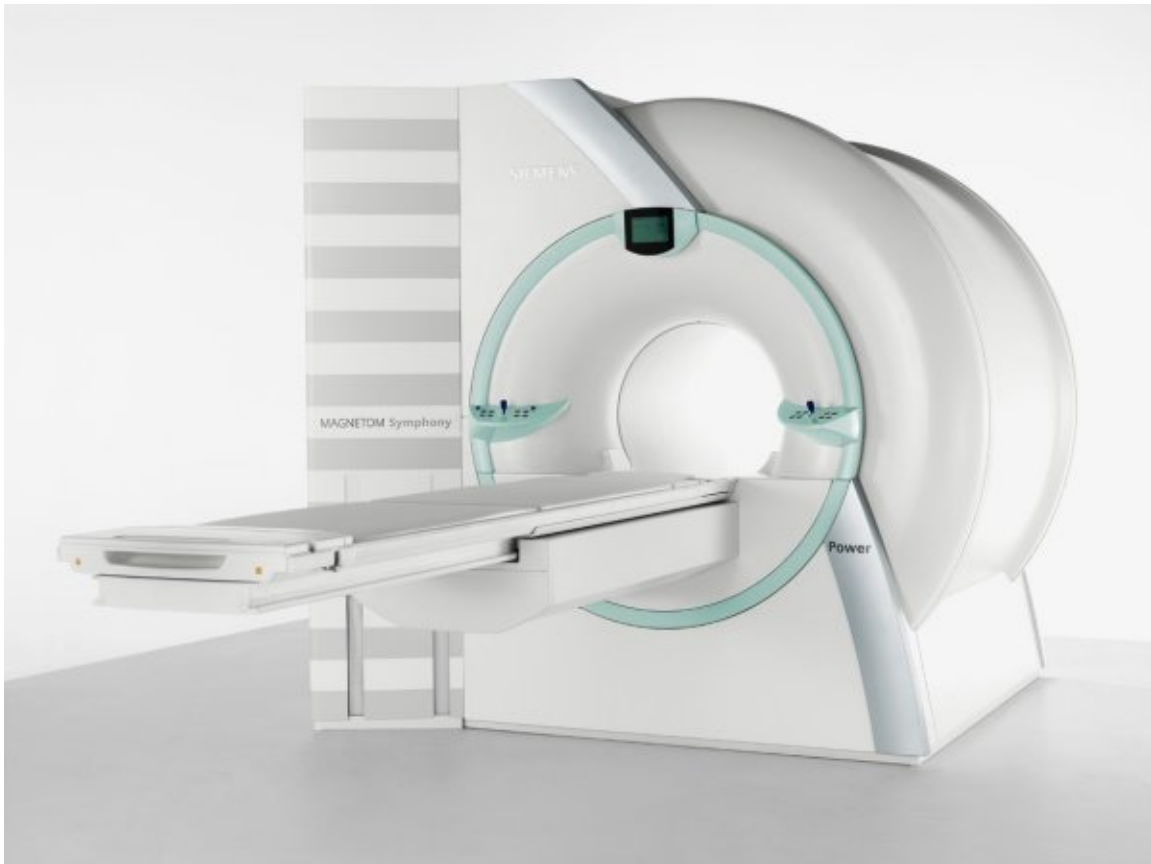


Figure 2.21: Siemens MAGNATOM Symphony 1.5T Clinical MRI Scanner [12]

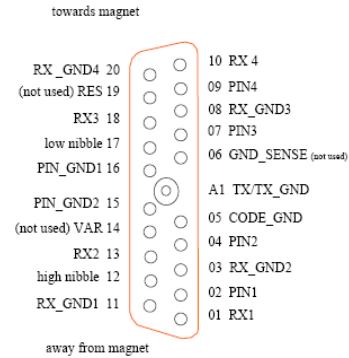
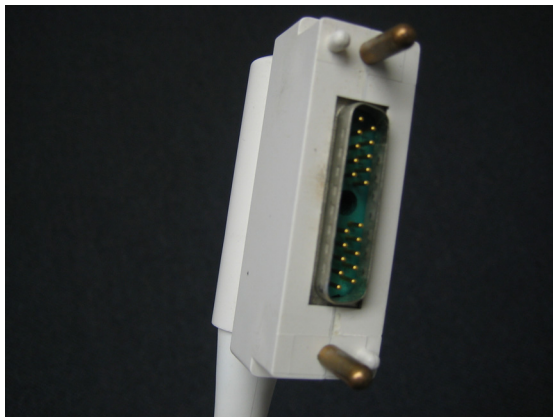


Figure 2.22: Siemens Symphony Connector Interface

There are four RF receive channels (RX 1:4) each includes 10VDC with a maximum current of 70mA superimposed on each receive channel to power the preamplifiers of the coil array. Furthermore, there are 4 PIN Bias signals (PIN 1:4) that are used to actively tune or detune each loop of the coil array as per the imaging sequence. These PIN Bias pins provide either a voltage of -30VDC to reverse bias the PIN diodes, or a current of 100mA to forward bias the PIN diodes. The final connections are known as “Coil Codes”. A Coil Code consists of two hexadecimal digits that are used by the MR console to automatically identify the make and model of the coil being used. Each hexadecimal digit is used to represent a resistor value. Coil codes are set through 3 pins that are comprised of a simple voltage divider. The first resistor in the voltage divider is known as the “high nibble” or coil code 1, and the second resistor is known as the “low nibble” or coil code 2. For the design, a coil code of ‘29’ was assigned by Siemens for this four channel coil array.

3 Simulation Methodology

3.1 Overview

It is desirable to simulate the performance of this new design prior to construction. The use of Electronic Design and Automation (EDA) software to optimize the design parameters and evaluate performance is necessary for rapid prototyping of a given design so that only one physical prototype needs to be built.

The first part of the simulation method involves solving for the so-called scattering, or S-Parameters and 3D field data of the geometrical coil structure at the Larmor frequency. To accomplish this task, a commercial electromagnetic simulation tool was chosen. This allows for a more detailed and reliable analysis. The software chosen for the simulation was the finite element solver Ansoft HFSS v10.1. HFSS has a full CAD style GUI seen in Figure 3.1, and has the ability to import 3D CAD models from industry standard CAD packages like Pro-Engineer and Solidworks. HFSS also features an adaptive meshing algorithm to more efficiently mesh the structure, thus increasing accuracy and decreasing simulation time and computational resources. Another advantage to using HFSS is the availability of a complete human body model. The Ansoft human body model package contains three full human body models, with varying degrees of detail. Each model contains a complete set of organs, including frequency dependant characteristics of conductivity and relative dielectric constant for each individual type of tissue. [13] More details on the human body model can be seen in Section 3.3. One particular goal of this project is to utilize the human body model to simulate in more detail the coverage area of the coil as well as the loading effects of various internal tissues in the chest.

The most important aspect of using Ansoft HFSS is the ability to model full 3D structures on all scales from the human body to the thickness of the copper traces used in the coil loops. This is specifically critical for RF coil designs to more accurately simulate the resistance of the structure of the coil. This allows for more accuracy when comparing the performance of multiple designs since the resistance of a coil loop is related to the strength of the magnetic field generated by the coil, and thus related to the SNR and overall performance of the coil.

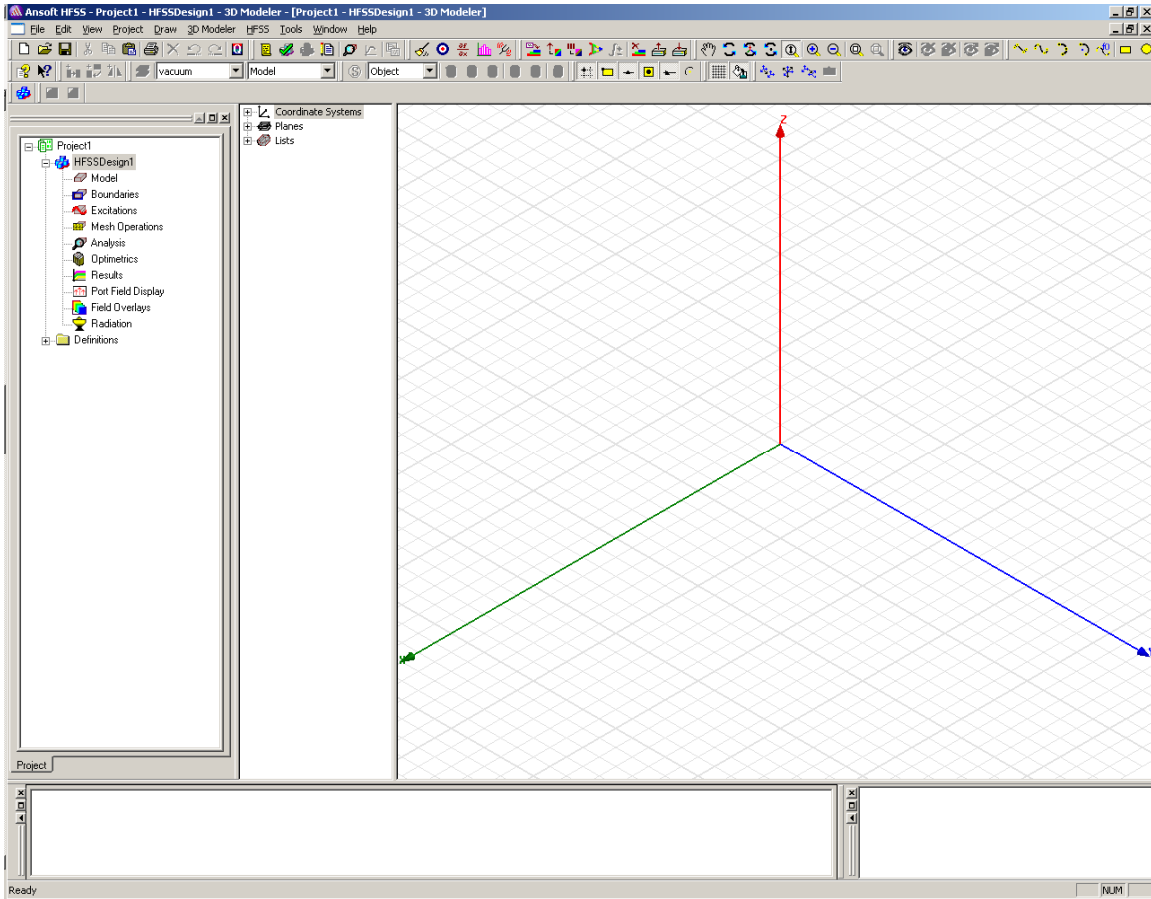


Figure 3.1: HFSS GUI Interface

Along with 3D field data, the HFSS simulation computes an $N \times N$ S-Matrix at the Larmor frequency where the size N of the matrix is determined by the number of generalized ports which represent breaks in the coil where lumped elements will be placed. This data will be used in the next step of the simulation method to determine the proper lumped element values used in terminating these ports to form the complete model of the resonating structure so that the field data of the resonating coil may be obtained.

The next part of the simulation involves modeling the circuit aspects of the coil. While HFSS is used to model the coil geometry and 3D field data, this data must be processed to include the effects of the lumped element components in the design to optimally tune and match the coil. This is done using custom MATLAB scripts to process the S-Parameter data from HFSS. The MATLAB scripts allow for the rapid evaluation of lumped element component choice so that the proper capacitor and inductor values can be chosen to best tune, match and decouple each channel of the coil array. This is an iterative process where the lumped element values are adjusted in the code and the S-Parameters of each of the four channels are recomputed. The process repeated and is done when all four channels are properly tuned matched and decoupled. At this point all lumped element values have been determined and the real S-Parameters of the four channel system are generated.

The final step in the simulation method is to import the data generated by the MATLAB scripts into HFSS in order to modify the field solution data so that the desired field data of the tuned, matched, and decoupled resonating coil array can be generated to evaluate the performance of the coil design. HFSS includes the ability to re-calculate the field data of the structure based on how each port is driven with a given amount of complex power. In the initial HFSS simulation, the field data is solved by exciting each port individually with 1W of incident power while the remaining ports are terminated with 50Ω impedances. Using this knowledge, a MATLAB script is used to compute a new set of complex power values which are then used to drive each of the N ports of the HFSS simulation in order to mimic the effect of terminating those N ports with the calculated lumped elements from the resonating simulation model from MATLAB. It is in this way that the original field solution from HFSS is “power scaled” in order to generate new field data of a coil array that is now tuned, matched, and decoupled to the levels set with the lumped elements determined using the first MATLAB script. A block diagram summarizing the simulation method can be seen in Figure 3.2.

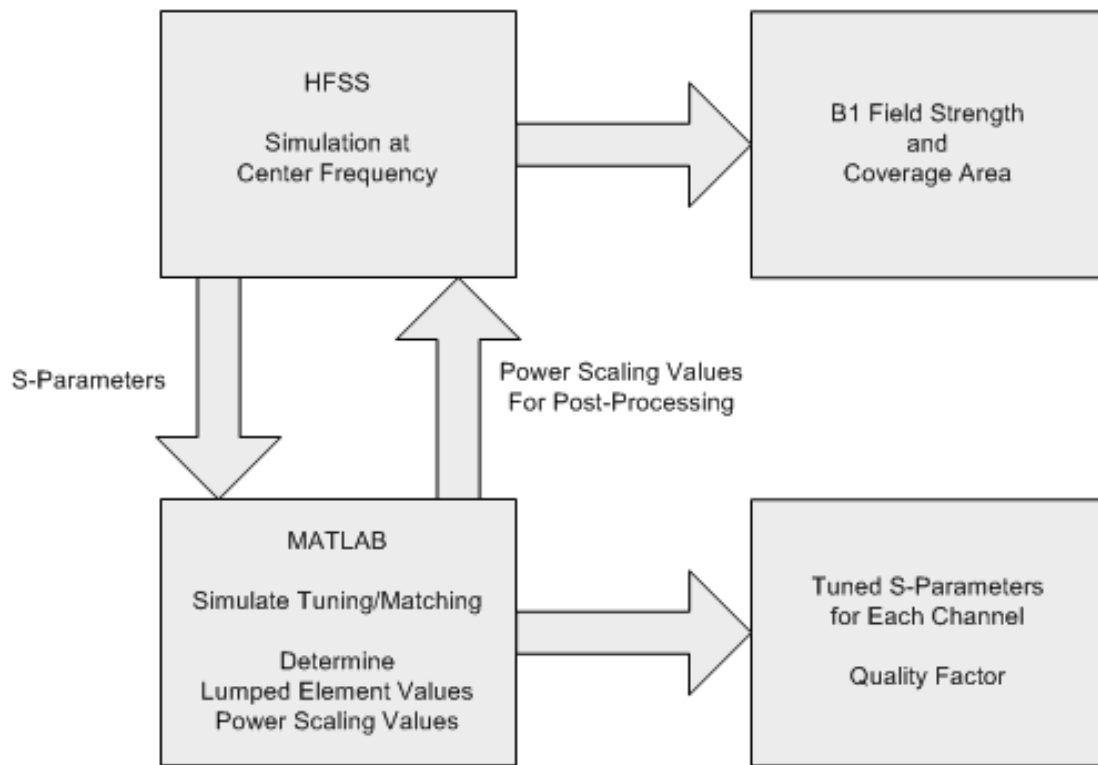


Figure 3.2: Simulation Method Block Diagram

3.2 Coil Structure Modeling in HFSS

3.2.1 Creating Models

3.2.1.1 Parameterized Design

HFSS has a built-in CAD modeling system that is based on the ACIS geometry modeling engine. Generic 2D and 3D geometries such as rectangles, circles, polygons, boxes, spheres, and cylinders can be created and assigned parameters that are linked to a central database of variables. For example, when a cylinder is created, the position, height and radius of the cylinder can all be assigned different variables. These variables can then be used in defining other structure geometries, so that they are linked by a single common variable.

Building models by parameterization is the optimal way to create models in HFSS. In this way, a single variable can be changed that will modify multiple geometries at the same time. Parameterized models also have the ability to link any parameter to a design optimization, allowing multiple simulation runs to be done at once to see which design parameter achieves optimal results. Another advantage to parameterized models is that they are created within HFSS's ACIS geometry system. Thus, they are much less likely to encounter meshing errors during simulation than models imported from other commercial CAD packages.

3.2.1.2 CAD Import

While parameterized models are the best way to build structures in HFSS, often times it is easier and more time efficient to import an existing model from a commercial CAD package such as Solidworks or Pro-Engineer. Complex 3D models containing splines and curves that cannot easily be modeled with regular primitive geometries, like cubes and cylinders, should be imported to save time and retain structure information that would be lost when approximating complex surfaces with regular geometries. PCB models can also be imported from a 2D drawing such as a DWG or DXF file. In this case HFSS will automatically assign a variable for the thickness of each 2D layer in order to extrude the model into a 3D object. HFSS has a variety of tools to aid the user in working with imported models. A built-in analysis and “healing” tool is available to find and remove small features such as screw holes, chamfers and fillets that are not electrically important to the design.

While HFSS can import a variety of industry standard CAD model formats such as STEP, IGES, and STL just to name a few, it is best to export the model from Solidworks or Pro-Engineer as an ACIS v14 (.SAT) file. Since HFSS 10 uses the ACIS v14 geometry engine, all other types of geometries imported will be converted to this file format. Through experience in working with imported objects, the built-in CAD conversion that HFSS will do to non-ACIS models can be time consuming and error prone. It is best to export the model from Solidworks or Pro-Engineer as an ACIS v14 (.SAT) file.

3.2.2 Defining Structure Parameters

3.2.2.1 Object/Draw Commands

Each object created will have its own command for creating the part. The specific commands depend on each particular geometry type. The example shown below in Figure 3.3 shows the creation of a cylinder. Included parameters that must be specified are center position, axis, radius, and height. Note how they are all given variable names as is the parameterized modeling methodology of HFSS. Later on, the variables can be accessed under the “Design Properties” window shown in Figure 3.5.

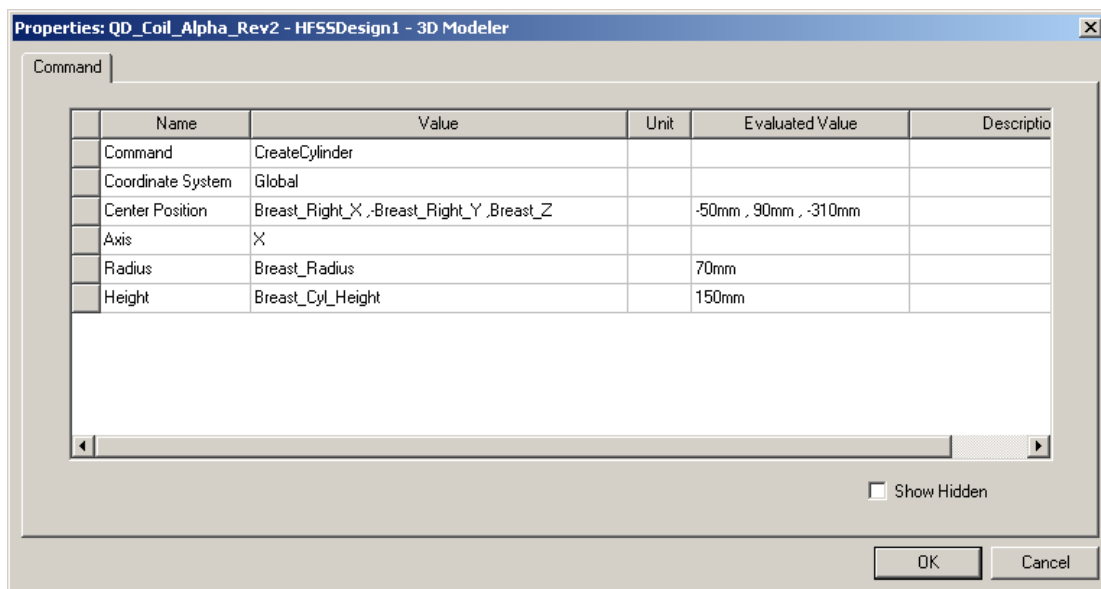


Figure 3.3: Object Command Window

3.2.2.2 Object Properties

Every object that is created or imported has visual and simulation properties. Visual properties include the object name, material, color, and transparency. These properties do not affect the simulation results, only how they appear in the model. Simulation properties include “Solve Inside” and “Model”. When creating an object these options are enabled by default. By un-checking the “Solve Inside” box, HFSS will not mesh this inside of a structure and only its boundary. By un-checking the “Model” box, the object will be ignored in the simulation and will be placed into the “Non Model” portion of the project tree.

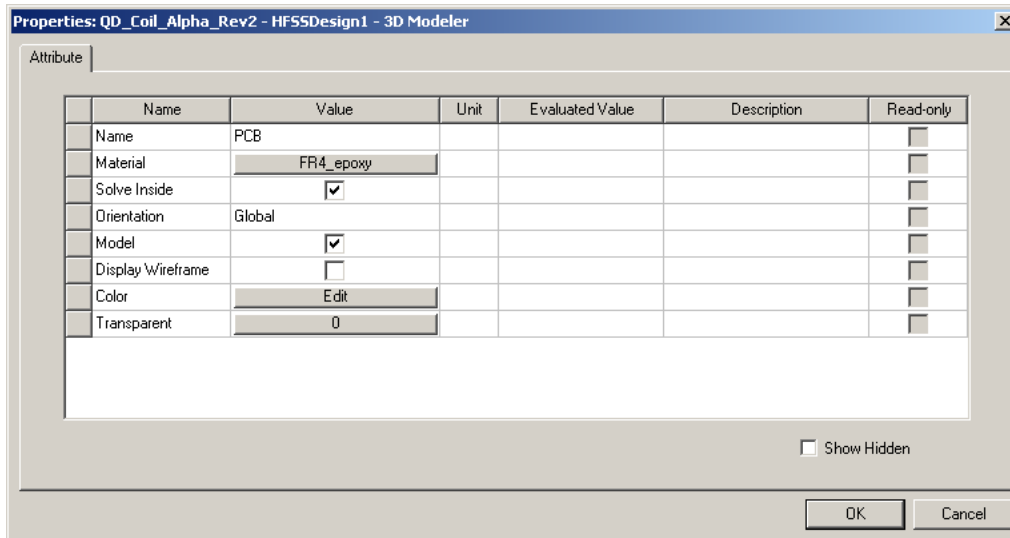


Figure 3.4: Object Properties Window

3.2.2.3 Design Properties

The Design Properties window is where all the variables are managed. It can be accessed under the HFSS menu, and then selecting “Design Properties”. This window is where all variables can be modified to change model geometry parameters.

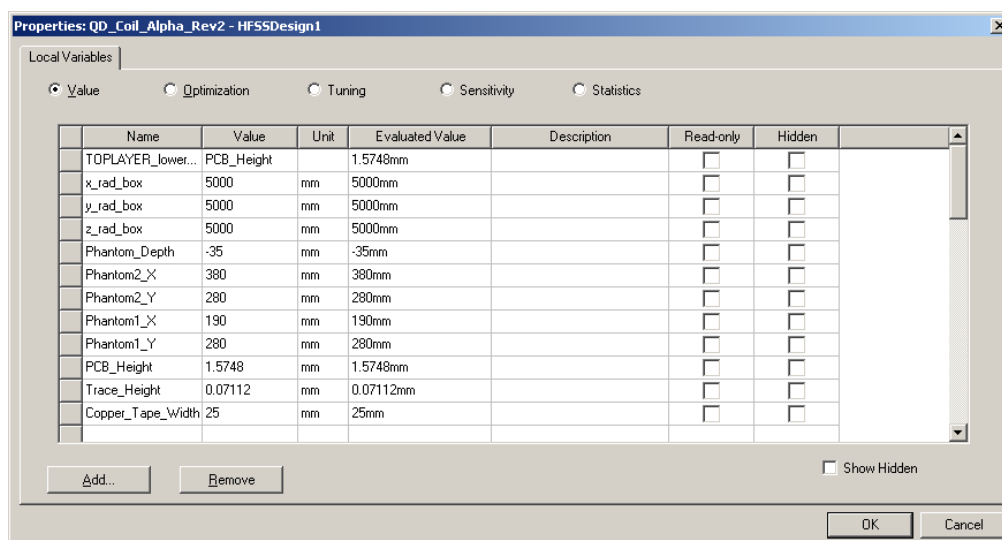


Figure 3.5: Design Properties Window

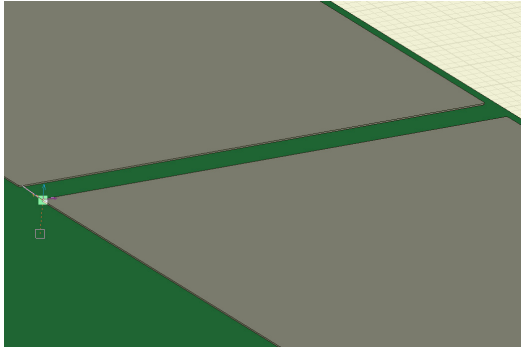
3.2.2.4 The Lumped Port Excitation

In HFSS, a lumped port excitation can be defined across any plane. The plane to be defined as the port can be drawn using any 2D surface geometry, or by drawing individual lines or splines to form a closed geometry. When creating a closed geometry from individual lines, HFSS by default adds the “Cover Lines” operation which will create a 2D sheet using the lines drawn as boundaries.

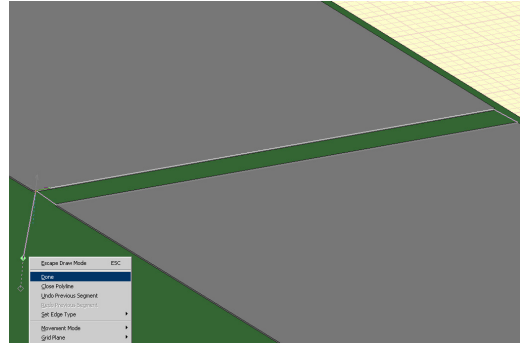
Once the desired 2D sheet is created, it can be assigned as a “Lumped Port”. Right Click on the recently created object’s name in the project tree windows and select “Assign Excitation” and then “Lumped Port...”. A dialog will appear where the characteristic impedance of the port can be defined. The next step is to define the line of integration. The line of integration is defined by the arrow shown below which indicates the direction of current flow. Mathematically represented by:

$$V = \oint_l E \cdot dl \quad (3.1)$$

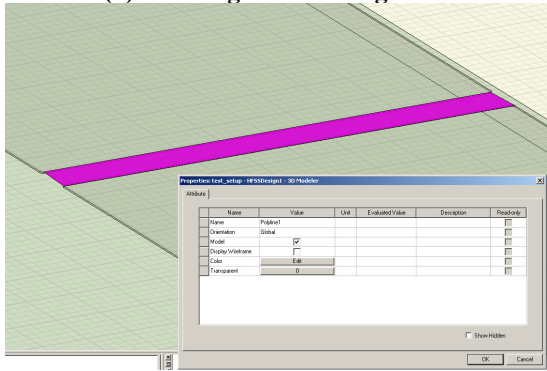
Select two points across the plane connecting both conductors to create the definition. A red arrow can now be seen across the port. The final step gives an option to renormalize the port impedance for post processing of S-Parameters. This does not effect the S-Parameter calculation and is not used in this design. Screenshots of the process, step by step are shown in Figure 3.6.



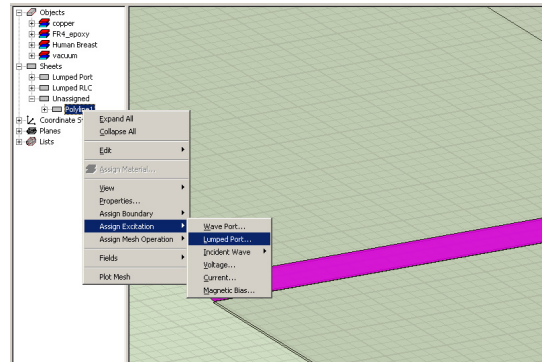
(a) Drawing the Line Segments



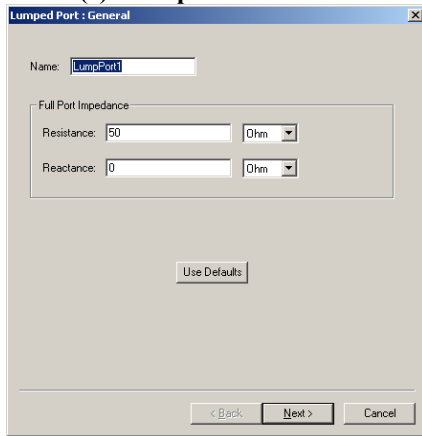
(b) Connecting all Line Segments



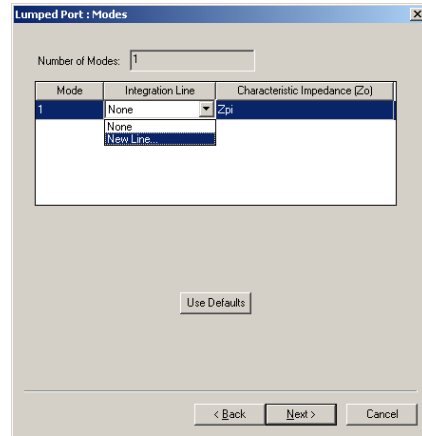
(c) Completed 2D Sheet



(d) Assigning the Port Definition



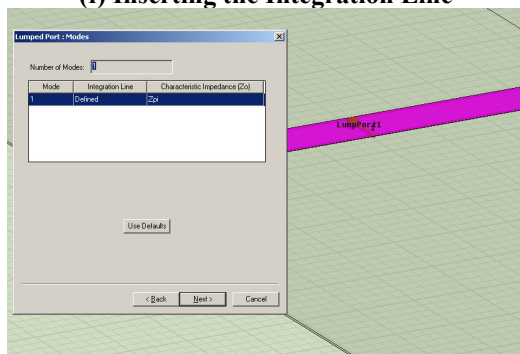
(e) Assigning the Port Impedance



(f) Inserting the Integration Line



(g) Defining the Integration Line



(f) Setting the Port Impedance

Figure 3.6: Defining a Lumped Port

3.2.2.5 Radiation Boundary

For all finite element simulations, a boundary must be defined around the structure. This “air-box” is defined as the radiation boundary. It is important that the size of this box is at least the size of the wavelength of the Larmor frequency being solved. A box made of vacuum material is then created. This boundary condition is assigned to the box by right clicking on the object in the project tree and selecting “Assign Boundary” and then “Radiation”. The default parameters are used. HFSS uses a second order boundary condition set up at this interface which is designed to absorb waves from the radiating structure so as not to allow any reflections at the radiation boundary:

$$(\nabla \times \mathbf{E})_{\text{tan}} = jk_0 \mathbf{E}_{\text{tan}} - \frac{j}{k_0} \nabla_{\text{tan}} \times (\nabla_{\text{tan}} \times \mathbf{E}_{\text{tan}}) + \frac{j}{k_0} \nabla_{\text{tan}} (\nabla_{\text{tan}} \cdot \mathbf{E}_{\text{tan}}) \quad (3.2)$$

where

- E_{tan} is the component of the E-field that is tangential to the surface.
- ∇_{tan} is the gradient taken tangential to the surface.
- k_0 is the free space phase constant

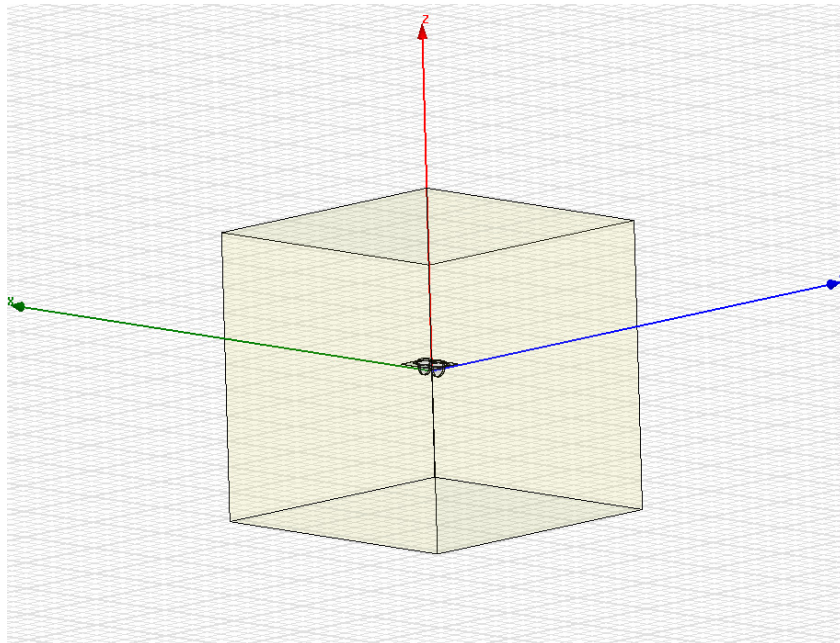


Figure 3.7: Defined Radiation Boundary Encompassing the Coil Structure

3.2.2.6 Assigning Material Properties

HFSS has a built-in library with over 100 common materials. This library includes frequency dependent parameters for each material such as relative permittivity, relative permeability, bulk conductivity, and dielectric loss tangent. Also included in the Human Body Model, are frequency dependant values for various human tissues. Highlighted are the material properties of copper. This menu can be accessed by right clicking on any object and selecting “Assign Material”

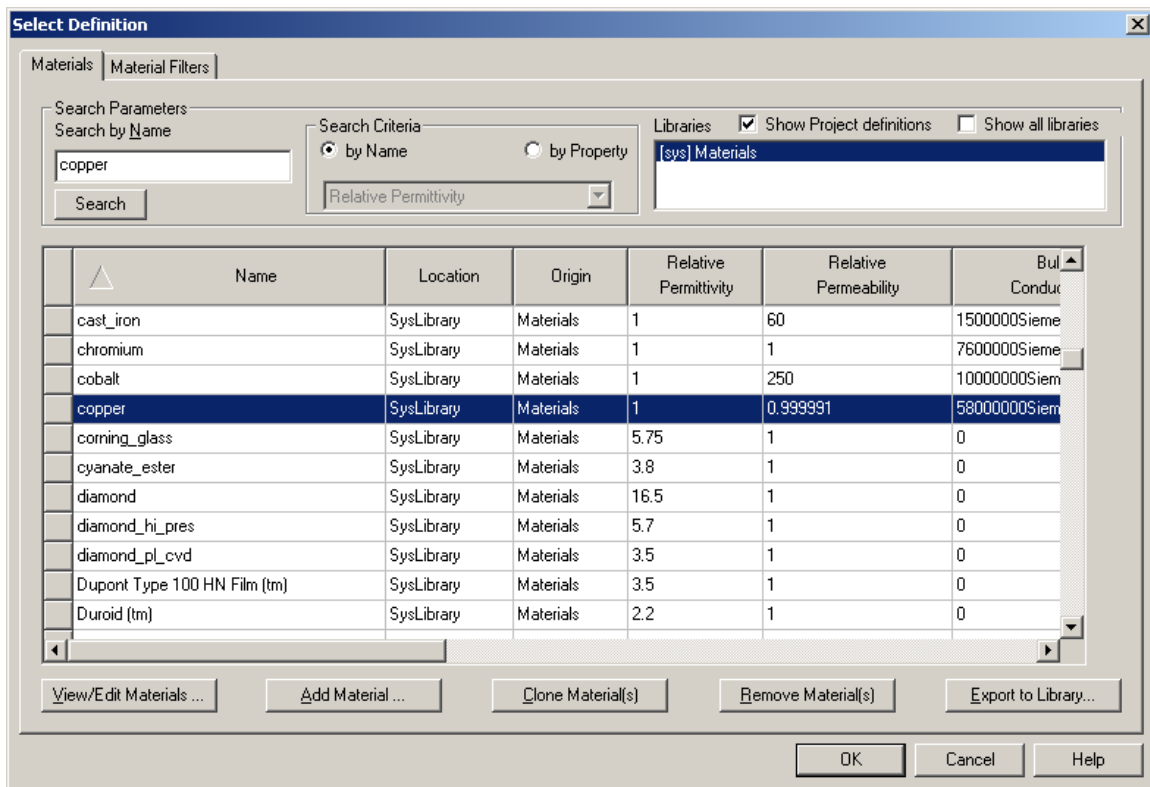


Figure 3.8: Material Properties Window

3.2.3 Defining Simulation Parameters

The simulation setup dialog includes options that control how the simulation is performed. The first option is the “Solution Frequency”. This parameter is used in the adaptive meshing algorithm to optimize mesh performance to satisfy FEM requirements for the number of nodes per wavelength. When moving a coil design to a different magnet system, i.e. 1.5T to 3T, the proper Larmor frequency can be changed here, and the simulation results are re-computed.

The next parameters are the maximum number of solver iterations or “passes” that should be completed, and the convergence criteria for each pass. A single HFSS simulation actually contains multiple FEM solutions. HFSS uses an iterative solving process where an initial mesh is created, and an FEM solution for the field data and S-Parameters are computed. Then a second, denser mesh is generated, and another FEM solution found. At this point, using a proprietary algorithm, HFSS continues to more densely mesh locations of the structure as its algorithm sees fit to create the most efficient mesh and re-solve the structure for the most accurate FEM solution. The maximum number of passes setting limits how many of these iterative solutions will be done.

Another way to limit the number of solution passes is to set convergence criteria. After each successive pass, the maximum difference in the magnitude of all S-Parameters between successive passes is calculated. This is the “Maximum Delta Energy” Convergence criteria parameter. If the change in S-Parameters is less than this value, the simulation will end, even if the maximum number of passes has not been reached. For all simulations, this parameter is set to 10^{-6} . This will ensure that the simulation will continue to solve until the maximum number of passes has been reached, as sometimes the solution’s convergence may oscillate and end before an accurate solution is found.

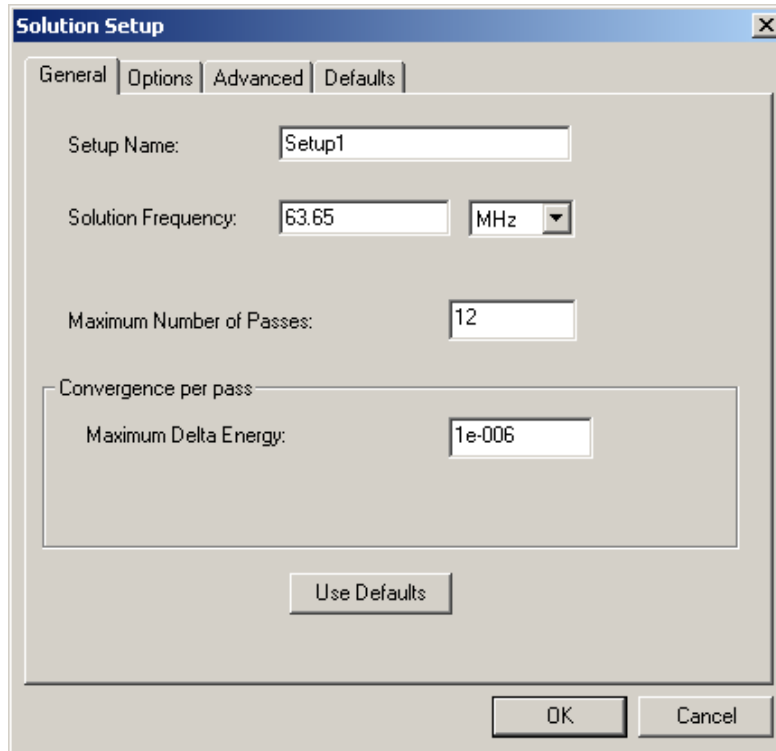


Figure 3.9: Simulation Setup Window

While there are a wide array of options that affect how the solver works, the default parameters typically work well for MRI coil designs. One important option to check is that the maximum number of processors is set in the HFSS solver options dialog. HFSS's solver program is multi-threaded to work with more than one processor to fully utilize modern multi-core, multi-processor computers. The standard desktop PC today contains a single dual core processor, while a typical workstation PC can contain up to four - quad core processors. Simulation time can be dramatically reduced when utilizing all of the available processors.

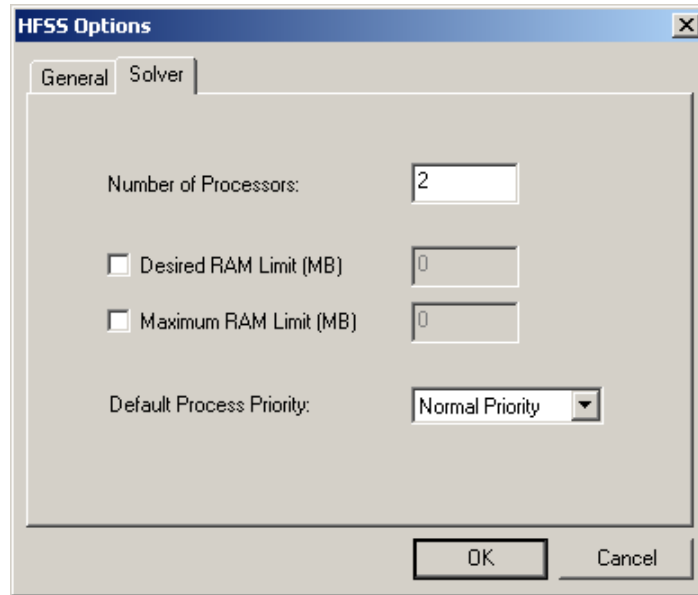


Figure 3.10: HFSS Solver Options Window

3.2.4 Running and Monitoring Simulations

After the model is created and all ports and boundaries are properly setup, the final step before simulation is to perform a model validation. While the validation check is a good way to ensure a simulation is setup properly, it does not however check to ensure proper mesh generation; this can only be done in simulation.

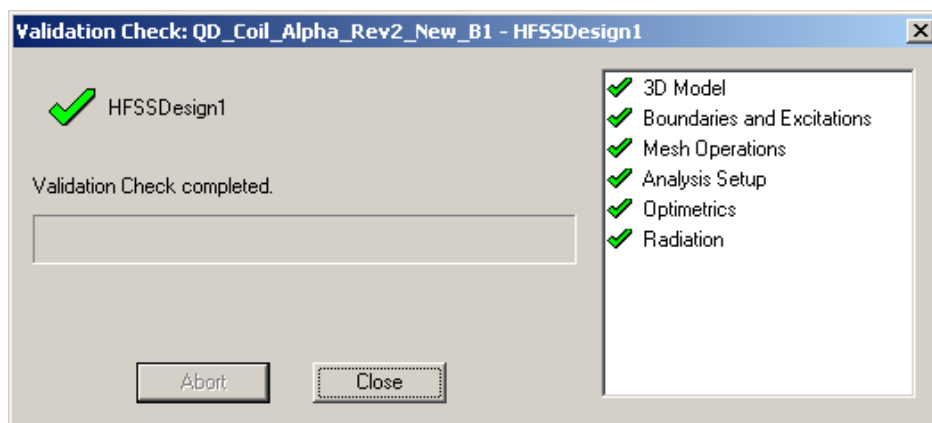


Figure 3.11: Simulation Validation Check Window

Information about the simulation can be obtained from the “Solution Data” window after a simulation is completed, or during a running simulation. It is accessed by right clicking on “Results” in the project tree and selecting “Solution Data”. Three tabs can be seen that show information about the simulation profile containing time and computing resources used, the convergence data, and S-Parameter Data.

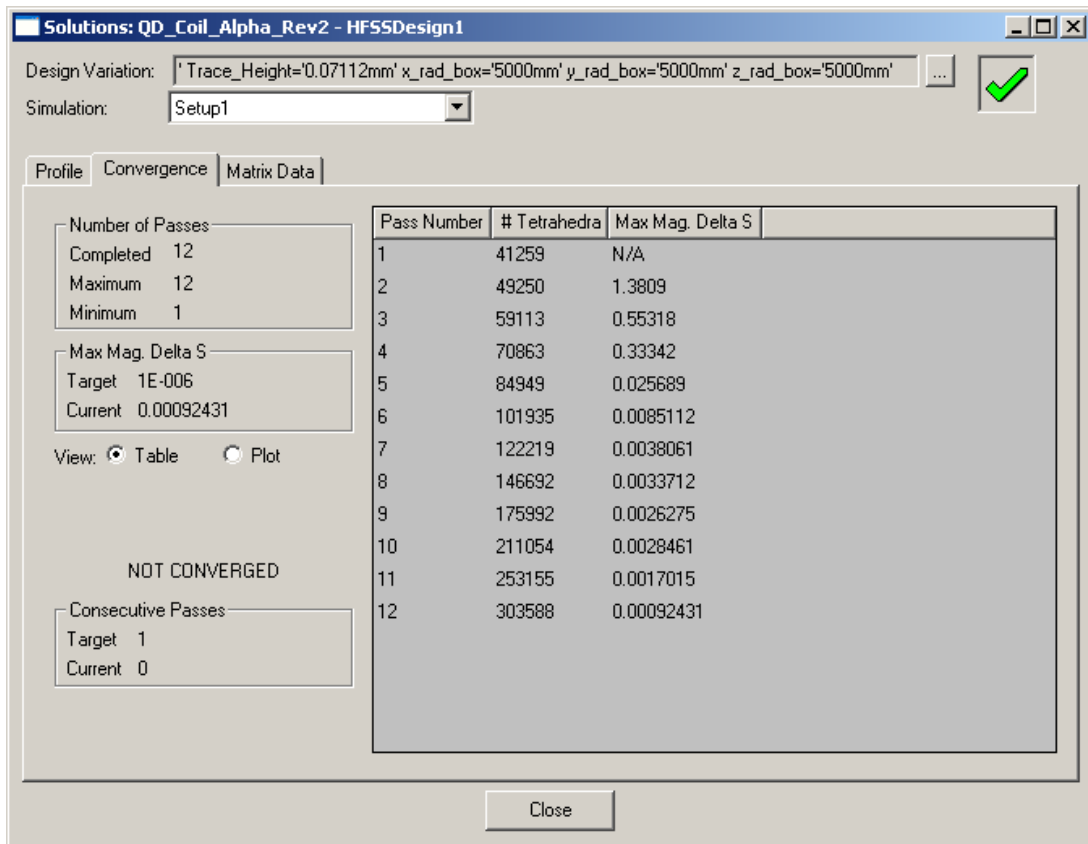


Figure 3.12: Solution Data Window

3.3 Human Body Load Modeling

Ansoft has an existing human body model that incorporates the following features:

- Accuracy to millimeter scale
- 300+ objects, including bones, muscles, and organs
- Frequency-dependant electrical properties for each type of tissue.

Figure 3.13 depicts the 3D mesh of the human body model.

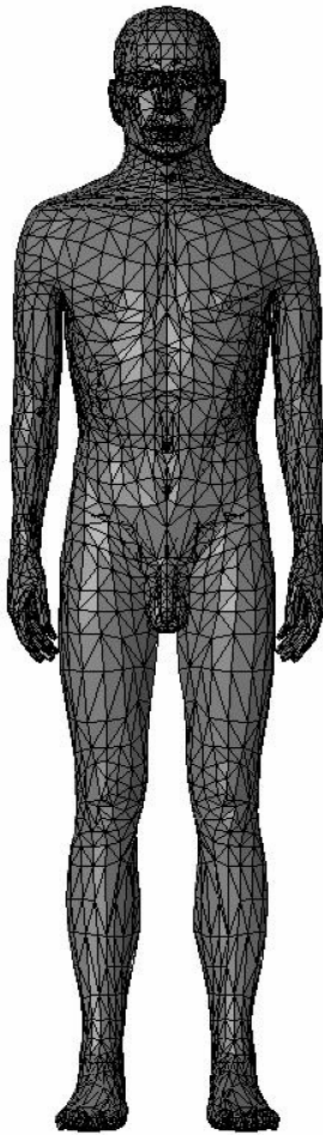


Figure 3.13: Ansoft Human Body Model

3.3.1 Augmenting the Model

Since the model provided is only suitable for the male anatomy, and the human load for this coil is the female breasts, the original male model has been augmented with female breasts as seen in Figure 3.14. These breasts were created inside Ansoft's geometry system using cylinders and spheres. The dimensions of the breasts were modeled based on the average female breast size of 34C [14]. These dimensions can be seen in Figure 3.16.

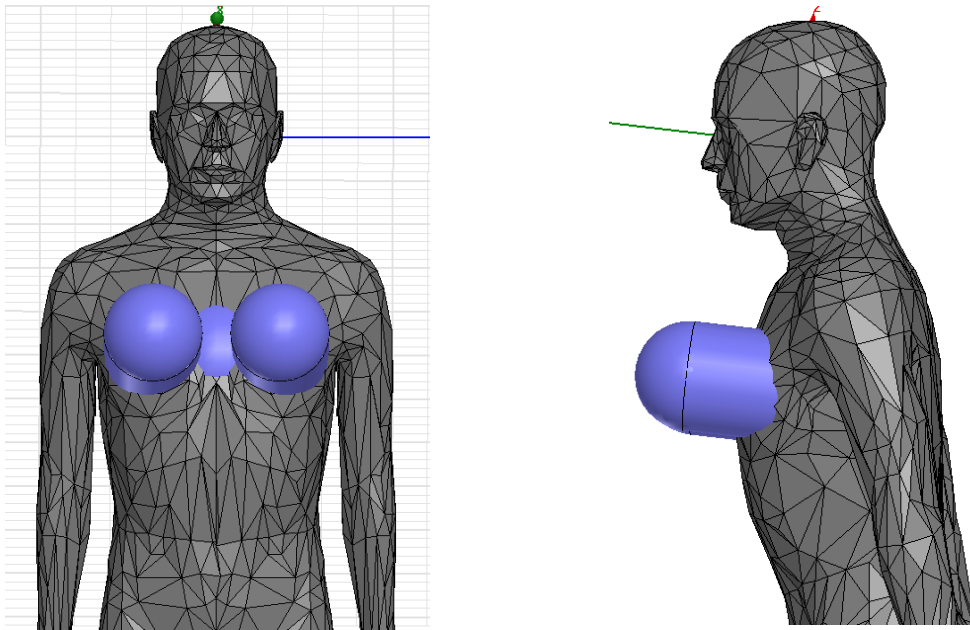


Figure 3.14: Human Body Model with Added Breasts

To reduce simulation time, only the torso of the body is used. The majority of the small internal organs and bones are also removed as their loading effects are considered minimal.

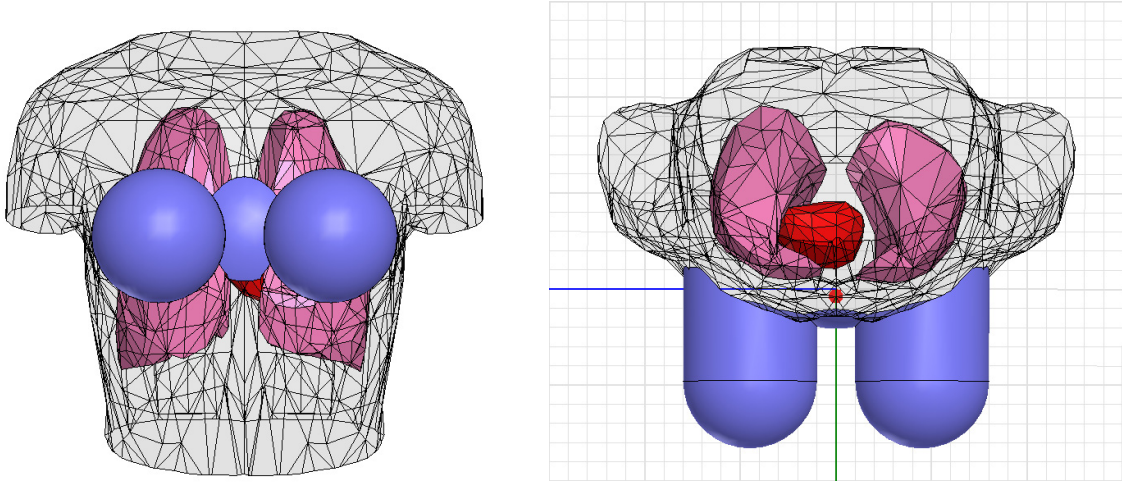


Figure 3.15: Human Body Model used for Simulation

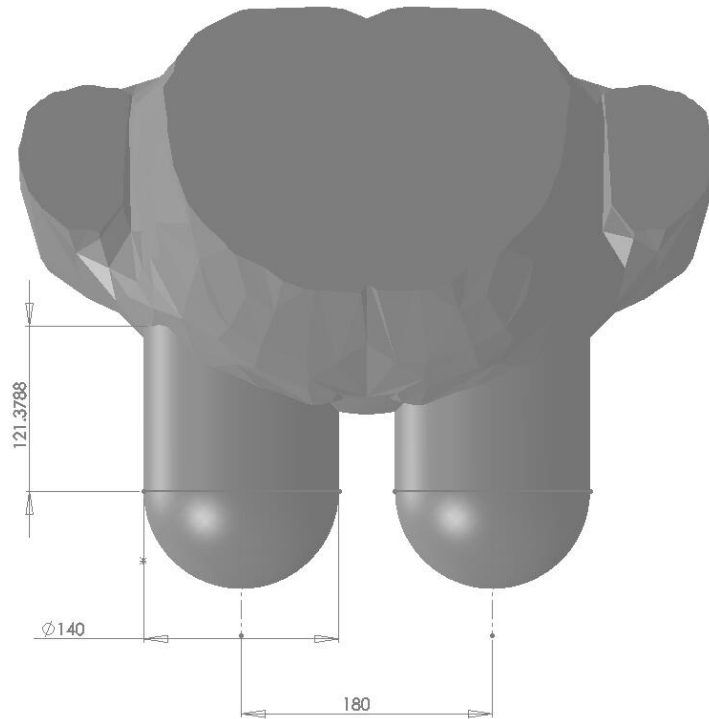


Figure 3.16: Dimensions of Augmented Breasts

3.3.2 Dielectric and Conductivity Data

Figure 3.17 shows an example of the frequency dependant data included for the tissues of the human body model. This is the dataset for the relative dielectric constant or permittivity of fat. The practically relevant parameters are those at the Larmor frequency.

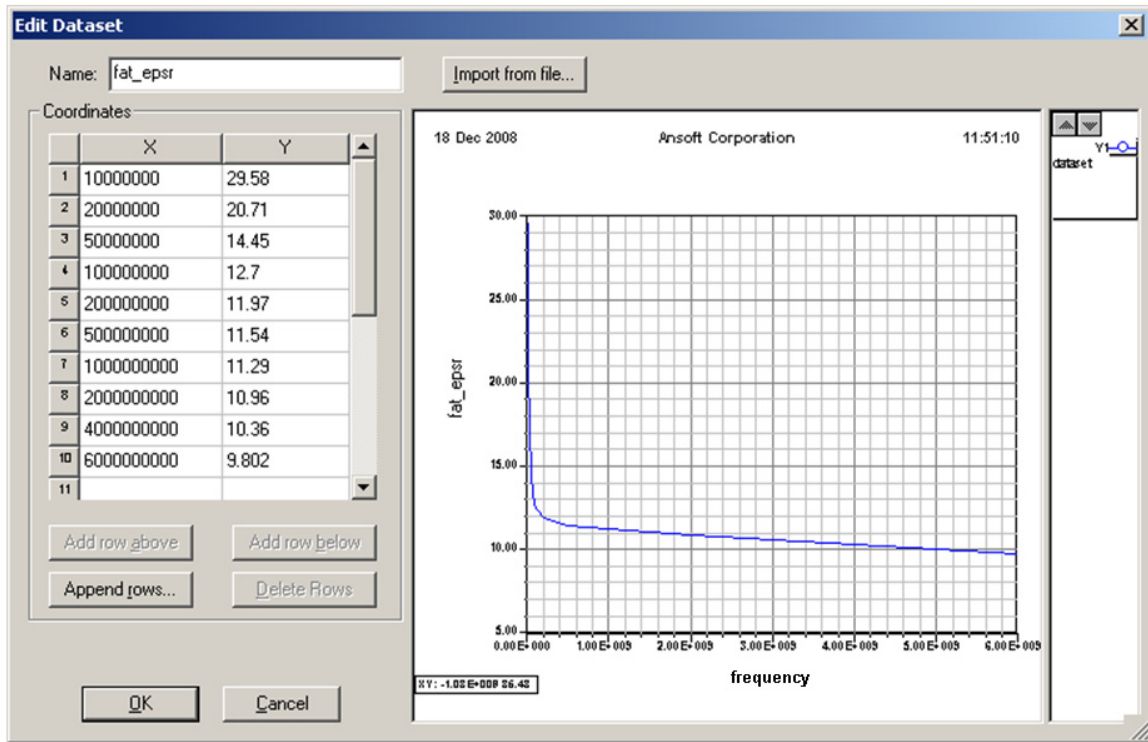


Figure 3.17: Relative Dielectric Constant of Fat vs. Frequency

3.4 Circuit Modeling with MATLAB

3.4.1 Circuit Modeling

Circuit modeling is done using linear network analysis. To better explain the circuit simulation method, a simpler example coil will be used. In this case a single loop, single channel coil with four breaks for lumped elements will be modeled. The HFSS structure model can be seen in. The four breaks are labeled 1 through 4.

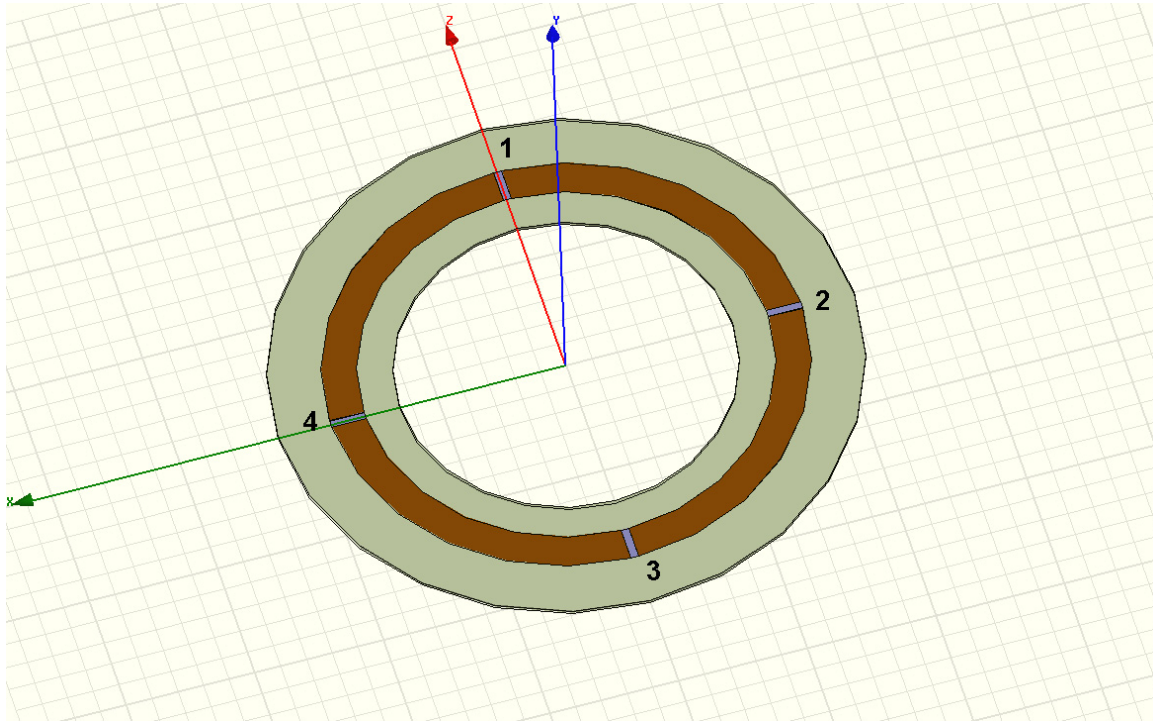


Figure 3.18: Single Loop Surface Coil.

The four breaks are placed equidistant from each other around the loop. Each of these breaks is assigned as a “port” in the simulation. The result of this simulation is a 4x4 S-matrix that describes this coil structure at the center frequency.

$$S_{Structure} = \begin{bmatrix} S_{11} & S_{12} & S_{13} & S_{14} \\ S_{21} & S_{22} & S_{23} & S_{24} \\ S_{31} & S_{32} & S_{33} & S_{34} \\ S_{41} & S_{42} & S_{43} & S_{44} \end{bmatrix} \quad (3.3)$$

In reality, ports 1-3 are terminated by a single capacitor, and port 4 is terminated with a two port matching network. For this two port matching network, one end will be connected to the structures fourth port, while the other port will become the real single port of the coil. A diagram of these interconnections can be seen in Figure 3.19. The system is now reduced into a one port network (single channel) for which the new S-Parameters of this system can be solved for mathematically.

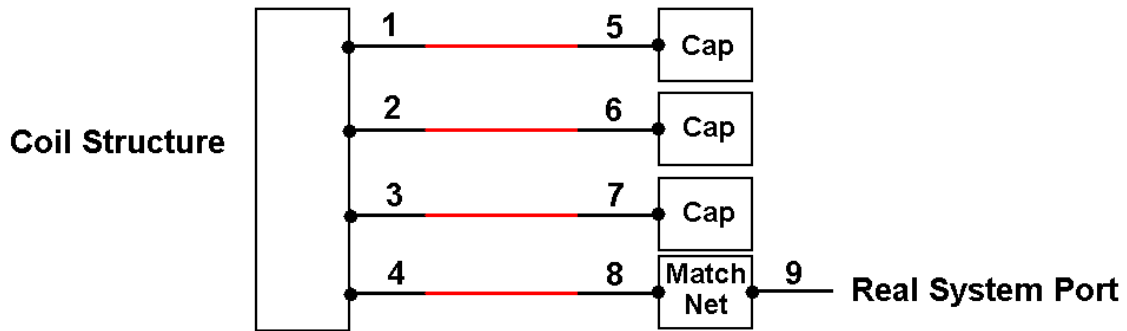


Figure 3.19: Coil and Lumped Element Interconnections, Port Definitions

The S matrices of these lumped element components are known and can be calculated as:

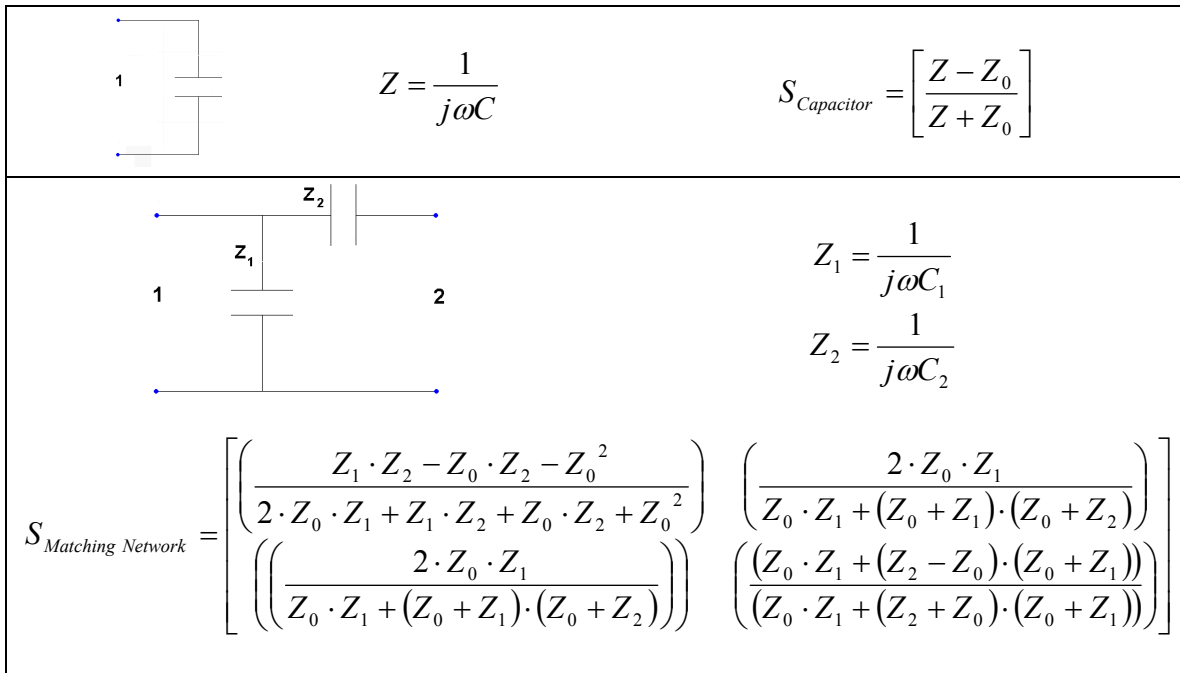


Figure 3.20: Lumped Element Terminations and S-Matrices

The S-matrices of the coil structure, capacitors, and matching network are combined into one large S matrix, S_{New} .

$$S_{New} = \begin{bmatrix} \begin{bmatrix} S_{11} & S_{12} & S_{13} & S_{14} \\ S_{21} & S_{22} & S_{23} & S_{24} \\ S_{31} & S_{32} & S_{33} & S_{34} \\ S_{41} & S_{42} & S_{43} & S_{44} \end{bmatrix} & 0 & 0 & 0 & 0 & 0 & 0 & 0 & 0 \\ 0 & 0 & 0 & 0 & [S_{55}] & 0 & 0 & 0 & 0 \\ 0 & 0 & 0 & 0 & 0 & [S_{66}] & 0 & 0 & 0 \\ 0 & 0 & 0 & 0 & 0 & 0 & [S_{77}] & 0 & 0 \\ 0 & 0 & 0 & 0 & 0 & 0 & 0 & \begin{bmatrix} S_{88} & S_{89} \\ S_{98} & S_{99} \end{bmatrix} \\ 0 & 0 & 0 & 0 & 0 & 0 & 0 & \begin{bmatrix} S_{88} & S_{89} \\ S_{98} & S_{99} \end{bmatrix} \end{bmatrix} \quad (3.4)$$

The general S-Parameter matrix is defined as:

$$S\bar{a} = \bar{b} \quad (3.5)$$

where b is the reflected power, and a is the incident power of a port.

Using these equations, a system of equations can be written as:

$$\begin{bmatrix} \begin{bmatrix} S_{11} & S_{12} & S_{13} & S_{14} \\ S_{21} & S_{22} & S_{23} & S_{24} \\ S_{31} & S_{32} & S_{33} & S_{34} \\ S_{41} & S_{42} & S_{43} & S_{44} \end{bmatrix} & 0 & 0 & 0 & 0 & 0 & 0 & 0 & 0 \\ 0 & 0 & 0 & 0 & [S_{55}] & 0 & 0 & 0 & 0 \\ 0 & 0 & 0 & 0 & 0 & [S_{66}] & 0 & 0 & 0 \\ 0 & 0 & 0 & 0 & 0 & 0 & [S_{77}] & 0 & 0 \\ 0 & 0 & 0 & 0 & 0 & 0 & 0 & \begin{bmatrix} S_{88} & S_{89} \\ S_{98} & S_{99} \end{bmatrix} \\ 0 & 0 & 0 & 0 & 0 & 0 & 0 & \begin{bmatrix} S_{88} & S_{89} \\ S_{98} & S_{99} \end{bmatrix} \end{bmatrix} \cdot \begin{bmatrix} a_1 \\ a_2 \\ a_3 \\ a_4 \\ a_5 \\ a_6 \\ a_7 \\ a_8 \\ a_9 \end{bmatrix} = \begin{bmatrix} b_1 \\ b_2 \\ b_3 \\ b_4 \\ b_5 \\ b_6 \\ b_7 \\ b_8 \\ b_9 \end{bmatrix} \quad (3.6)$$

At this point the knowledge of the interconnections is used to reduce the system. For example, since port 1 is connected to port 5, it can be said that:

$$\begin{aligned} b_1 &= a_5 \\ b_5 &= a_1 \end{aligned}$$

Therefore, the system can be re-written as:

$$\begin{bmatrix} \begin{bmatrix} S_{11} & S_{12} & S_{13} & S_{14} \\ S_{21} & S_{22} & S_{23} & S_{24} \\ S_{31} & S_{32} & S_{33} & S_{34} \\ S_{41} & S_{42} & S_{43} & S_{44} \end{bmatrix} & -1 & 0 & 0 & 0 & 0 \\ -1 & 0 & 0 & 0 & [S_{55}] & 0 & 0 & 0 & 0 \\ 0 & 0 & 0 & 0 & 0 & [S_{66}] & 0 & 0 & 0 \\ 0 & 0 & 0 & 0 & 0 & 0 & [S_{77}] & 0 & 0 \\ 0 & 0 & 0 & 0 & 0 & 0 & 0 & \begin{bmatrix} S_{88} & S_{89} \\ S_{98} & S_{99} \end{bmatrix} & \\ 0 & 0 & 0 & 0 & 0 & 0 & 0 & \end{bmatrix} \cdot \begin{bmatrix} a_1 \\ a_2 \\ a_3 \\ a_4 \\ a_5 \\ a_6 \\ a_7 \\ a_8 \\ a_9 \end{bmatrix} = \begin{bmatrix} 0 \\ b_2 \\ b_3 \\ b_4 \\ 0 \\ b_6 \\ b_7 \\ b_8 \\ b_9 \end{bmatrix} \quad (3.7)$$

Using the rest of the interconnections as described in Figure 3.19, the system can be re-written as:

$$\begin{bmatrix} \begin{bmatrix} S_{11} & S_{12} & S_{13} & S_{14} \\ S_{21} & S_{22} & S_{23} & S_{24} \\ S_{31} & S_{32} & S_{33} & S_{34} \\ S_{41} & S_{42} & S_{43} & S_{44} \end{bmatrix} & -1 & 0 & 0 & 0 & 0 \\ -1 & 0 & 0 & 0 & [S_{55}] & 0 & 0 & 0 & 0 \\ 0 & -1 & 0 & 0 & 0 & [S_{66}] & 0 & 0 & 0 \\ 0 & 0 & -1 & 0 & 0 & 0 & [S_{77}] & 0 & 0 \\ 0 & 0 & 0 & -1 & 0 & 0 & 0 & \begin{bmatrix} S_{88} & S_{89} \\ S_{98} & S_{99} \end{bmatrix} & \\ 0 & 0 & 0 & 0 & 0 & 0 & 0 & \end{bmatrix} \cdot \begin{bmatrix} a_1 \\ a_2 \\ a_3 \\ a_4 \\ a_5 \\ a_6 \\ a_7 \\ a_8 \\ a_9 \end{bmatrix} = \begin{bmatrix} 0 \\ 0 \\ 0 \\ 0 \\ 0 \\ 0 \\ 0 \\ 0 \\ b_9 \end{bmatrix} \quad (3.8)$$

The system can then be reduced to a single equation for which the S-Parameter of the free real port of the fully terminated system can be found:

$$[S_{free-port}] \cdot [a_9] = [b_9] \quad (3.9)$$

To ease the process of determining the lumped elements, it is desirable to see the new reduced S-Matrix at frequencies above and below the center frequency. This will allow the user who is manually tuning and matching the system to be able to see the resonant behavior shift over a sweep of frequencies as capacitor values are changed. While it is easy to recalculate the S-Matrices of the lumped element components at the neighboring frequencies, the S-Matrix of the structure from the HFSS Simulation only contains data at the center frequency. However, this data can be interpolated.

The S-matrix coefficients of neighboring frequencies are interpolated by first converting the S-matrix to the admittance or Y-matrix; it is assumed that each term in the Y-matrix depends on frequency inductively according to $1/(c_{mn} + j\omega d_{mn})$. After obtaining the frequency independent coefficients c_{mn} , d_{mn} around the resonance frequency, the Y-matrix is then converted back into S-matrix form. The system matrix reduction procedure is then repeated for the desired neighboring frequencies. At this point a full sweep of the S-Parameters of the system is obtained.

3.4.2 Matlab S-Parameter Accuracy

In order to confirm the accuracy of the S-Parameter sweep approximation used in the simulation method, a basic single loop coil with one port was simulated. The coil loop, shown in Figure 3.21, is 45mm in radius and is comprised of a strip that is 1mm in width, 0.1mm in thickness and the material properties of copper.

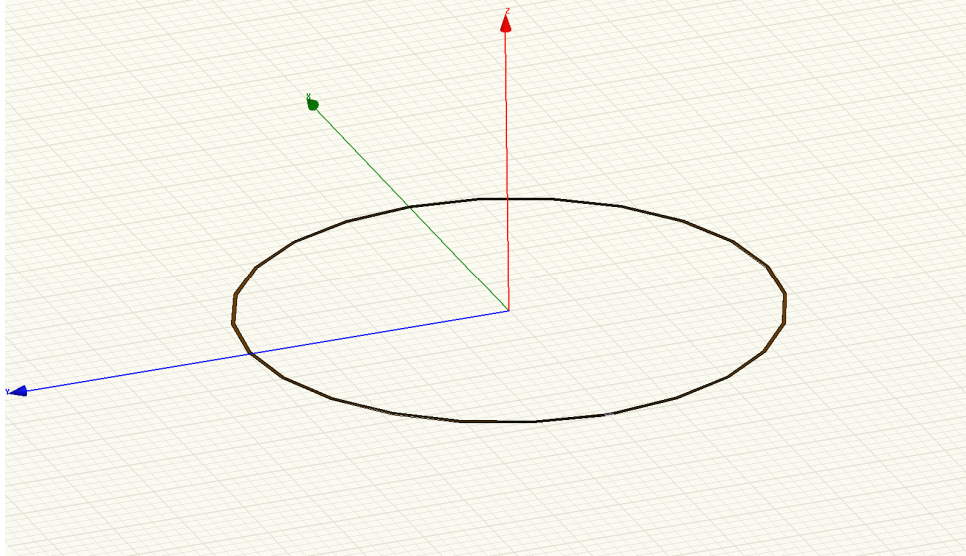


Figure 3.21: Single Loop Coil Model

The single port of the coil loop will be terminated with a shunt-series capacitive tune and match network as seen in Figure 3.22. With the proper selection of C_1 and C_2 , the coil will be able to resonate at the desired center frequency of 63.65MHz.

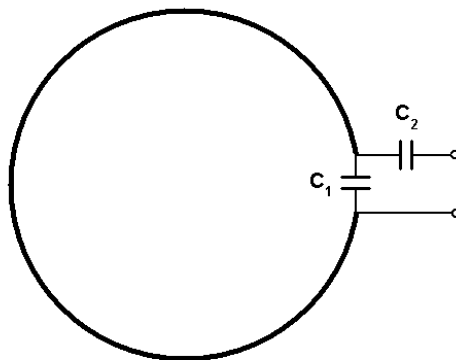


Figure 3.22: Coil Loop Circuit Schematic

An FEM solution in HFSS was computed using 296453 tetrahedral mesh elements at each of 101 discrete frequency points from 63.15MHz to 64.15MHz in 0.01MHz steps.

First, the coil is tuned and matched to 63.65MHz using the inductive sweep approximation which is based only on the S-Parameter data from HFSS at 63.65MHz. C_1 was found to be 20.16 pF and C_2 was found to be 1.7pF. The resulting S-Parameter data generated can be seen in Figure 3.23.

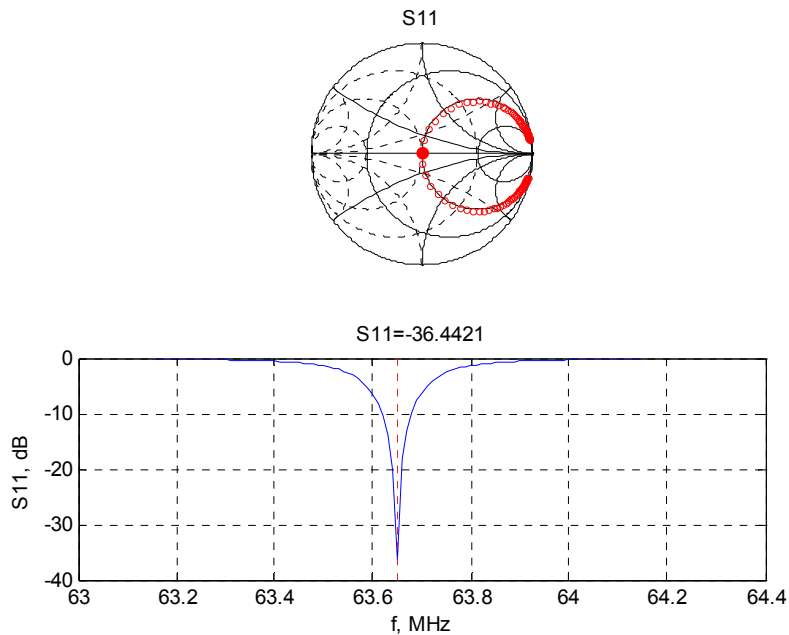


Figure 3.23: Single Point S-Parameter Approximation

Next, to confirm the accuracy of this data generated using the MATLAB code, a second Ansoft software package known as Ansoft Designer is used. Ansoft Designer is a circuit simulator similar to Agilent ADS that can perform linear network analysis. A circuit simulation was setup to re-simulate the circuit modeling done previously with MATLAB.

In this circuit simulation; schematic seen in Figure 3.24; the determined values for C_1 (C_{Tune}) and C_2 (C_{Match}) from the first step are defined in Ansoft Designer. The data-block labeled “LumpPort1:1” contains the solved S-Parameter data at each frequency point from HFSS. A simulation is setup to compute the new S-Parameters of “Port1”.

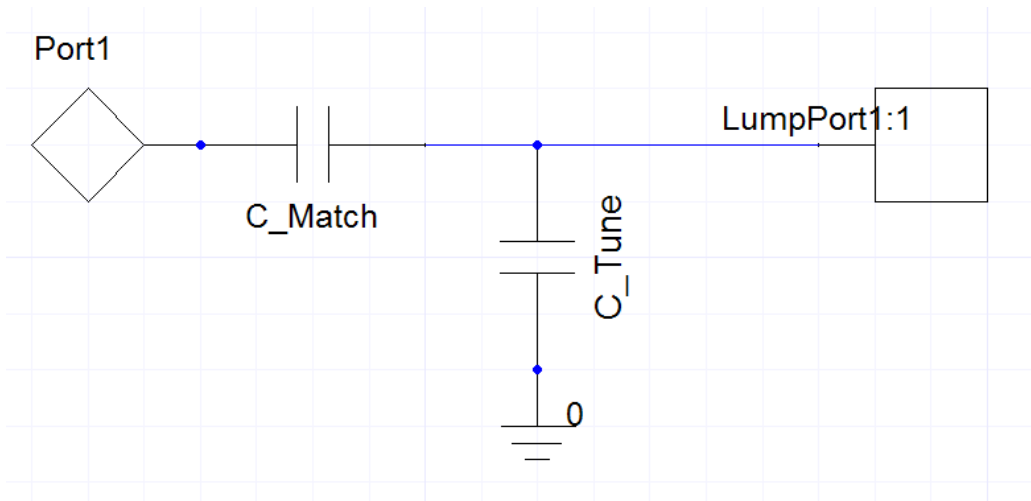


Figure 3.24: Ansoft Designer Circuit Schematic

The data generated by the Ansoft Designer simulation is exported from Designer and imported into MATLAB. The data from the MATLAB simulation based on the FEM data at 63.65MHz, and the data from the Ansoft Designer simulation based on the FEM data at each frequency point in the sweep are plot on the same graph seen in Figure 3.25. It can be seen that there is good agreement between both simulation methods.

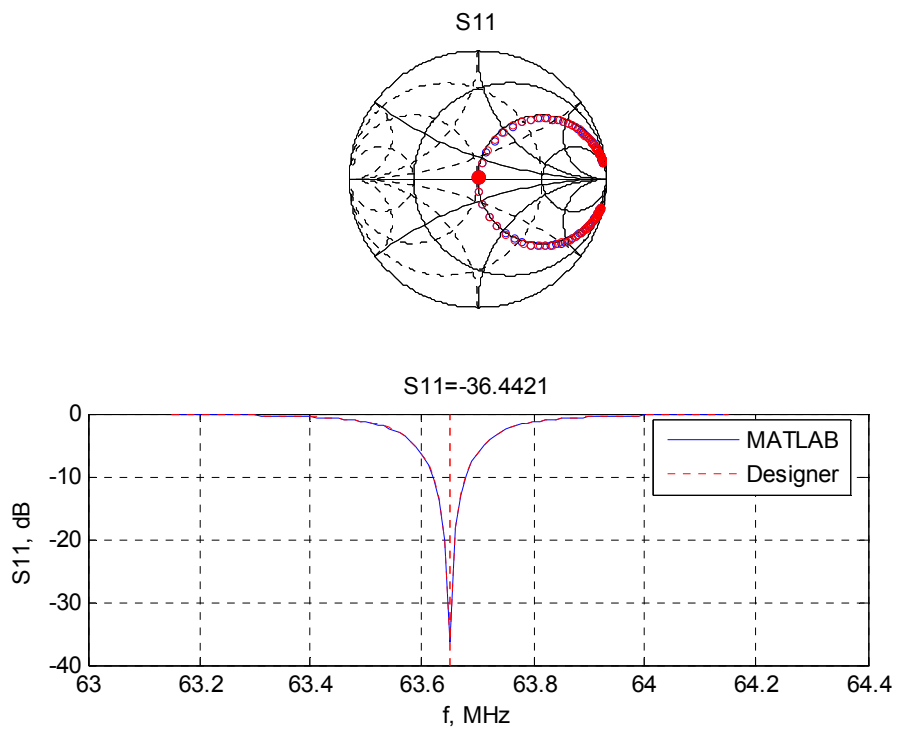
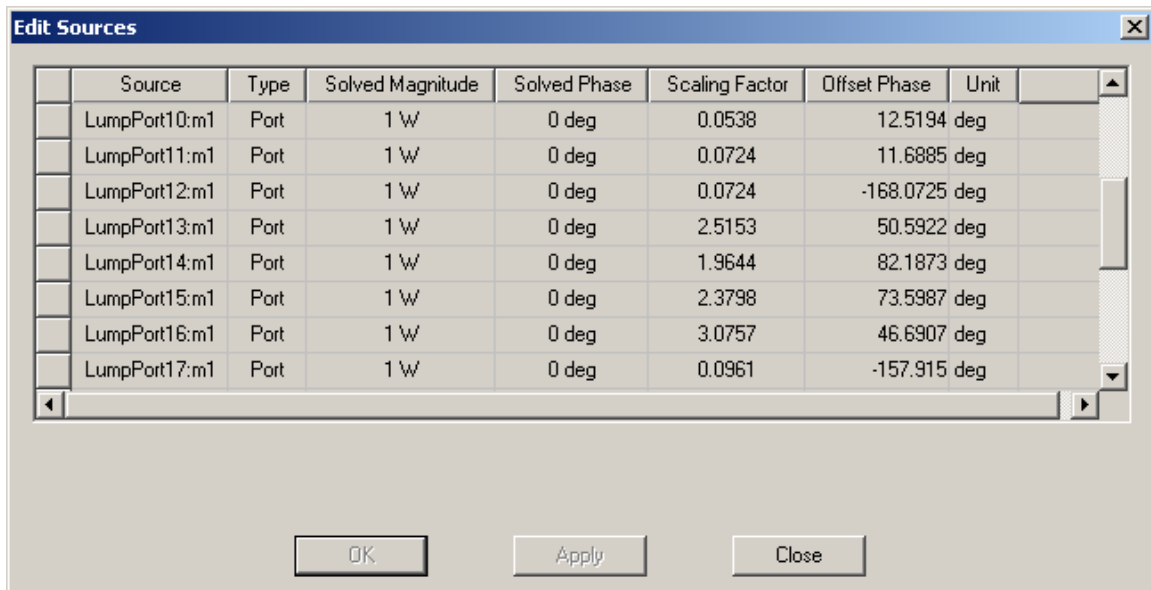


Figure 3.25: MATLAB vs. Ansoft Designer S-Parameter Comparison

3.4.3 Modifying the HFSS Solution with Circuit Data from MATLAB

HFSS includes the ability to re-calculate the field data of the structure based on how each port is driven with a given amount of complex power. In the initial HFSS simulation, the field data is solved by exciting each port individually with 1 watt of power while the remaining ports are terminated with 50Ω impedances. Using this knowledge, a MATLAB script is used to compute a new set of complex power values which are then used to drive each of the N ports of the HFSS simulation in order to mimic the effect of terminating those N ports with the calculated lumped elements from the resonating simulation model from MATLAB. It is in this way that the original field solution from HFSS is “power scaled” in order to generate new field data of a coil array that is now tuned, matched, and decoupled to the levels set with the lumped elements determined using the first MATLAB script. In Figure 3.26, the “Edit Sources” window of HFSS can be seen. It is here that the “Scaling Factor” and “Offset Phase” values are imported into HFSS from the MATLAB script.



The screenshot shows the 'Edit Sources' window in HFSS. It contains a table with 8 rows of source data. The columns are Source, Type, Solved Magnitude, Solved Phase, Scaling Factor, Offset Phase, and Unit. The 'Solved Magnitude' for all ports is 1 W, and the 'Solved Phase' is 0 deg. The 'Scaling Factor' and 'Offset Phase' values are imported from a MATLAB script.

Source	Type	Solved Magnitude	Solved Phase	Scaling Factor	Offset Phase	Unit
LumpPort10:m1	Port	1 W	0 deg	0.0538	12.5194 deg	
LumpPort11:m1	Port	1 W	0 deg	0.0724	11.6885 deg	
LumpPort12:m1	Port	1 W	0 deg	0.0724	-168.0725 deg	
LumpPort13:m1	Port	1 W	0 deg	2.5153	50.5922 deg	
LumpPort14:m1	Port	1 W	0 deg	1.9644	82.1873 deg	
LumpPort15:m1	Port	1 W	0 deg	2.3798	73.5987 deg	
LumpPort16:m1	Port	1 W	0 deg	3.0757	46.6907 deg	
LumpPort17:m1	Port	1 W	0 deg	0.0961	-157.915 deg	

Figure 3.26: HFSS Edit Sources Window

In this final step, weights of the individual FEM solutions can be obtained in order to simulate the field effects of the structure when terminated by the lumped elements in the circuit model. First, it is known that HFSS calculates S-Parameters by exciting each port with 1W of incident power. From (3.10), the incident power coefficient a can be calculated:

$$P_{Incident} = \frac{1}{2}|a|^2 = 1W \quad \therefore a = \sqrt{2} \quad (3.10)$$

Using the previous example situation from section 3.4.1, a_9 is replaced with $\sqrt{2}$, since it is the real system port which will be driven with 1W of power. The modified S-Matrix from (3.8) can then be re-solved to obtain the remaining coefficients a_1 through a_8 .

With these new coefficients, a set of power magnitude and phase scaling values can be obtained for every port in the structure. These values are calculated as:

$$Magnitude\ Scale_n = \left| \frac{a_n^2}{2} \right| \quad (3.11)$$

$$Phase\ Offset_n = phase(a_n)$$

These values will be imported into HFSS so that the field data can be properly modified as to have the effect of terminating the structure's four ports with the lumped elements that were determined in the Matlab circuit simulation. At this point field data of the tuned and matched structure can be evaluated within HFSS.

3.4.4 HFSS Field Data Accuracy

In order to confirm that accurate field data is generated by HFSS using the simulation method, the basic single loop coil with one port used as an example in Section 3.4.2 is revisited.

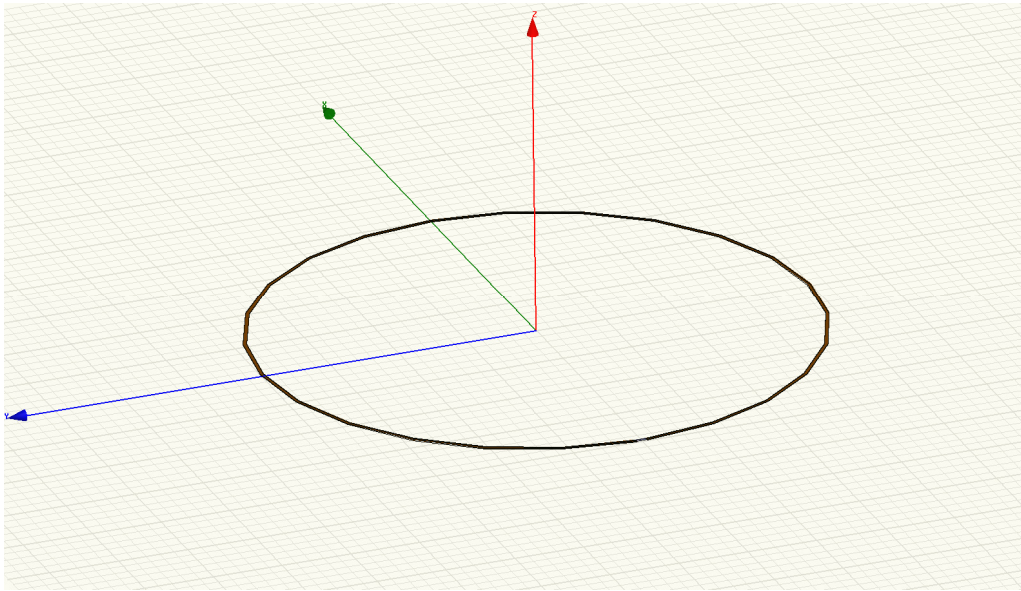


Figure 3.27: Single Loop Coil Model

In this example, the power scale factor and offset phase for the port are generated as described in section 3.4.3. These values were computed as 270.8301 and 63.8647 degrees and were imported into the HFSS model to post-process the field data to simulate the now resonating coil. At this point, the B field data is computed along the z-axis from -100 to 100mm and exported into Matlab so that this data may be compared to the analytical result.

This simple single loop coil model was chosen since an analytical expression for the value of the magnetic field along the center z axis of the loop can be used to compare with the simulated value:

$$B_z = \frac{\mu_0 I}{4\pi} \cdot \frac{2\pi R^2 I}{(z^2 + R^2)^{3/2}} \quad (3.12)$$

Where $I = 2.63A$, $R = 0.045m$

In Figure 3.28, the analytical result as calculated using ((3.12) and the simulated data from HFSS are plot in the same graph. It can be seen that there is good agreement between the simulated and analytical result.

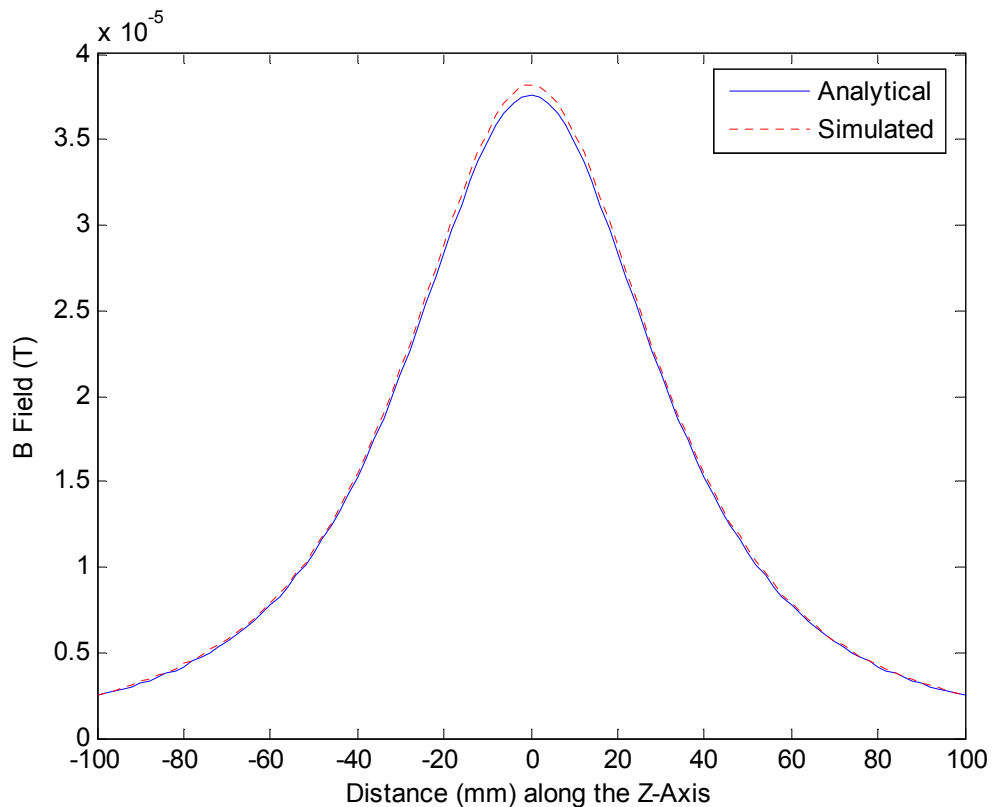


Figure 3.28: Comparison of Theoretical vs. Simulated Value of the B Field

3.5 Generating Array Field Data

Once the proper power scaling values are found and imported into HFSS, all field data generated will now take into account the particular lumped element configuration defined in the circuit model in Matlab. Ansoft HFSS includes a field calculator that can be used to compute quantities that are functions of the solved electric and magnetic field vectors. Expressions must be entered into the HFSS field calculator in Reverse Polish Notation (RPN). Once the proper field quantity is entered into the calculator, it can be plot on any surface or cross-section of the model.

In each of the coil array simulations, a single lumped element configuration (and thus set of power scaling values) is found to properly tune and match each individual channel of the array to the Larmor frequency. This is done by assuming an open circuit exists in each of the remaining three coil channels so that a single channel may be tuned and matched without the effects of coupling between the other channels. This assumption is justified by the use of the preamp decoupling technique described in section 2.4.2. While the preamplifiers are not a direct component of the coil circuit model, modeling each individual channel in this manner provides the effect of preamp decoupling however at a slightly exaggerated level then in reality.

Since only a single channel will be excited in HFSS at a time, the field plot for each individual channel must be combined to create an array field plot as:

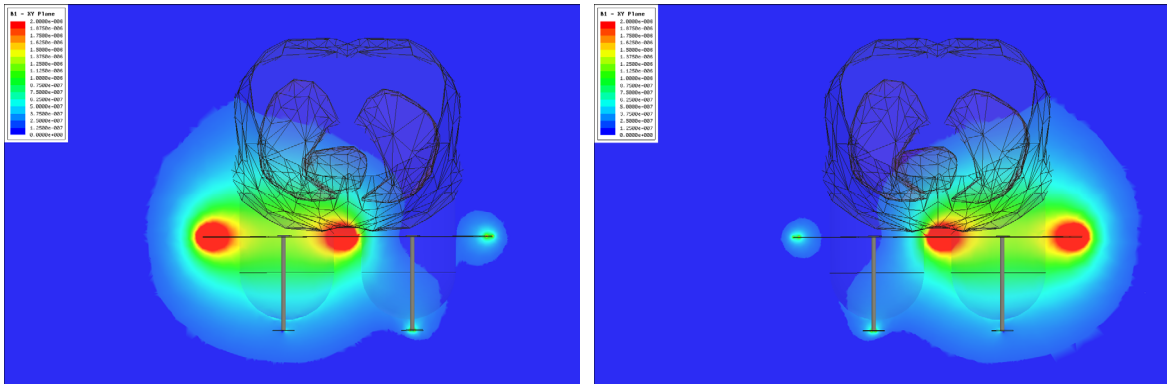
$$B_{Combined} = \sqrt{(B_{channel 1})^2 + (B_{channel 2})^2 + (B_{channel 3})^2 + (B_{channel 4})^2} \quad (3.13)$$

Unfortunately, HFSS does not include any functions to compute this quantity directly. There would need the ability of the HFSS field calculator to create expressions that are not only functions of the solved field quantities and space, but also functions of how much power is input into each lumped port of the HFSS model, as this is how each individual channel excitation is modeled.

HFSS does however have the ability to export any particular field plot generated by the user. Once a plot is generated on the desired surface or cross-section of the model, it can be saved in Ansoft's file format which will further be referred to as a "DSP" file, named for its three letter file extension ".dsp". An Ansoft DSP file is simply a text file that contains the mesh and field data of the plot in a format similar but not equivalent to the NASTRAN standard for defining a mesh by nodes and their interconnections. The DSP file contains three main sets of data – "Nodes", the list of 3D Cartesian coordinates, "Elements", the list of node interconnections and "Element Solution", the list of field values. For the purposes of combining field plot data, only the Element Solution dataset will need to be extracted.

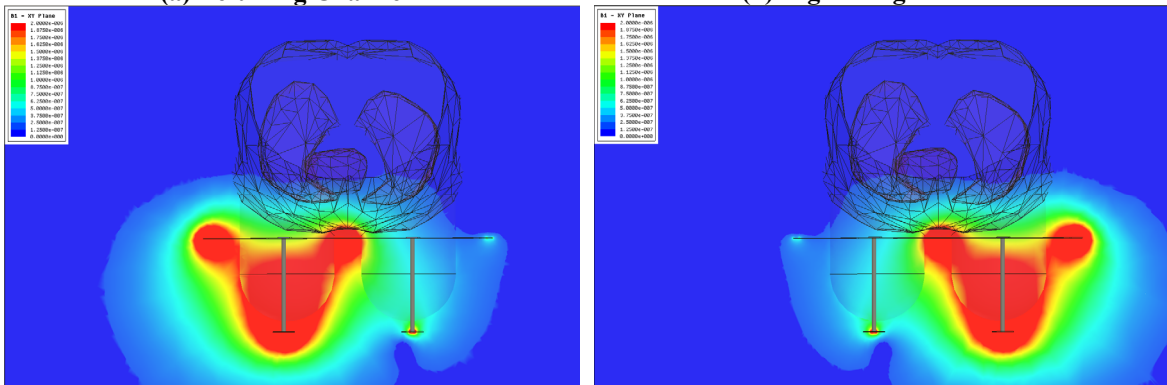
A Matlab function named "dspread" was written that can parse the Element Solution data from the DSP file and then load it as a variable in Matlab. A field plot file for each of the four channel excitations is saved and read by this function to extract its Element Solution dataset. Once in the Matlab workspace, the four datasets can now easily be combined as per (3.13). This resultant combined dataset is then written into one of the four existing DSP files thus overwriting the original Element Solution data using a new function named "dspwrite". This now modified DSP file can be opened in HFSS to view the combined field plot. Figure 3.29 shows the individual field plots for each of the four channel excitations plot on a cross-section of the transverse plane where (a) is the left ring channel, (b) is the right ring channel, (c) is the left strap channel, and (d) is the right strap channel. The combined field plot generated using this method can be seen in Figure 3.30.

This method will work for combining any number of field plots as long as they are from the same simulation and plot on the same geometry. The only difference between the field plots to be combined must be the set of power scaling values entered into HFSS to generate the individual plot.



(a) Left Ring Channel

(b) Right Ring Channel



(c) Left Strap Channel

(d) Right Strap Channel

Figure 3.29: Example Individual Field Plots per Channel

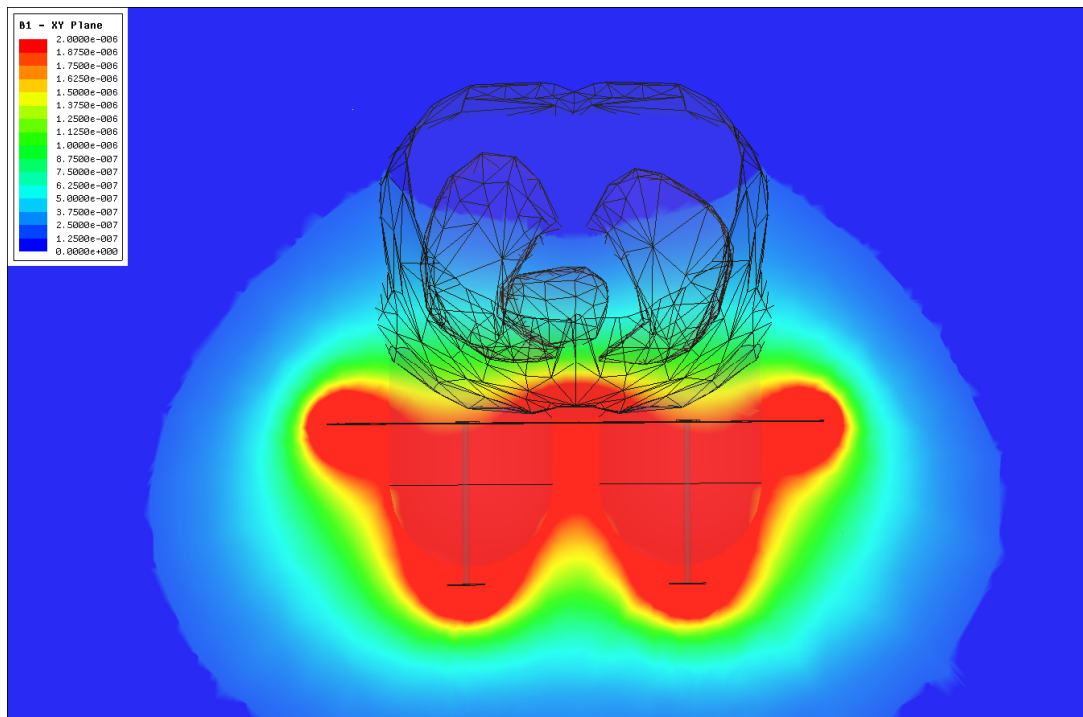


Figure 3.30: Example Combined Array Field Plot

3.6 Analyzing Simulation Results

3.6.1 B₁ Field and SNR

The goal of these simulations is to estimate the Signal to Noise Ratio (SNR) for a given coil design. The SNR is the most important figure of merit in comparing MRI coil designs as it directly relates to the quality of the image generated by the coil. While this simulation method can not directly compute the SNR of a given coil design, it utilizes the strength of what is known as the B_1 field as a quantity that can be shown to be relatively proportional to SNR. This field quantity is that of the circularly polarized components of the magnetic field which contribute to the excitation of the nuclei imaged. This field quantity can be computed as:

$$B_1 = \frac{1}{2}(B_x - jB_y) \quad (3.14)$$

The strength of the generated B₁ field relates to the SNR of a single coil as follows:

$$SNR \approx \frac{B_1}{\sqrt{P}} \quad (3.15)$$

Since the power being transmit into each coil is the same in each simulation, a linear relation can be used to estimate the SNR in terms of the B_1 field strength. Therefore, the larger the B_1 field found over a particular ROI will then correspond to a higher SNR calculated in the same ROI when measured in a MR scanner. This expression has been shown to be accurate when evaluating single channel coils. However, a more accurate method of computing the SNR of an array of coils involves computation of the mutual resistance matrix of the array as described by L. Wald [15]. This method was not used in this thesis due to the added complexity of generating the mutual resistance matrix of the coil model. There are also two methods that will be used to evaluate the field strength. The first is to use the value of the field at a single point in the middle of a single breast. The second is to average the value of the B_1 field in a cross section of the entire breast area. Both values will be used later in comparing simulation results.

3.6.2 Surface Current Density

Plots of the magnitude of the surface current density J_{surf} are useful for visualizing the flow of current in the coil as a check to verify current is flowing in the expected manner. In Figure 3.31 (a) and (c), J_{surf} is calculated and plot on the coil loops for the left ring and left strap channels respectively. In Figure 3.31 (b) and (d), the expected current flow for the ring and strap excitations is shown. It can be seen that for the ring mode excitation, the majority of the current density resides in the ring loop. For the strap mode excitation, the current density though the “strap” portion of the loop is about twice as strong as it is along the “ring” portion of the loop, showing how the current splits equally around the loop and is combined in the strap.

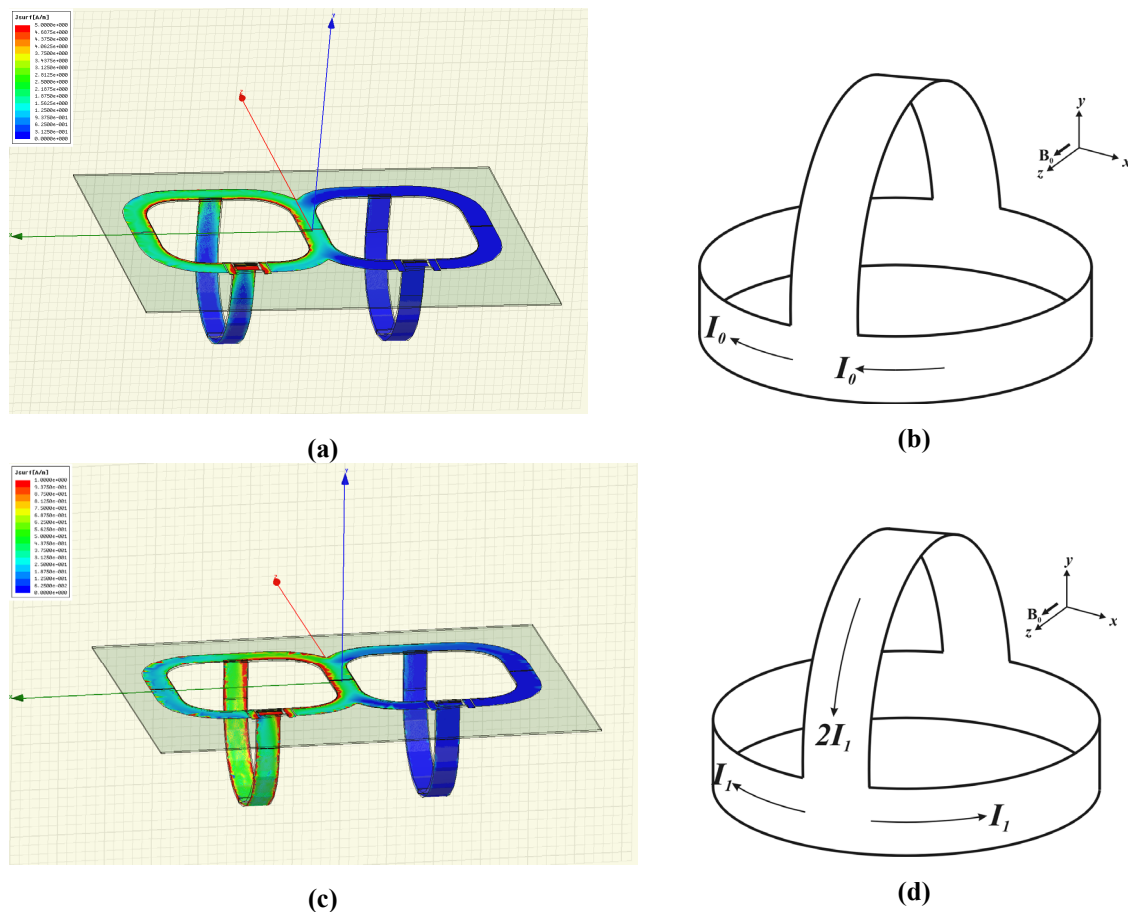


Figure 3.31: Calculated Surface Current Density and Expected Current Flow

3.6.3 Axillary Field Coverage

One important performance characteristic for this four channel breast coil array is the axillary field coverage. The axilla, seen in Figure 3.32, is the area of the human body directly under the joint where the arm connects to the shoulder. This area is of key importance in diagnostic breast imaging as it contains lymph nodes where the cancer presents itself in a majority of breast cancer cases. [16]

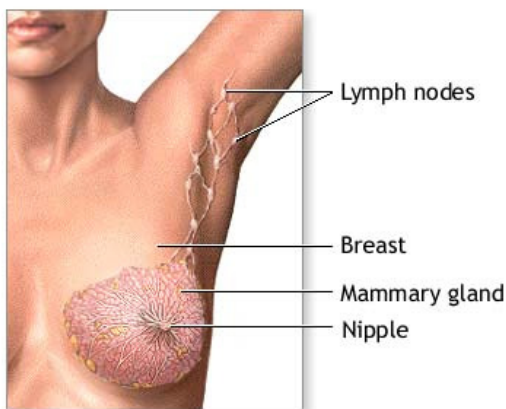


Figure 3.32: Human Axilla

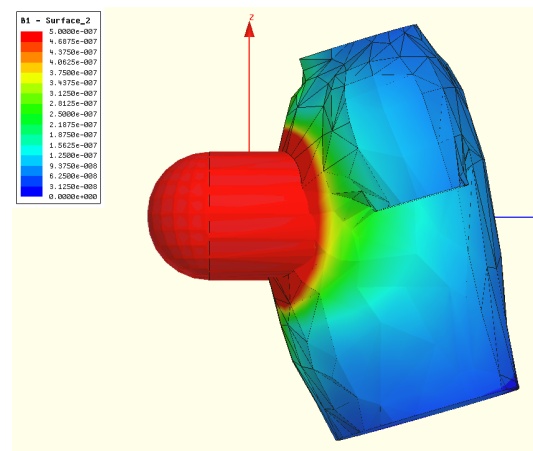


Figure 3.33: B_1 Field on the Surface of the Human Body Model

Shown in Figure 3.33, the magnitude of the B_1 field can be plot on the surface of the human body model. With this plot, the axillary field coverage for each design can be used as a tool for comparing the performance of various designs.

3.6.4 Quadrature Field Performance

This coil design can be configured in two modes of operation, as either a linear array, or a quadrature array. By default, the coil is setup as a linear array; all four channels are operated independently. In an effort to increase SNR, this coil can also be configured as a two channel quadrature array. In this configuration, each set of ring and strap coils are combined in what is known as the quadrature mode, effectively reducing the array to two channels. The ring and strap channels can be combined in this manner because the ring and strap channels were designed to create magnetic fields that are oriented perpendicular to each other in the ROI. Figure 3.34 shows a vector plot of the magnetic field in the ROI. These plots were generated in the simulation of the prototype coil. The direction of the magnetic field is indicated by the direction of the arrows. Figure 3.34(a) shows the vector plot for the left ring channel. Its field is oriented in the Y-axis, looking out of the page. Figure 3.34(b) shows the vector plot for the left strap channel. Its field is oriented in the X-axis.

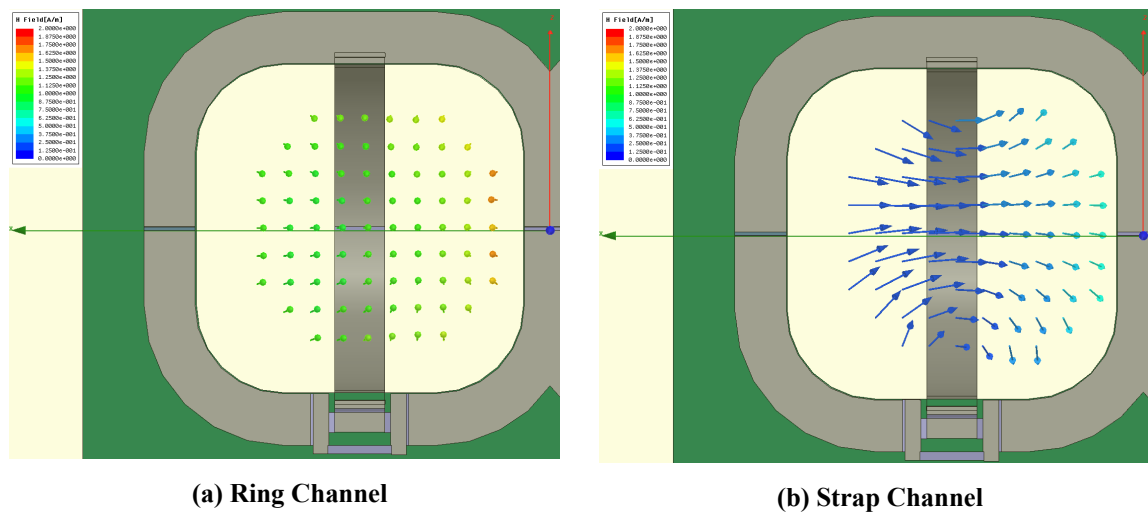


Figure 3.34: Vector Plots of the Magnetic Field within the ROI

In the quadrature mode, these perpendicular fields are driven 90 degrees out of phase of one another to create a rotating magnetic field in sync with the procession of the nuclei in the ROI. This creates an increase in the efficiency of the coil for which the result is an NMR signal with a theoretical $\sqrt{2}$ (or 3dB) increase in B_1 field strength. The actual gain will be based on how perfectly perpendicular the generated magnetic fields are from one another. A perfect $\sqrt{2}$ increase is not typically achievable in the entire imaging ROI due to design issues; since arranging the coils to generate perfectly perpendicular magnetic fields within the entire ROI would limit patient access or not be feasible to construct. For example, in Figure 3.34(b), one can see how all of the arrows indicating the direction of the magnetic field are not oriented perfectly with the X-axis throughout the entire ROI.

Quadrature combination is physically realized by using a standard 90 degree hybrid combiner, a four port RF device characterized by the following S-Parameter matrix:

$$S = \frac{-1}{\sqrt{2}} \begin{bmatrix} 0 & j & 1 & 0 \\ j & 0 & 0 & 1 \\ 1 & 0 & 0 & j \\ 0 & 1 & j & 0 \end{bmatrix} \quad (3.16)$$

Using the newly developed MATLAB tools to process HFSS field plot data described in section 3.5, the quadrature mode performance can be evaluated and compared to non-quadrature mode. To do this, four plots must be made of each of the channels. Those four plots include $\text{Re}(B_x)$, $\text{Im}(B_x)$, $\text{Re}(B_y)$, and $\text{Im}(B_y)$. The quadrature combined B_1 field is then computed as:

$$B_{\text{Combined-X-Ring-Strap-Left}} = (\text{Re}(B_{x\text{-Ring}}) + j \cdot \text{Im}(B_{x\text{-Ring}}) + j(\text{Re}(B_{x\text{-Strap}}) + j \cdot \text{Im}(B_{x\text{-strap}}))) \quad (3.17)$$

$$B_{\text{Combined-Y-Ring-Strap-Left}} = (\text{Re}(B_{y\text{-Ring}}) + j \cdot \text{Im}(B_{y\text{-Ring}}) + j(\text{Re}(B_{y\text{-Strap}}) + j \cdot \text{Im}(B_{y\text{-strap}}))) \quad (3.18)$$

and

$$B_{1\text{-Quad-Left}} = \left| \frac{1}{2} \cdot (B_{\text{Combined-X-Ring-Strap-Left}} + j \cdot B_{\text{Combined-Y-Ring-Strap-Left}}) \right| \quad (3.19)$$

This results in a field plot of the quadrature combination of the left-side ring-strap pair. The process is repeated for the right half of the coil. These two field plot datasets are then combined as per Section 3.5 to form a complete array field plot. Once this field plot has been created, the original non-quadrature field plot and the new quadrature field plot can be compared by dividing the quadrature field data over the non-quadrature field data within MATLAB. This new field plot will now show where the actual improvement or degradation in B_1 field strength occurs. This plot is shown in Figure 3.35. The plot is scaled from 0.5 to 1.5, showing a +/- 50% change in B_1 field strength.

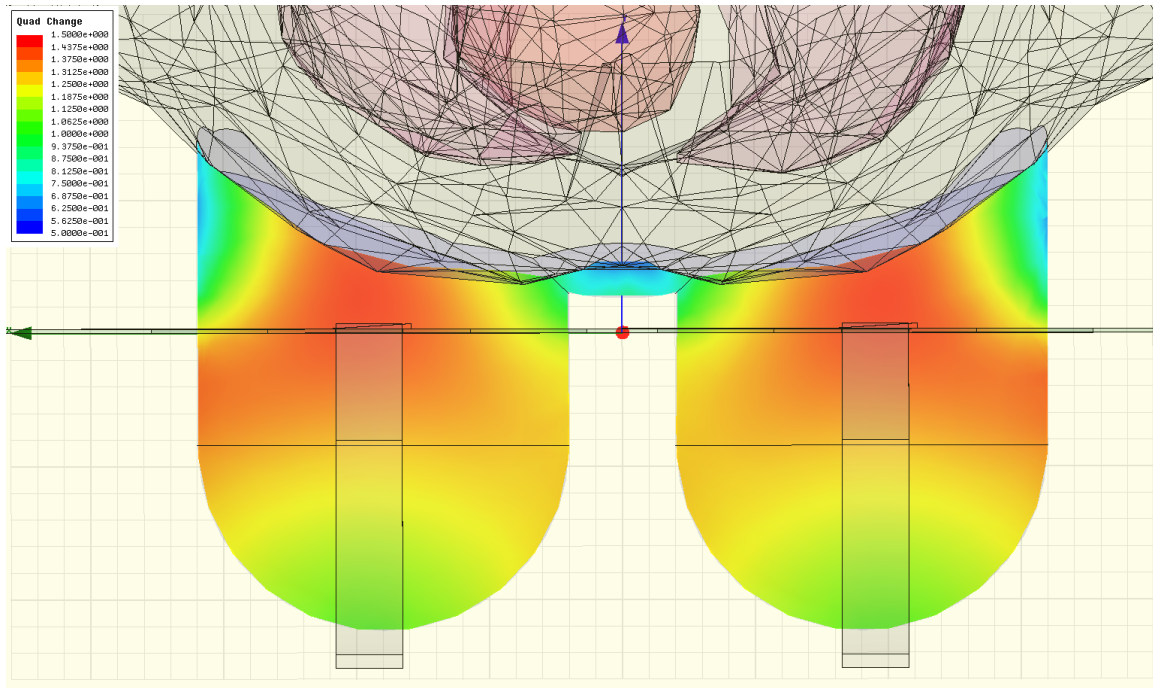


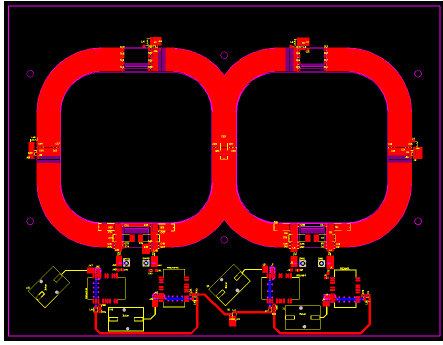
Figure 3.35: Example Quadrature Field Difference Plot

4 Simulation Models

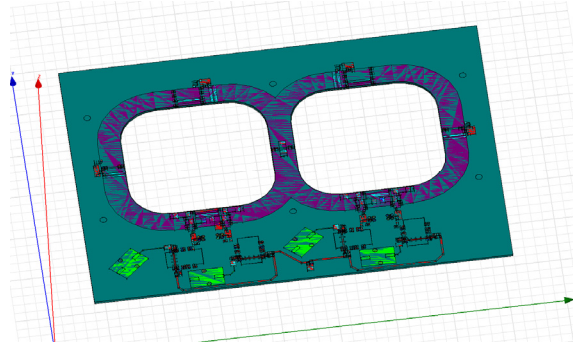
4.1 Prototype Simulation

4.1.1 HFSS Model

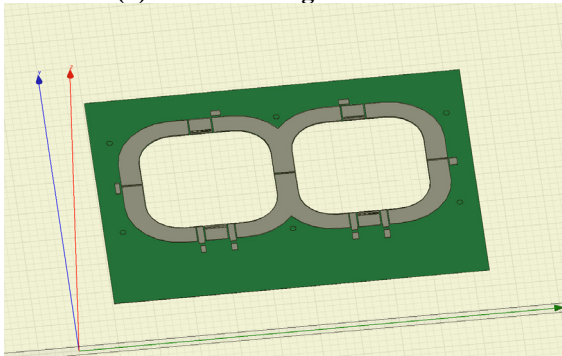
To begin modeling of the existing prototype coil, existing CAD drawings were imported into HFSS. The PCB was imported from an existing 2D DXF file that was exported from the PCB program Protel (Figure 4.1a). The 2D model is extruded to 3D by HFSS with each 2D layer assigned its own thickness (Figure 4.1b). Once imported, the model is automatically edited to remove small features such as chamfers and small screw holes. The model is then manually edited to remove the remaining features that were missed by the automatic model healing done by HFSS. Finally the 2D layers of the PCB and the copper traces are extruded into 3D (Figure 4.1c). The straps were imported from a 3D solid model exported from Solidworks (Figure 4.1d). The models are imported into HFSS and moved into their proper position (Figure 4.1e, f). Using the strap model as a geometrical reference, a thin 3D sheet of copper is extruded on the surface of the strap to model the copper tape used to make the strap loops. The copper traces are then united together as a single object (Figure 4.1g). The next step is to create the 2D sheets necessary to define the ports. The sheet for each break or port containing a lumped element is added and assigned the HFSS lumped port boundary condition (Figure 4.1h). The remaining simulation parameters are set in HFSS such as the radiation boundary conditions, simulation frequency, and convergence criteria. The final step is to import the human body model to be used as the load for the coil. The breast augmented human torso model as described by section 3.3.1 is used. The completed model can be seen in Figure 4.2.



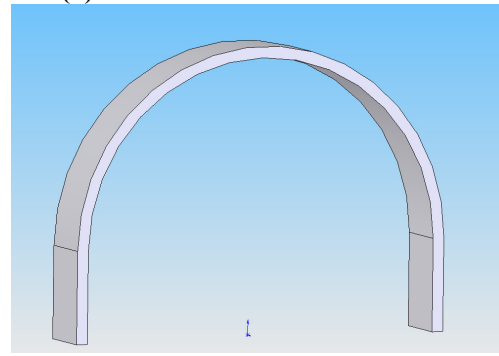
(a) DXF Drawing from Protel



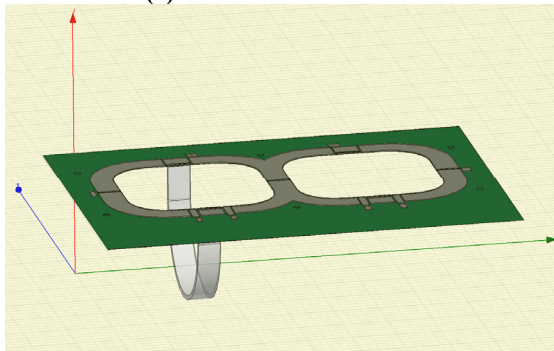
(b) Converted DXF to Solid Model



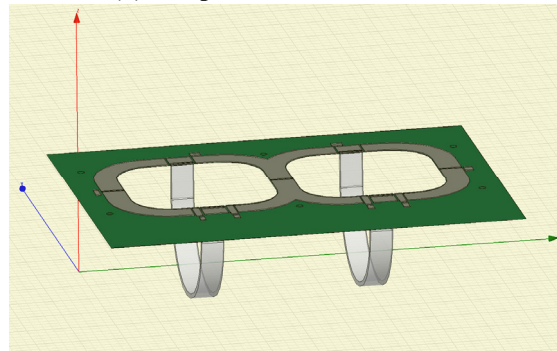
(c) Cleaned Solid Model



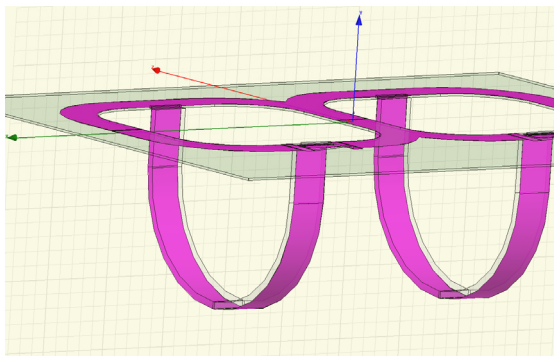
(d) Strap Model in Solidworks



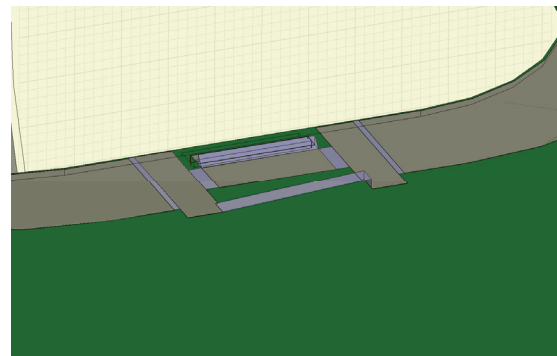
(e) Importing the Strap Model



(f) Completed Strap Placement



(g) Extruded Copper Layer



(h) Completed Port Definitions

Figure 4.1: Creating the HFSS Model of the Existing Prototype

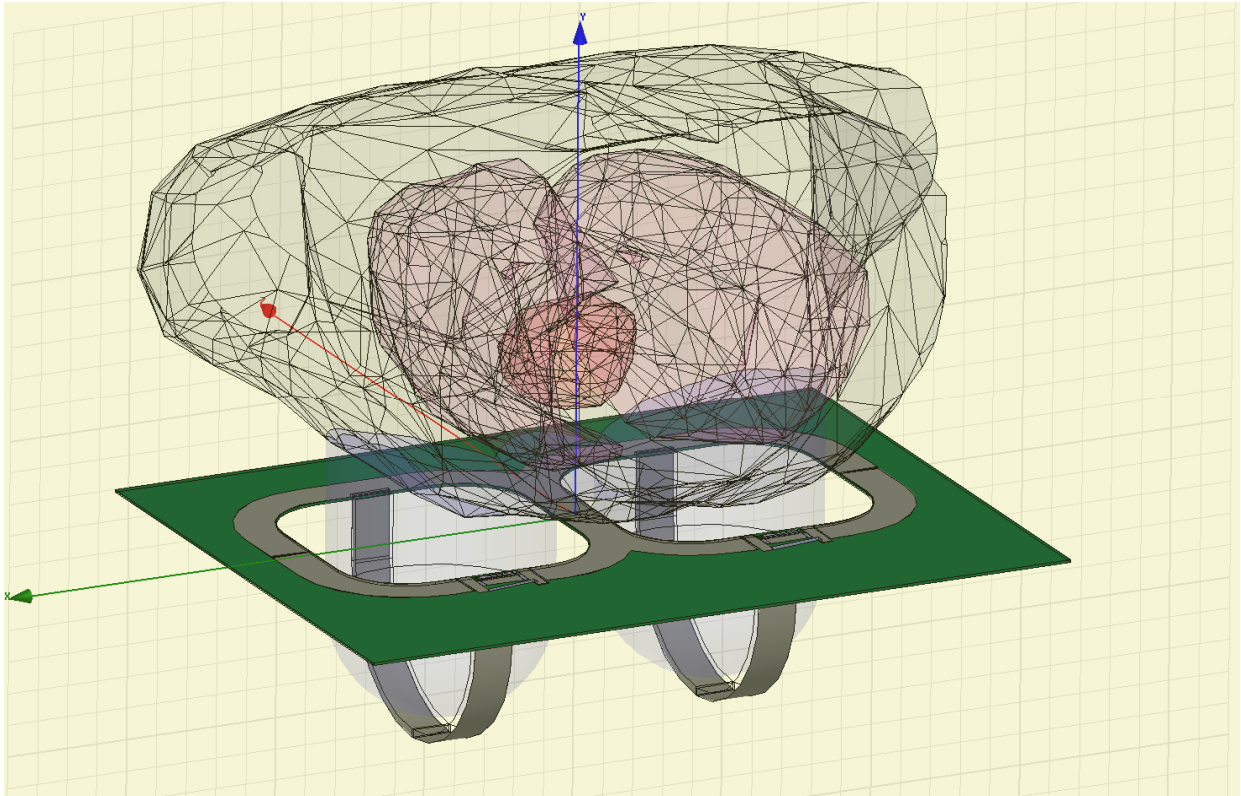


Figure 4.2: Completed HFSS Model of Existing Prototype

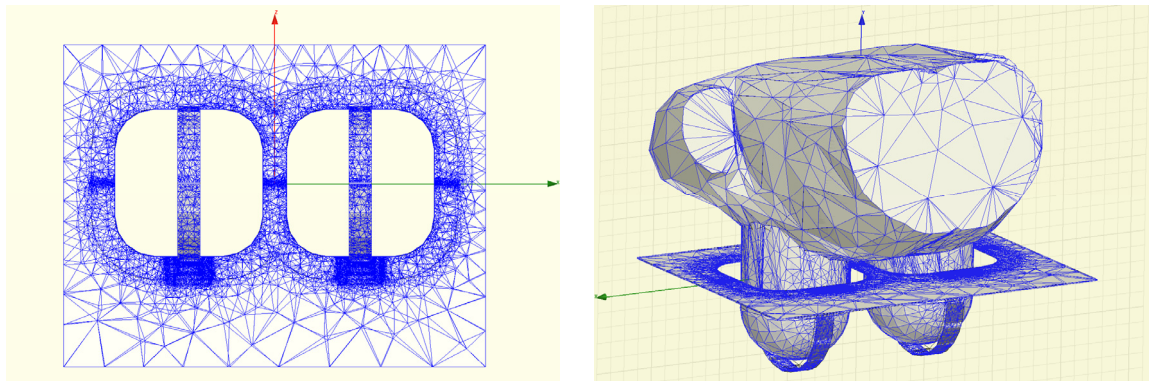
4.1.2 Simulation Results

The simulation completed with the following parameters reported in Table 4.1.

Table 4.1: Simulation Data of Prototype Design

Simulation Time (h:mm:ss)	6:50:19
Tetrahedra	303588
Convergence (Max Mag. Delta S)	0.0009 @ 11 Passes
Peak RAM Usage	11.7 GB

Views of the mesh can be seen below in Figure 4.3. The results of the adaptive mesh operation can be seen in the variation of the mesh density around the structure. Although the exact mesh algorithm is unknown, the most densely meshed areas are the ports intended for lumped elements and those areas carrying the largest currents. Overall there are over three hundred thousand tetrahedra creating the mesh. With this final mesh, the resulting FEM solution was able to obtain less than 0.1% change in the maximum magnitude change in S-Parameters from the previous iteration.



(a) Coil Top View

(b) Coil and Load, Isometric View

Figure 4.3: Mesh Plots of the Prototype Simulation

4.1.3 S-Parameters

Figure 4.4 shows the calculated S-Parameters for each of the four channels. These plots were generated using the method described in section 3.4.1. Each channel is tuned to the Larmor frequency and matched to achieve a return loss of -45dB.

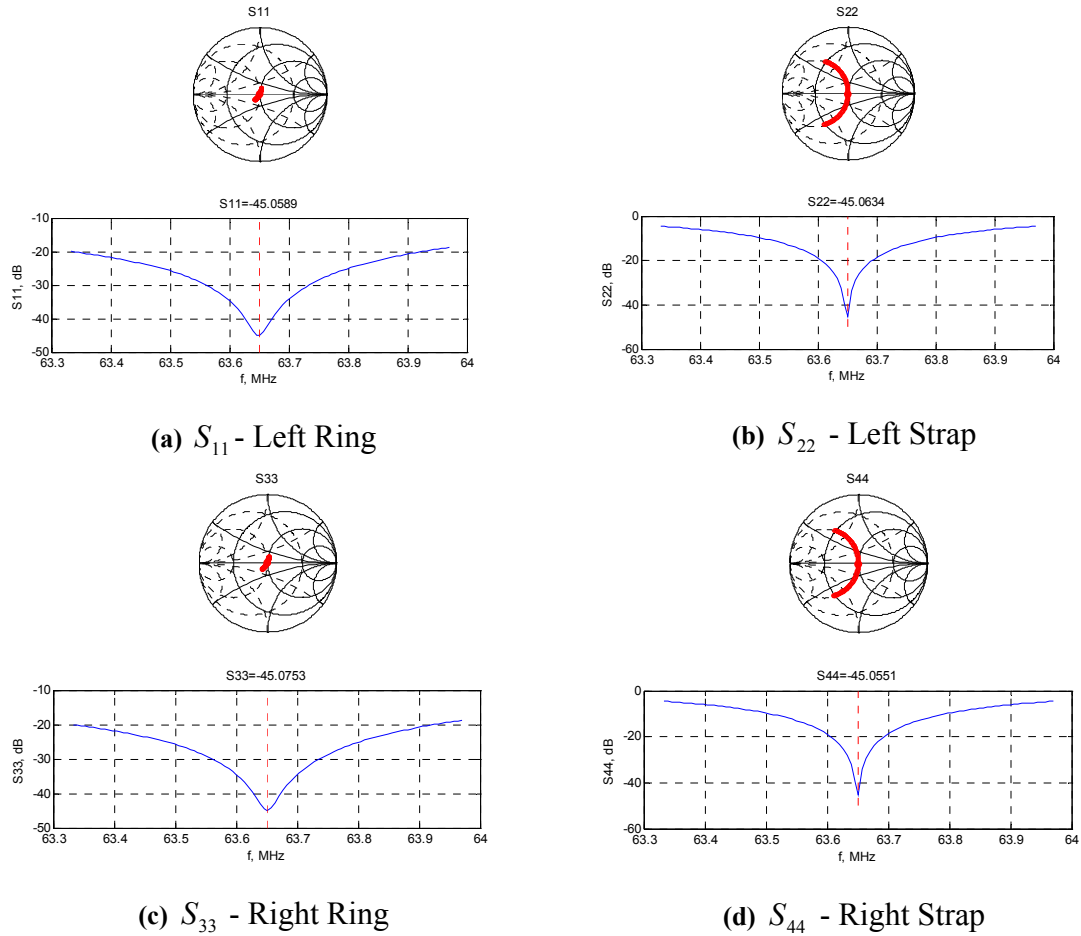


Figure 4.4: S-Parameters of the Prototype Coil Array

4.1.4 Field Data

Surface Current Density

In Figure 4.5, the magnitude of the surface current density is plot for each channel of the array. These plots are useful for visualizing how the currents flow for a given channel excitation. It can be seen that the currents flow as expected as per Figure 2.6 and Figure 2.7.

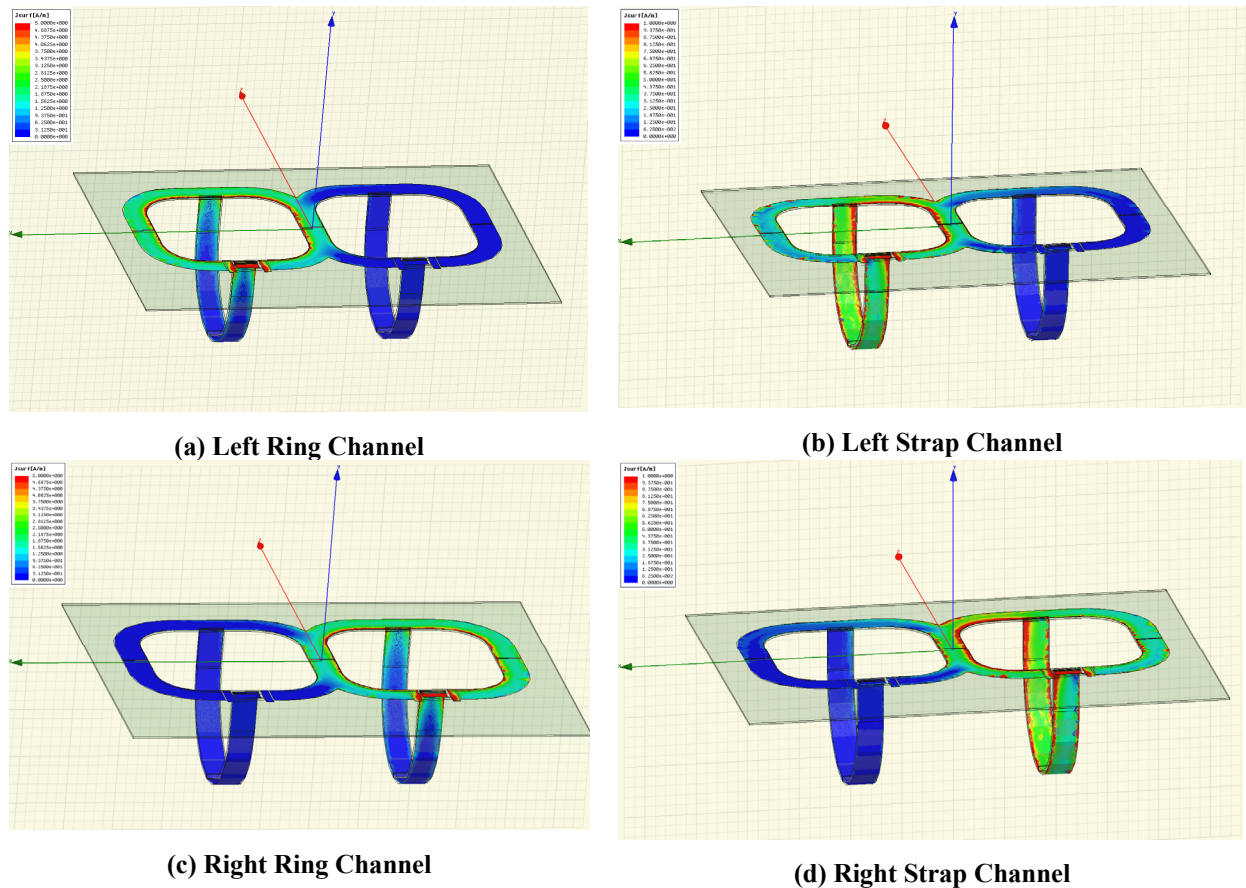


Figure 4.5: Prototype Coil – Surface Current Density per Channel

Transverse Plane B1 Field

Figure 4.6 shows the B_1 field generated by each of the four coil channels in the array within the transverse plane of the subject. These field plots are combined using the methods and assumptions made in section 3.5 to generate Figure 4.7. It is this combined field data that will be used as a basis for the comparison of each coil design.

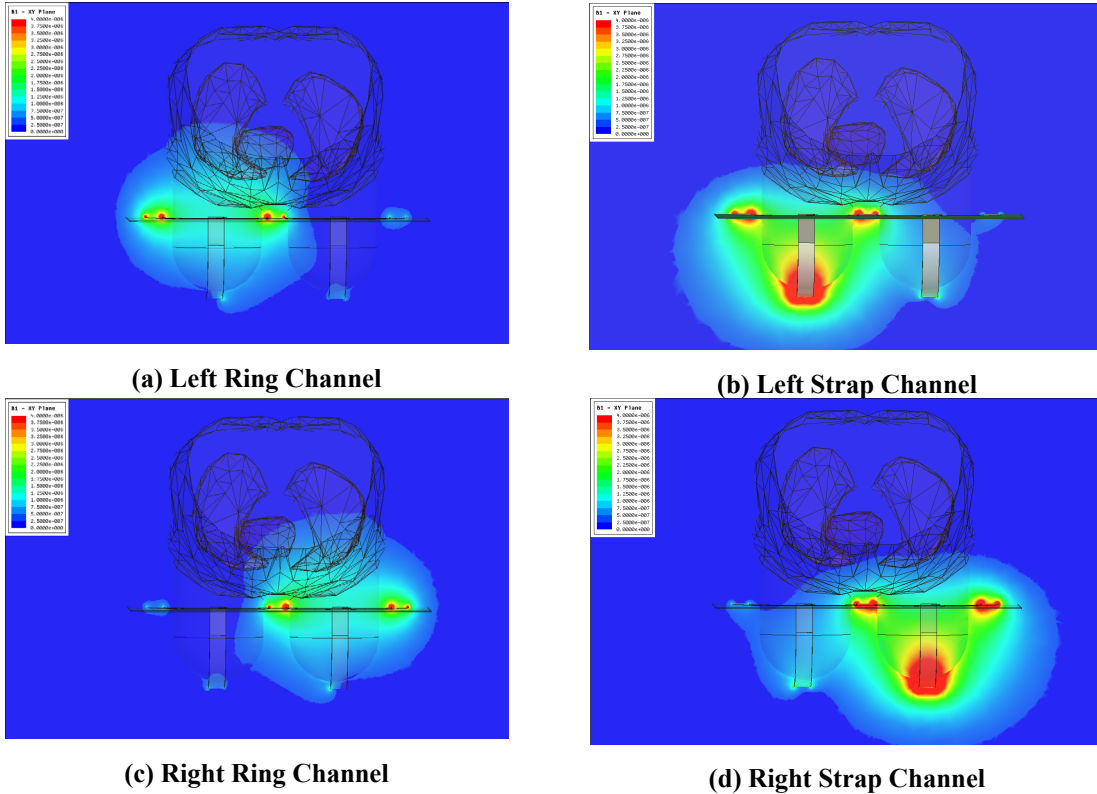


Figure 4.6: Prototype Coil – B1 Field per Channel – Transverse Plane

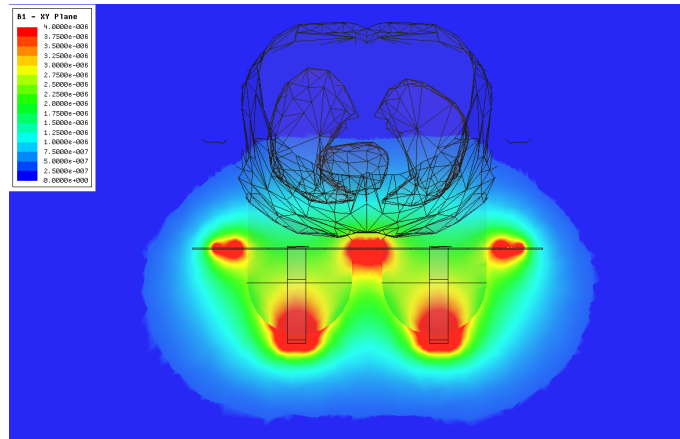


Figure 4.7: Prototype Coil – Combined B1 Field – Transverse Plane

Axillary Field Coverage

Figure 4.8 shows the B_1 field of the coil array plot on the surface of the human body model. The plot is scaled as to show the area where good field coverage as achieved. It can be seen that this prototype coil's field of view extends only slightly outside of the breasts and into the axilla.

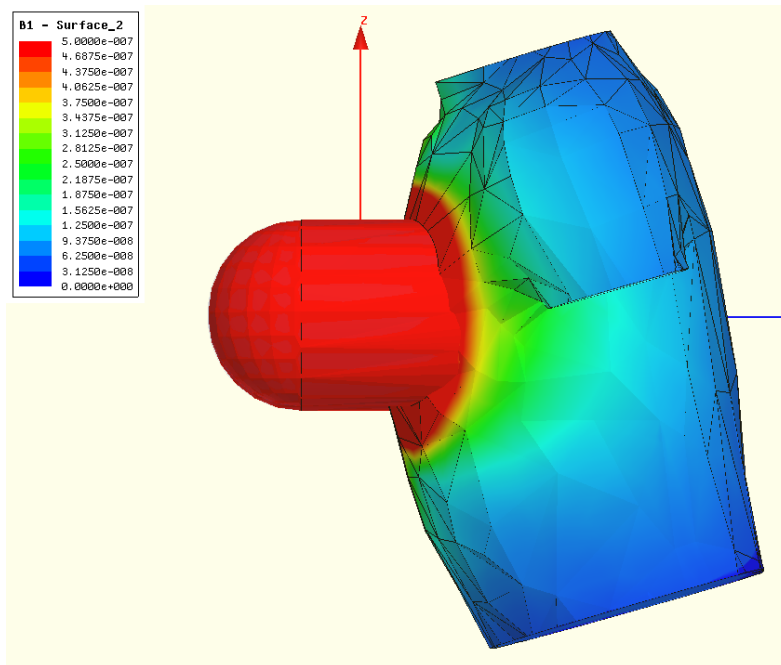


Figure 4.8: Prototype Coil – B_1 Field on the Surface of the Body

Quadrature Field Performance

The quadrature difference plot can be seen in Figure 4.9. This plot was generated using the method described in Section 3.6.4. The plot is scaled from 0.5 to 1.5, showing a +/- 50% change in B_1 field strength. It can be seen that the increase in the B_1 field strength does come close to its theoretical maximum of 41% in the area in the center of each breast. However, this quadrature configuration also causes a decrease in the chest and axilla up to 25%. Here a design trade-off exists where the increased SNR of the quadrature coil array must be weighed against the decrease in field of view of the axilla.

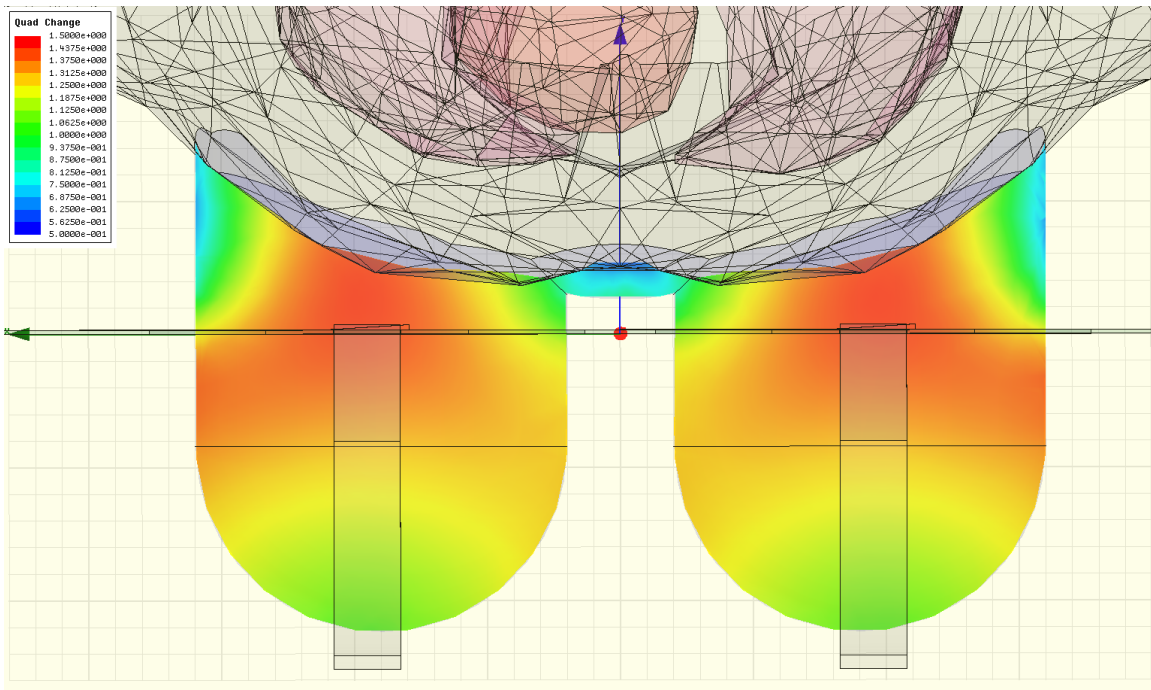


Figure 4.9: Prototype Coil – Quadrature Combined Field Increase

4.2 New Design Simulation

4.2.1 HFSS Model

In the new design model, all geometries were created within HFSS. The more complex model features, such as the PCB and PCB traces were created by importing the former from Solidworks, and using points and lines of the model as references to create features within HFSS. The former is not meshed due to resource limitations and is included only for visual and model creating references.

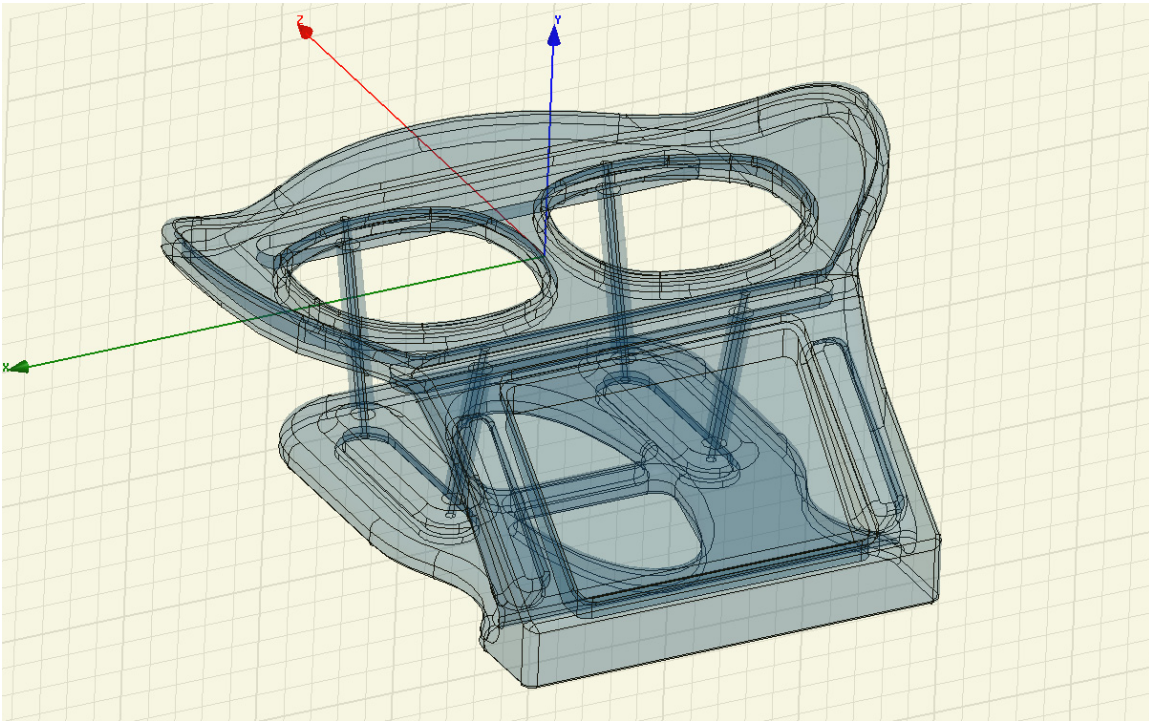


Figure 4.10: Former CAD Model used as a Basis for HFSS Model Building

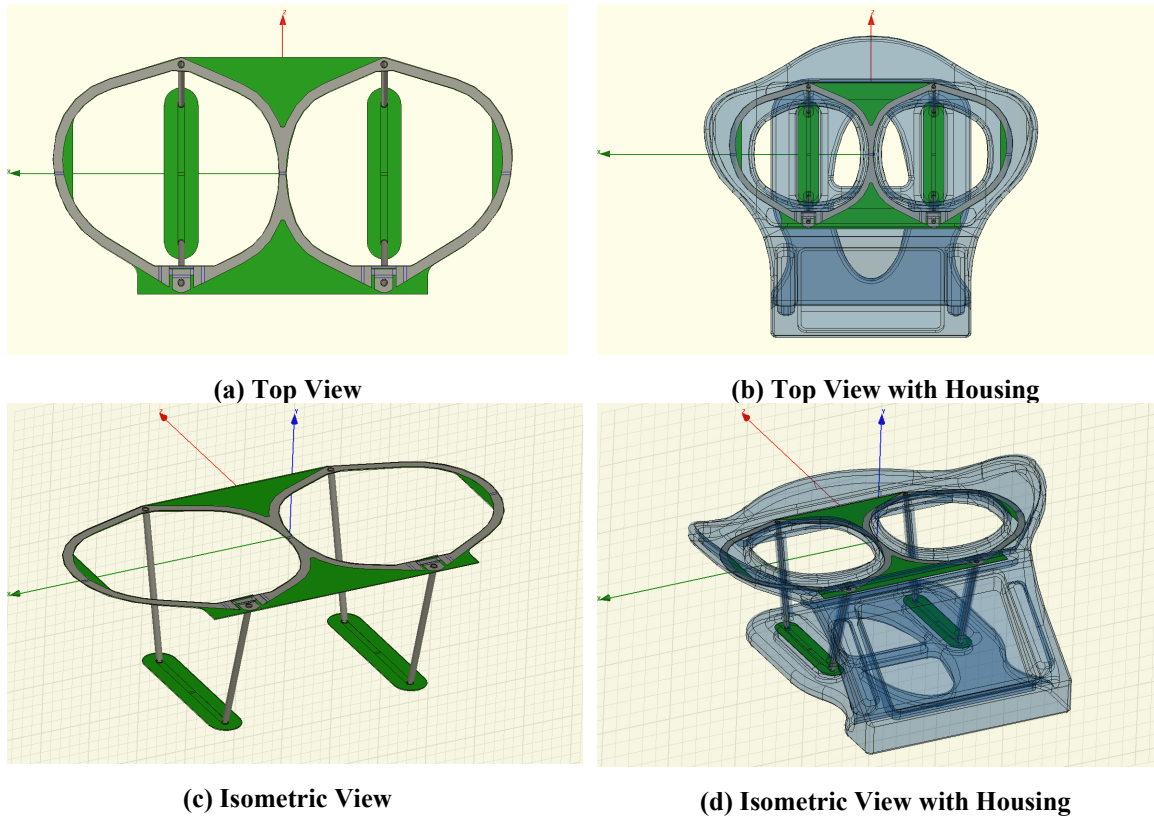


Figure 4.11: HFSS Model of the New Coil Design

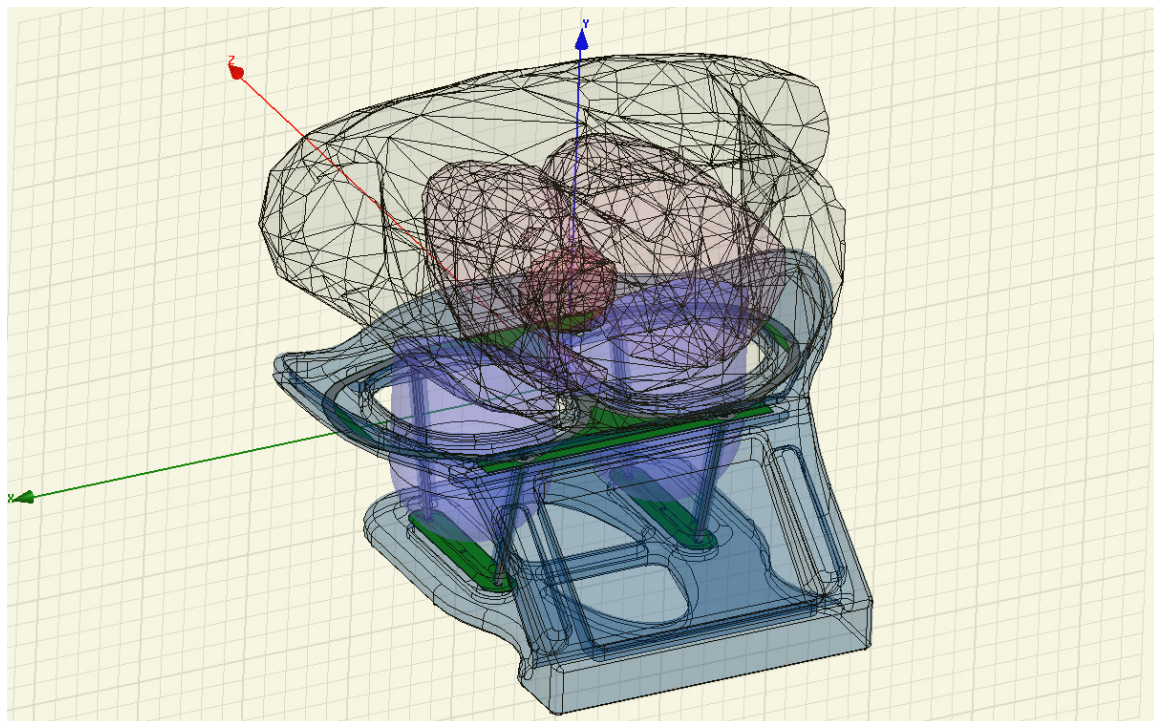


Figure 4.12: Completed HFSS Model with Human Body Load

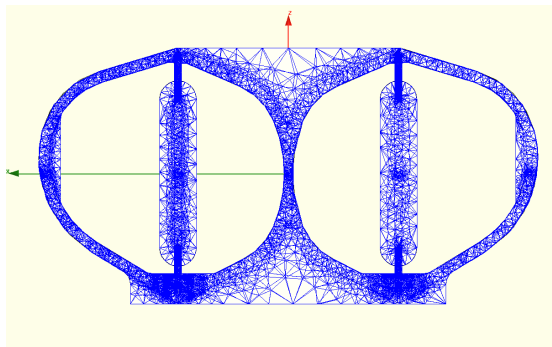
4.2.2 Simulation Results

The simulation completed successfully with the following parameters reported in Table 4.2.

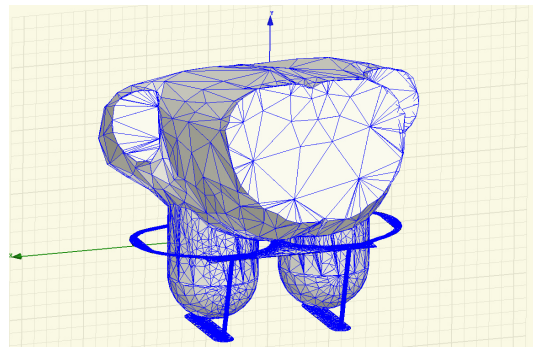
Table 4.2: Simulation Data for the New Coil Design

Simulation Time (h:mm:ss)	9:53:31
Tetrahedra	377396
Convergence (Max Mag. Delta S)	0.0015 @ 12 Passes
Peak RAM Usage	14.6 GB

Views of the mesh can be seen below in Figure 4.13. The results of the adaptive mesh operation can be seen in the variation of the mesh density around the structure. Although the exact mesh algorithm is unknown, the most densely meshed areas are the ports intended for lumped elements and those areas carrying the largest currents. Overall there are over three hundred thousand tetrahedra creating the mesh. With this final mesh, the resulting FEM solution was able to obtain less than 0.2% change in the maximum magnitude change in S-Parameters from the previous iteration.



(a) Coil Top View



(b) Coil and Load, Isometric View

Figure 4.13: Mesh Plots of the New Design Simulation

4.2.3 S-Parameters

Figure 4.14 shows the calculated S-Parameters for each of the four channels. These plots were generated using the method described in section 3.4.1. Each channel is tuned to the Larmor frequency and matched to achieve a return loss of -45dB.

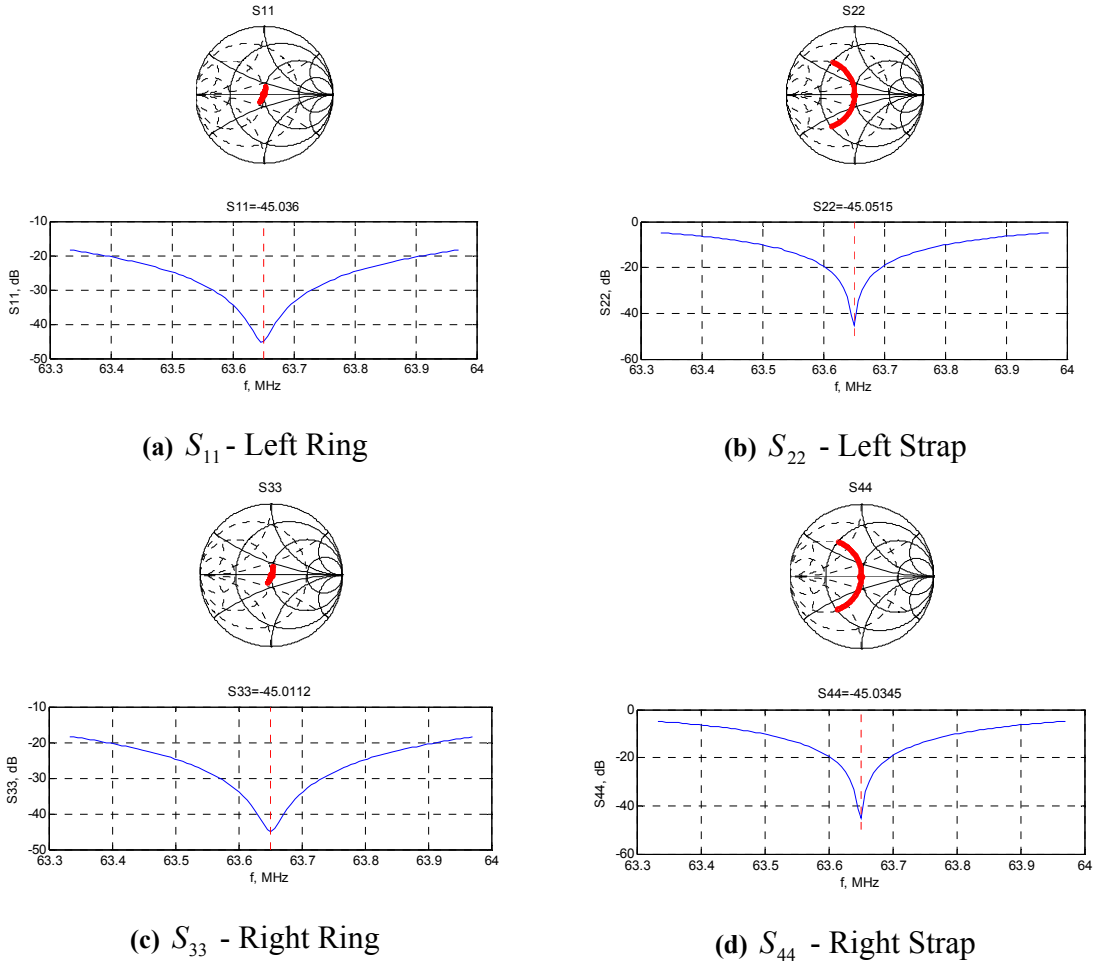


Figure 4.14: S-Parameters of the New Coil Design

4.2.4 Field Data

Surface Current Density

In Figure 4.15, the magnitude of the surface current density is plot for each channel of the array. These plots are useful for visualizing how the currents flow for a given channel excitation. It can be seen that the currents flow as expected as per Figure 2.6 and Figure 2.7.

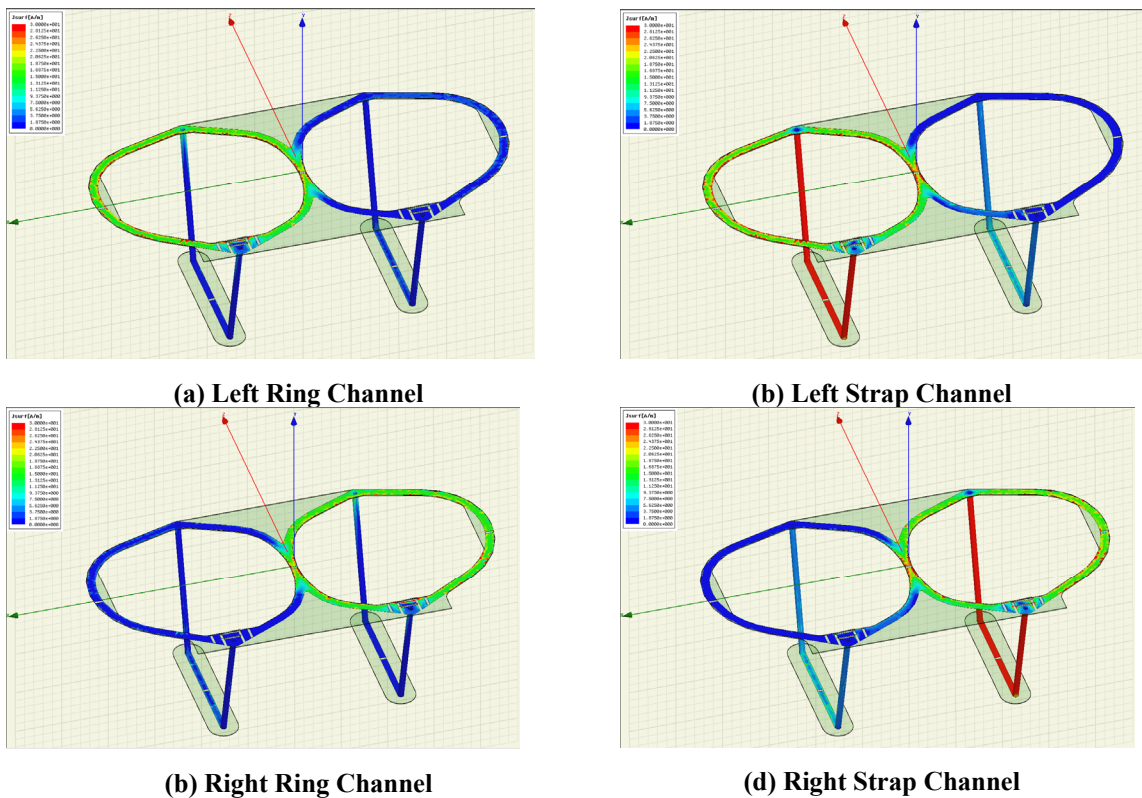


Figure 4.15: New Coil Design – Surface Current Density per Channel

Transverse Plane B1 Field

Figure 4.16 shows the B_1 field generated by each of the four coil channels in the array within the transverse plane of the subject. These field plots are combined using the methods and assumptions made in section 3.5 to generate Figure 4.17. It is this combined field data that will be used as a basis for the comparison of each coil design.

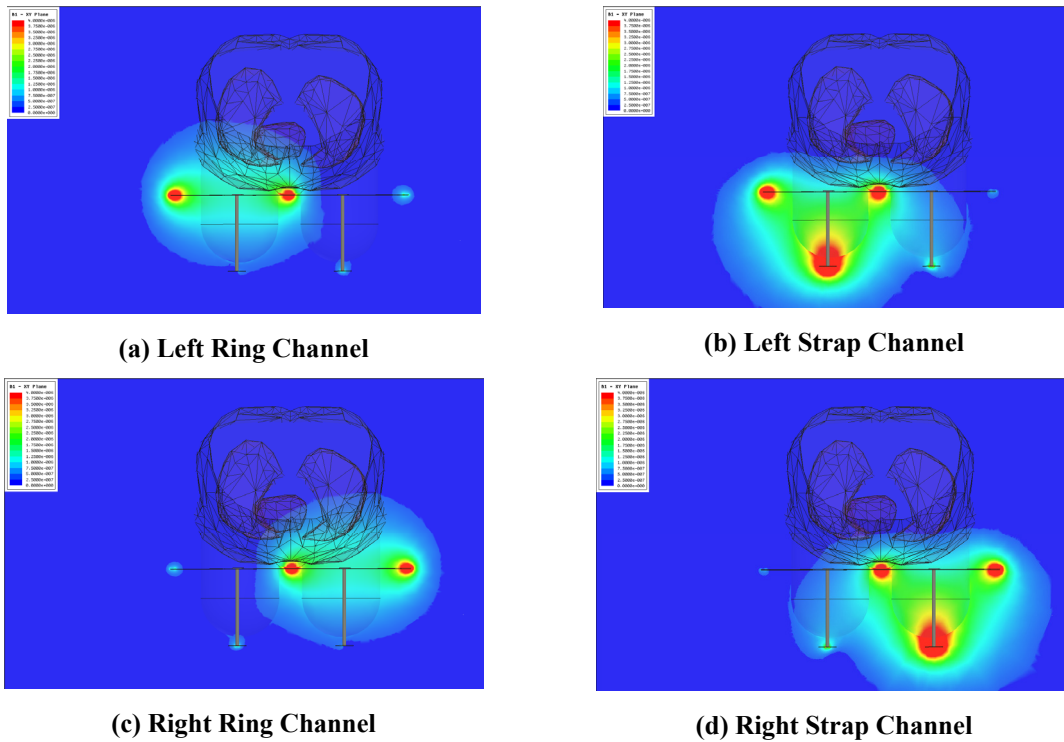


Figure 4.16: New Coil Design – B1 Field per Channel – Transverse Plane

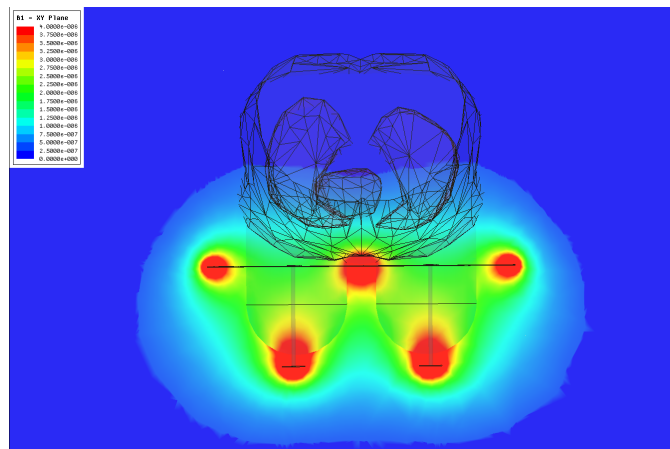


Figure 4.17: New Coil Design – Combined B1 Field – Transverse Plane

Axillary Field Coverage

Figure 4.18 shows the B_1 field of the coil array plot on the surface of the human body model. The plot is scaled as to show the area where good field coverage as achieved. It can be seen that this prototype coil's field of view extends outside of the breasts and into the axilla.

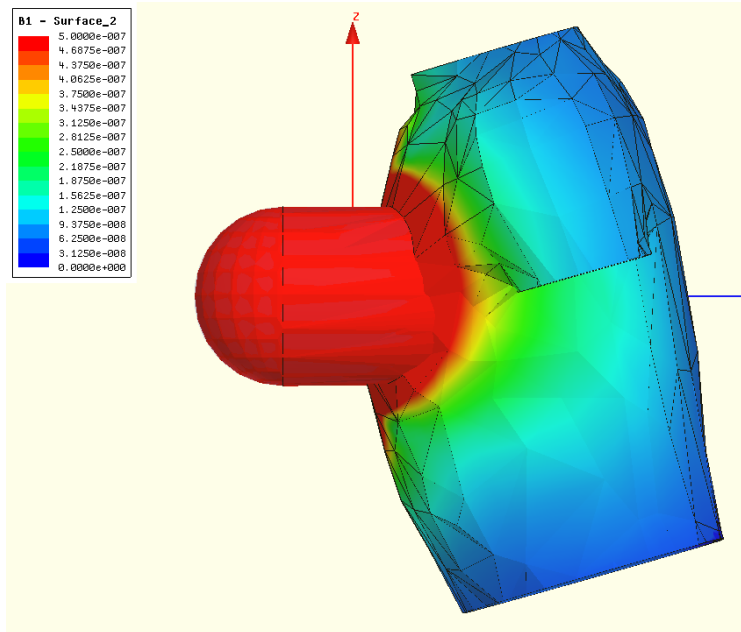


Figure 4.18: New Coil Design – B_1 Field on the Surface of the Body

Quadrature Field Performance

The quadrature difference plot can be seen in Figure 4.19. This plot was generated using the method described in section 3.6.4. The plot is scaled from 0.5 to 1.5, showing a +/- 50% change in B_1 field strength. It can be seen that the increase in the B_1 field strength does come close to its theoretical maximum of 41% in the area in the center of each breast. However, this quadrature configuration also causes a decrease in the chest and axilla up to 15%. Here a design trade-off exists where the increased SNR of the quadrature coil array must be weighed against the decrease in field of view of the axilla.

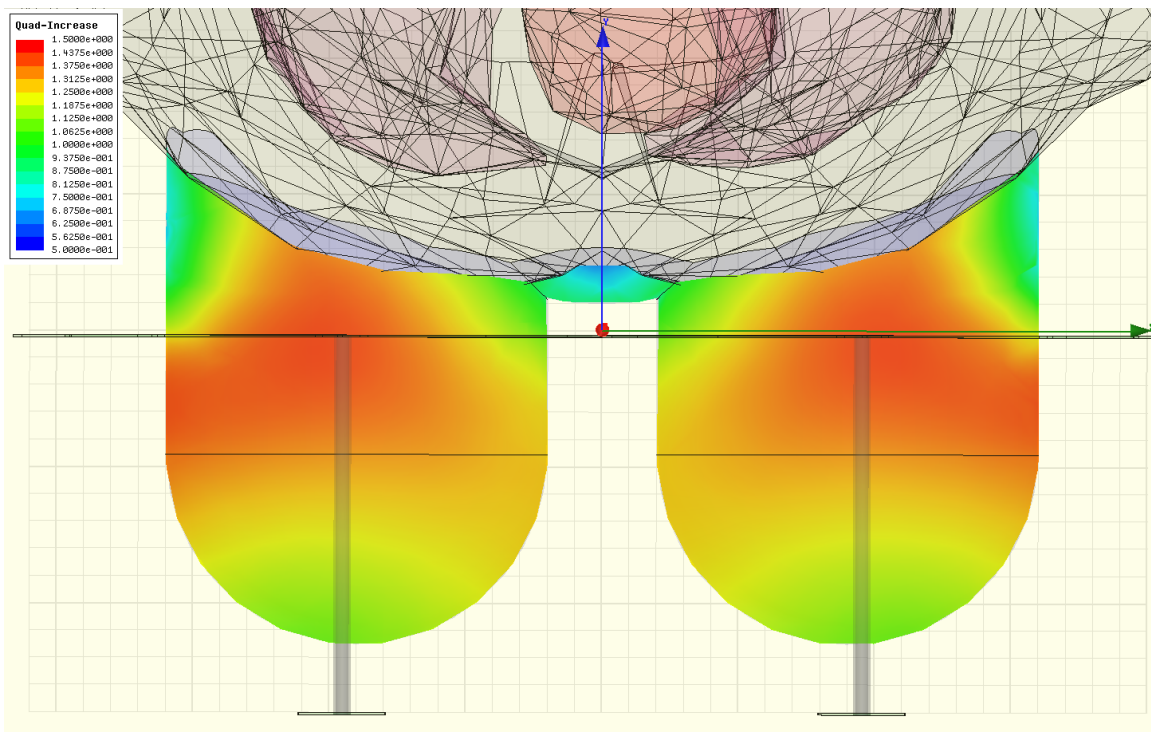


Figure 4.19: New Coil Design – Quadrature Combined Field Increase

4.3 Simulation Results

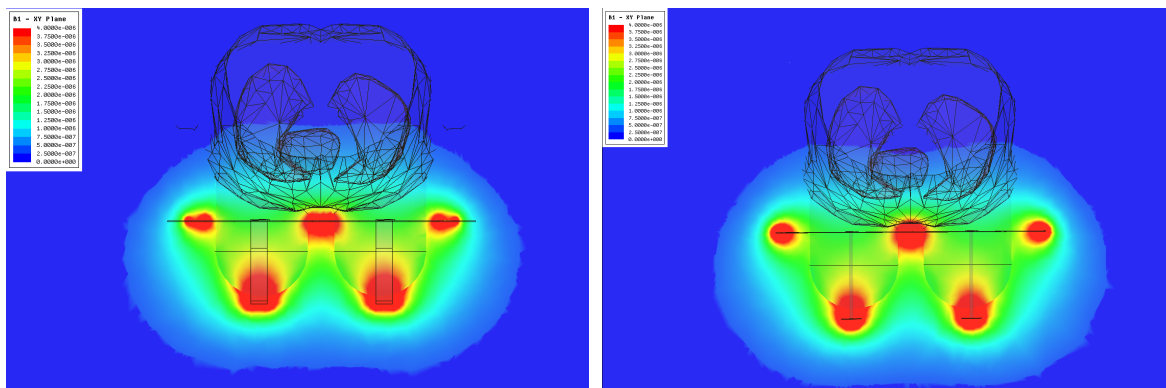
4.3.1 B₁ Field Strength Comparison

Two methods were used in analyzing the B_1 field strength simulation results. The first is to compare the value of the field as a single point in the ROI. The point used is located 40mm below the center of the Y-axis, centered in the left breast. This point was chosen due to the fact that the SNR calculation of the measured results will be taken in this area. The second method is to compare the mean value of the field in a cross-section of the breasts. This average value will take into account the performance of the coil over the entire ROI. Table 4.3 shows the results of these calculations. With both methods, the prototype coil simulation yielded approximately 10% higher B_1 field strength.

Table 4.3: B₁ Field Strength Comparison – Prototype vs. New Coil Design

	Prototype Coil	New Coil Design
Single Point	$2.74\mu T$	$2.51\mu T$
Mean B₁	$2.56\mu T$	$2.35\mu T$

To visually compare field coverage area, array plots of both designs can be seen in Figure 4.20. Comparing both designs, the field coverage is almost identical. Both coils should perform similar although it can be seen that the new design covers the chest and axilla with higher field strength, while the prototype design has a stronger field in the center of the breasts.



(a) Prototype Coil

(b) New Coil Design

Figure 4.20: B₁ Field Comparison – Transverse Plane

4.3.2 Axillary Coverage Comparison

A side by side visual comparison of the axillary field coverage can be seen in Figure 4.21. In these plots, the B_1 field is plot on the surface of the human body model. It can be seen that the new coil design shows an increase in the axillary coverage of the B_1 field.

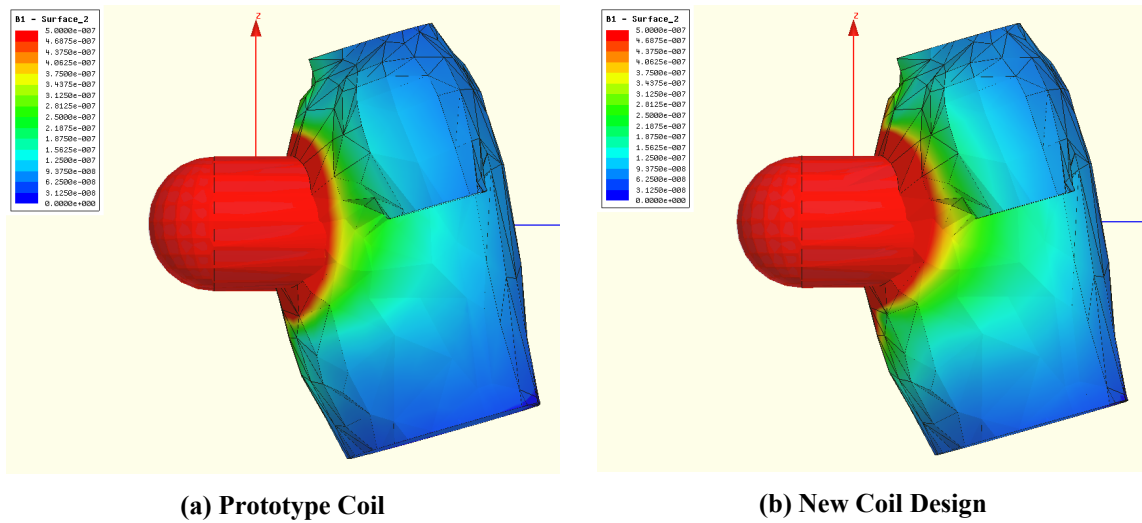


Figure 4.21: Axillary Coverage Comparison

4.3.3 Quadrature Performance Comparison

A comparison of the quadrature difference plot for each design can be seen in Figure 4.22. These plots were both generated using the method described in section 3.6.4. These plots are scaled from 0.5 to 1.5, showing a +/- 50% change in B_1 field strength. For each design, it can be seen that the increase in the B_1 field strength does come close to its theoretical maximum of 41% in the area in the center of each breast. Both quadrature array configurations also result a decrease in field strength in the chest and axilla. The new coil design however, does not suffer as great a decrease in the chest and axilla and when in configured in quadrature should perform better then the prototype design in terms of axillary field coverage.

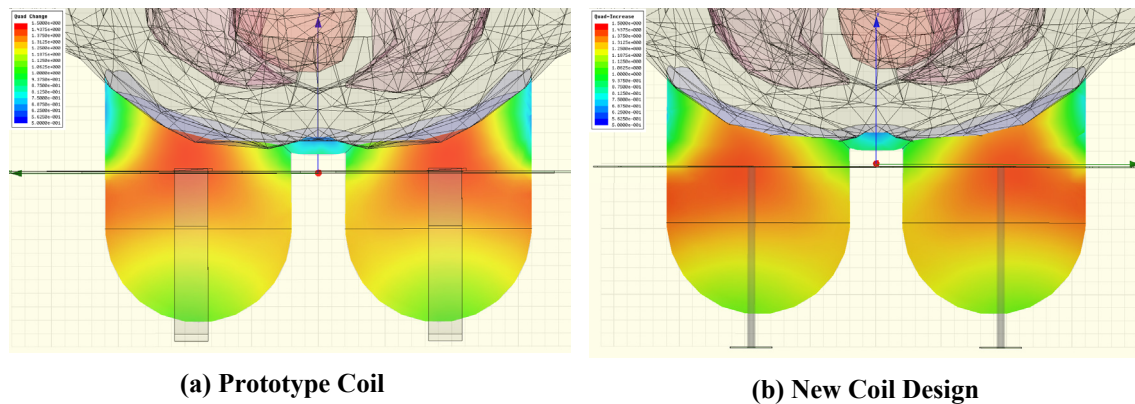


Figure 4.22: Quadrature Field Comparison

Components are linked to the schematic library and are generated and placed into their proper location. Design rule checks for un-routed connections are enabled to prevent errors before manufacturing. There are also extra pads included for soldering temporary SMA connectors during the tuning process. Multiple pads for multiple capacitors are used in place of single capacitors. This allows for a combination of fixed and variable capacitors to simplify the tuning process. The final manufactured PCBs can be seen in Figure 5.3 and Figure 5.4.



Figure 5.3: Manufactured Main PCB

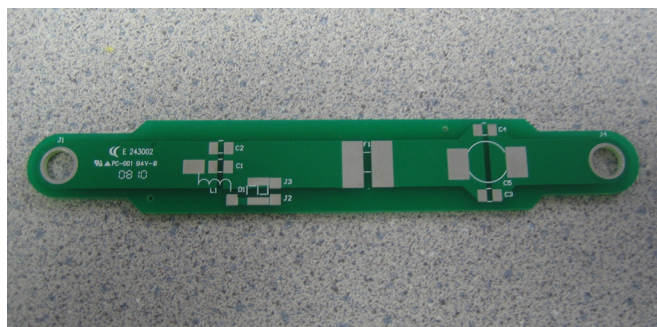


Figure 5.4: Manufactured Strap PCB

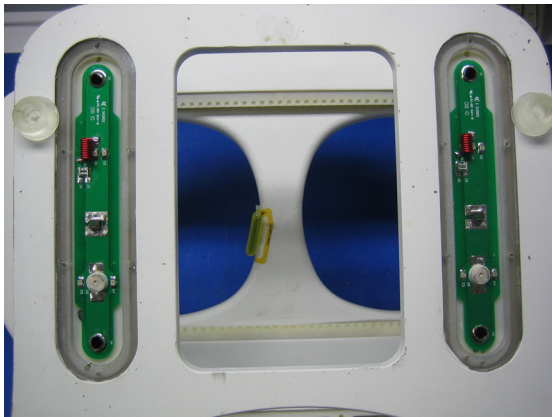
5.2 Construction



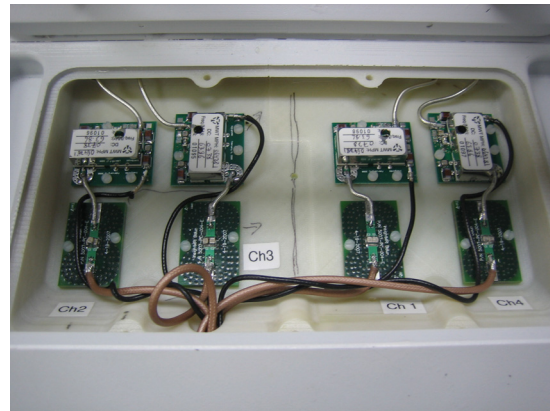
(a) Empty Coil Housing



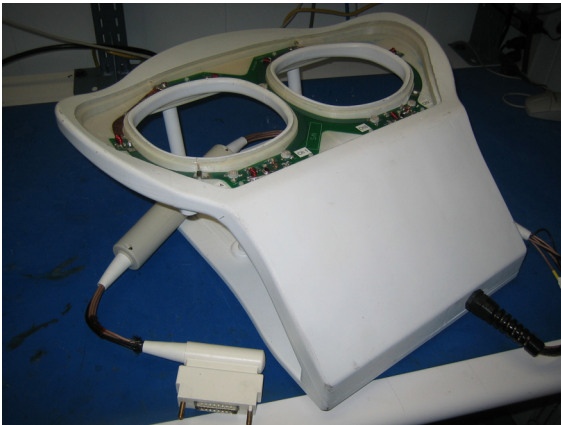
(b) Tuning/Matching Network



(c) Strap PCBs



(d) Pre-Amps and Baluns



(e) Completed Prototype, Cover Open



(f) Completed Prototype

Figure 5.5: Building the New Design Prototype

5.3 Bench Testing and Parameter Recording

The tuning and matching of the coil is an iterative process that can take several iterations to complete. The first step is to tune, match, and decouple the two adjacent ring channels. In Figure 5.6, the left ring is channel 1 and the right ring is channel 2. At this point, the two strap channels contain an open break.

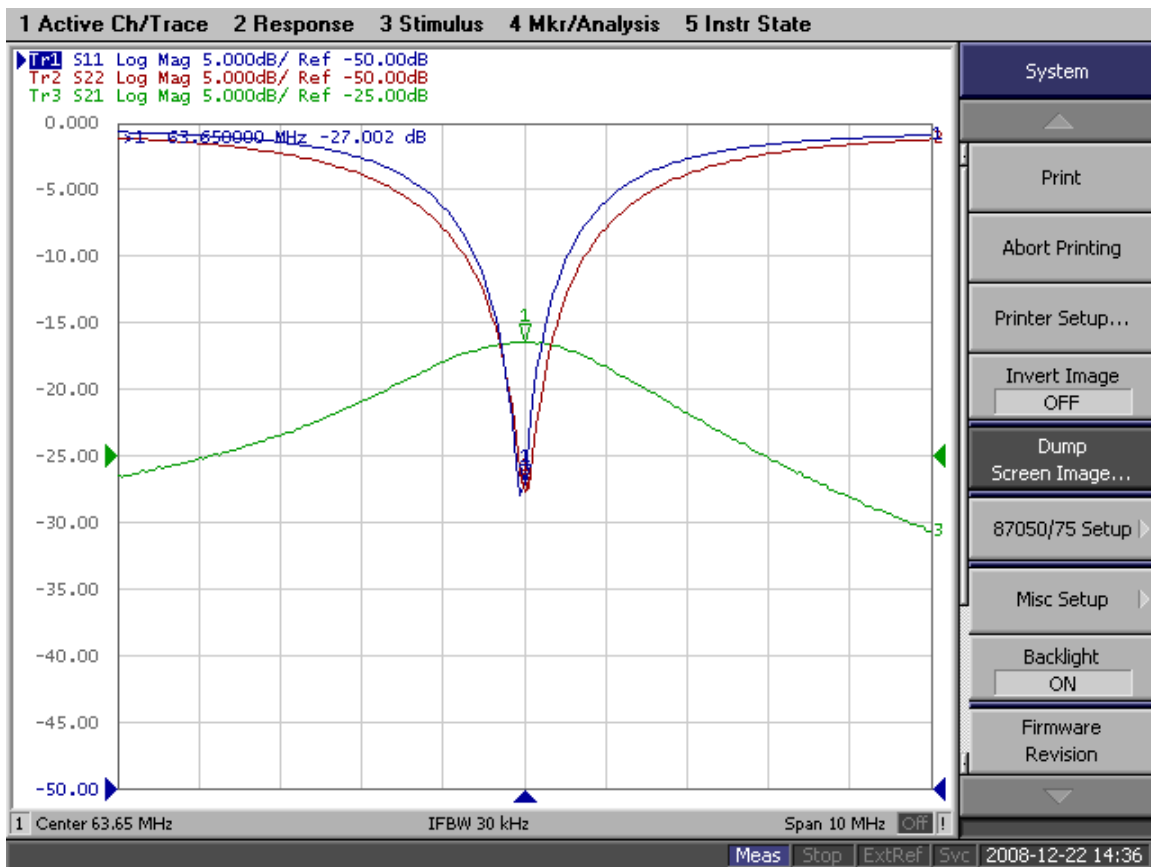


Figure 5.6: S-Parameters of the Two Adjacent Ring Channels

The next step is to tune and match each ring-strap pair. In this case, breaks are made in the right ring and strap channels. In Figure 5.7, the left ring is channel 1, and the right ring is channel 2. Once the left pair has been tuned, matched, and decoupled, the same process is repeated for the right half of the coil.

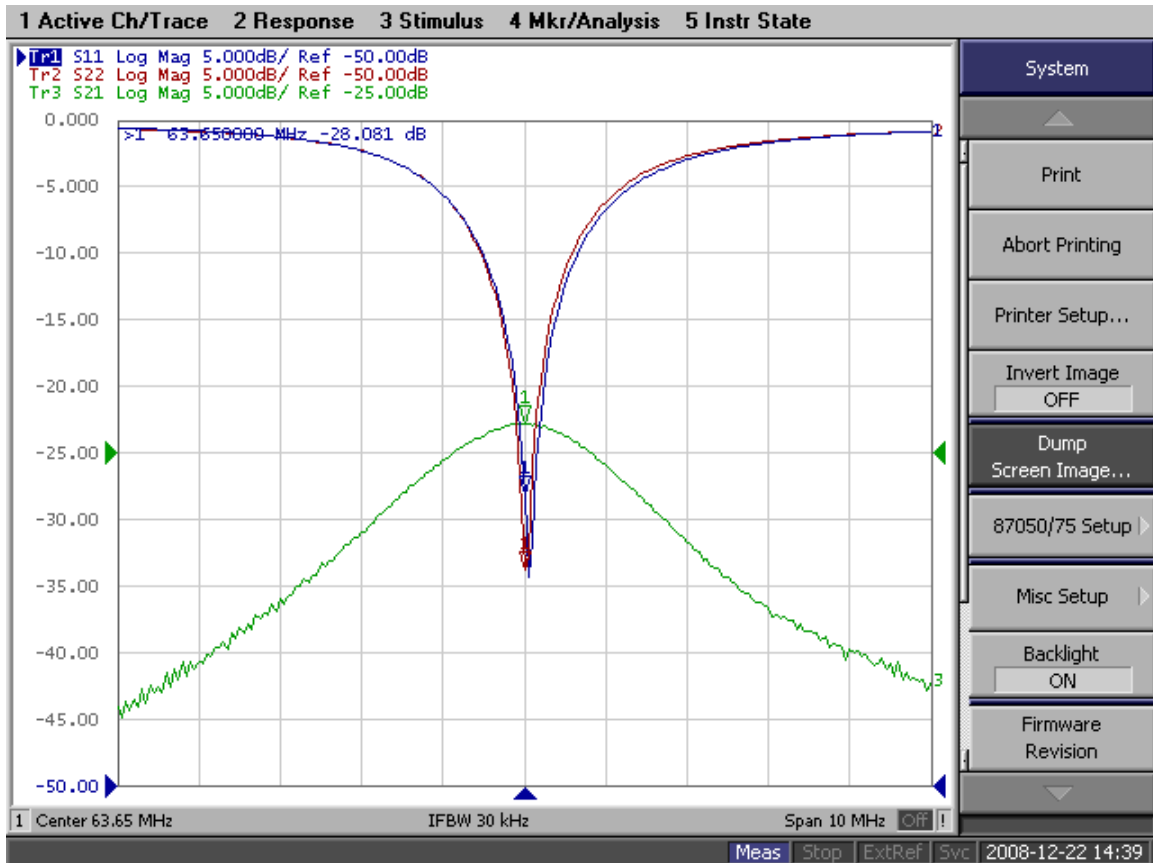


Figure 5.7: S-Parameters of the Left Ring and Strap Channels

After these three coil pairs have been tuned, matched, and decoupled, the process is done over again since adjusting the lumped elements of one ring channel has an effect on the other ring channel. This process is completed until all three coil pairs (ring1-ring2, ring1-strap1, ring2-strap2) are tuned, matched, and decoupled. The final step is too adjust the input impedance of the pre-amps to maximize the pre-amp decoupling effect.

6 Results

6.1 Measured SNR Data

Testing was done in a Siemens Magnetom 1.5T MRI clinical scanner at Mass General Hospital in Boston, MA. Both the original coil prototype and the new design were tested consecutively on the same day. As a load for the coil, two Siemens brand 1L saline phantoms were used. These phantoms are used as a standard load for testing of breast coils used in Siemens scanners.

6.1.1 Prototype Coil

Table 6.1: Prototype Coil Scan Results

	ROI #	Area	Mean	Std Dev	Min	Max
Signal Left	1	4794	1077.816	241.914	540	1556
Signal Right	2	4794	1022.641	227.964	504	1482
Noise	3	7080	14.631	3.405	5	30
SNR Left	73.6666		Homogeneity Left		77.55517	
SNR Right	69.8955		Homogeneity Right		77.70831	
Mean SNR	71.78105		Mean Homogeneity		77.63174	

6.1.2 New Coil Design

Table 6.2: New Design Scan Results

	ROI #	Area	Mean	Std Dev	Min	Max
Signal Left	1	4794	1031.013	222.797	500	1658
Signal Right	2	4794	1164.295	285.534	491	1903
Noise	3	7080	17.092	9.436	0	60
SNR Left	60.32138		Homogeneity Left		78.39048	
SNR Right	68.1193		Homogeneity Right		75.4758	
Mean SNR	64.22034		Mean Homogeneity		76.93314	

6.2 Comparing Simulation to Measured Data

Numerical results from the simulations and measured SNR data from testing are summarized in the following table:

Table 6.3: Simulation and Measured Data Summary

	Prototype Coil	New Coil Design	% Difference
Simulation B1 (Single Value)	$2.74\mu T$	$2.51\mu T$	-8.3 %
Simulation B1 (Mean in Breasts)	$2.56\mu T$	$2.35\mu T$	-8.2 %
Measured SNR	71.78	64.22	-10.5 %

It can be seen that the measured SNR data coincides with the predicted difference in B1 field strength from simulation. Both the measured and predicted data show the original prototype coil to have a greater SNR / B1 Field Strength. The difference found between the simulation and the measured data is within 3%.

7 Conclusion

7.1 Summary

A new design methodology for the simulation of MRI coils has been developed and applied to the redesign of a four channel breast coil array. This new design methodology is based on the commercial FEM software package HFSS. This software package includes new advancements in the fast and accurate prediction of a given structure's S-Parameters. The highly efficient adaptive mesh refinement process reduces computational requirements by automatically adjusting the mesh density to more important features of the model. HFSS also has the ability to create complex models combining small and large details within the same simulation. These models can be created within HFSS geometry system or imported from any commercial CAD tool. The included human body model contains over 300 parts of the body with multiple frequency dependent material parameters that can all be used within a single simulation. With this model, the complex interactions with biological tissues can be easily added to a coil simulation.

While HFSS has many advantages, there are still some steps in the simulation process that HFSS can not do by itself. The need to augment the software's abilities has been identified and successfully implemented by using Matlab to enable the necessary post processing operations to fully simulate a tuned and matched resonating MRI coil array. This includes the ability to transfer calculated values into HFSS to modify the solution vector to generate tuned and matched field plots as well as the ability to import those new field plots back into Matlab for further computation and analysis.

Using this new simulation method, an existing prototype four channel breast coil array was redesigned to fit into a new former while maintaining similar electrical performance. Using this new simulation data, a new design prototype was built, tested and compared to the original prototype model. Results from measured SNR data coincide with predicted values from simulations.

7.2 Further Research

The developed simulation method is not without its limitations. Currently, assumptions need to be made with the decoupling of multiple channels in a coil array when those coils are decoupled using the preamp decoupling method. Since the preamplifiers are not included in the simulation, the current method must assume that there is very strong decoupling between preamp decoupled channels, which is not always accurate.

Another part of the simulation method that could be improved is the interfacing between HFSS and Matlab. Currently there is no automatic way to link data between the two software packages. When creating array field plots, the field plots for each individual channel must be exported separately. To create a single quadrature combined four channel plot, 16 plots need to be manually exported from HFSS for computation within Matlab.

While HFSS is a very powerful tool in determining structure S-Parameters, the use of Ansoft Designer to incorporate the EM simulation from HFSS with circuit and system level components such as baluns and preamplifiers needs to be explored. The latest version of Ansoft Designer has the ability to dynamically link with HFSS to enable rapid system level design. This could also eliminate the need to use Matlab for all of the post-processing operations. Also, the human body model while an excellent biological load model, is only available as a male subject. A more detailed female breast model could be very useful. The model is also in a fixed standing position, making the placement of the model with the coil structure somewhat limited.

The coil design is also another aspect that can still be explored in more depth. Iterations on the design could be run to improve its performance. More research is needed on design parameters like the coil strip width, usage of the copper tubes as resonant structures, as well as the optimal locations for lumped elements such as the tuning capacitors should all be researched more in depth.

8 Bibliography

- [1] J. Als-Nielsen and D. McMorrow, *Elements of Modern X-ray Physics*, Wiley, London, 2001.

- [2] L. McKinnis, *Fundamentals of Musculoskeletal Imaging*, F.A. Davis, Philadelphia, 2005.

- [3] P. J. Keller, *Basic Principles of Magnetic Resonance Imaging*, GE Medical System, June 1988

- [4] Magnetom Symphony, *Proven technology meets innovation*, Siemens AG, Brochure A91100-M2220-D32-1-7600.

- [5] J. Jin, *Electromagnetic Analysis and Design in Magnetic Resonance Imaging*, CRC Press LLC, Florida, 1999.

- [6] M A Bernstein, K F King and X J Zhou, *Handbook of MRI Pulse Sequences*, Elsevier Academic Press, San Diego, 2004

- [7] ReviseMRI.com
<http://www.revisemri.com/images/sliceselection.gif>

- [8] C. Westbrook, C. Roth and J. Talbot, *MRI in Practice*, Wiley-Blackwell, London, 2005

- [9] Chan JHM. *Basic Physics of Magnetic Resonance Imaging*, Bondman Publishing Company, Hong Kong, 1994.
- [10] P. Robitaille and L. Berliner, *Ultra High Field Magnetic Resonance Imaging*, Springer, New York, 2006
- [11] Obi, A., 2003, *A Novel Radio Frequency Coil Design for Breast Cancer Screening in a Magnetic Resonance Imaging System*.
[M.S. Thesis]: Worcester Polytechnic Institute
- [12] Magnetom Symphony, *Proven technology meets innovation*, Siemens AG, Brochure A91100-M2220-D32-1-7600
- [13] R.P. Kleihorst and M.H. Vogel, *Analysis of MRI Systems Including a Human-Body Model*, 2007
- [14] Journal for Sex Research (vol. 24,pp. 177-183), 1987
- [15] L. Wald and S. Wright, *Theory and Application of Array Coils in MR Spectroscopy*, NMR in Biomedicine, Vol. 10, 394-410 (1997)
- [16] *Breast Cancer Screening for Women Ages 40-49*, National Institute of Health Consensus Statement 1997, Bethesda, January 21-23, 15(1)

Appendices

Appendix A: Issues found with the HFSS Lumped RLC Boundary

In HFSS, a lumped element can be defined across any planar break of a structure with the “Lumped RLC Boundary”. The process for defining this boundary condition is the same as for the lumped port. The line of integration is drawn and the value of the lumped element is defined in the dialog box. This method of including lumped elements adds a boundary condition to the full-wave simulation defined as:

$$E_{\tan} = Z_s (\hat{n} \times H_{\tan}) \quad (0.1)$$

Where:

- \hat{n} is the unit vector that is normal to the surface.
- E_{\tan} is the component of the E-field that is tangential to the surface.
- H_{\tan} is the component of the H-field that is tangential to the surface.
- Z_s is the surface impedance of the boundary, $R_s + jX_s$, where
- R_s is the resistance in ohms/square.
- X_s is the reactance in ohms/square.

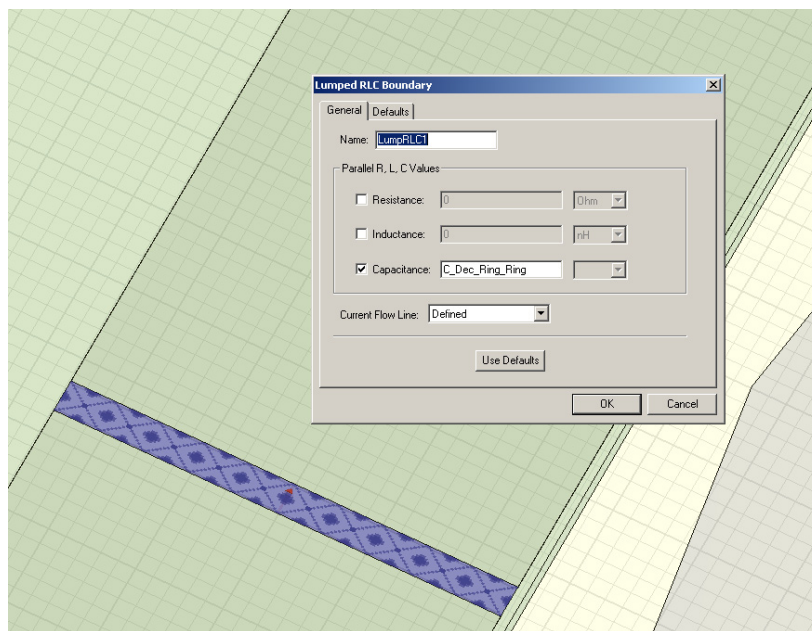


Figure 0.1: Defined Lumped Element Boundary

Simulation Method Utilizing the Lumped RLC Boundary

The structure is developed by parameterization as well as CAD import. The desired breaks in the structure to accommodate lumped elements are added and assigned as a generic $50\ \Omega$ lumped ports. The result of this simulation is an $N \times N$ S-Parameter matrix that describes the system. This matrix data is exported from HFSS and imported into Matlab to be processed on the circuit level to determine lumped element values for the optimal tuning, matching and decoupling of the coils. Once the lumped element values are determined, they can be inserted back into the same HFSS structure model via the Lumped RLC definition. The original generic lumped port definitions are deleted and replaced with LumpedRLC definitions with specific values of capacitors and inductors as found in Matlab. At this point a full frequency sweep of the 4-channel system can be done. It is from this simulation result that field plots can be generated to determine the field strength and coverage in the ROI. A block diagram of this method can be seen in Figure 0.2.

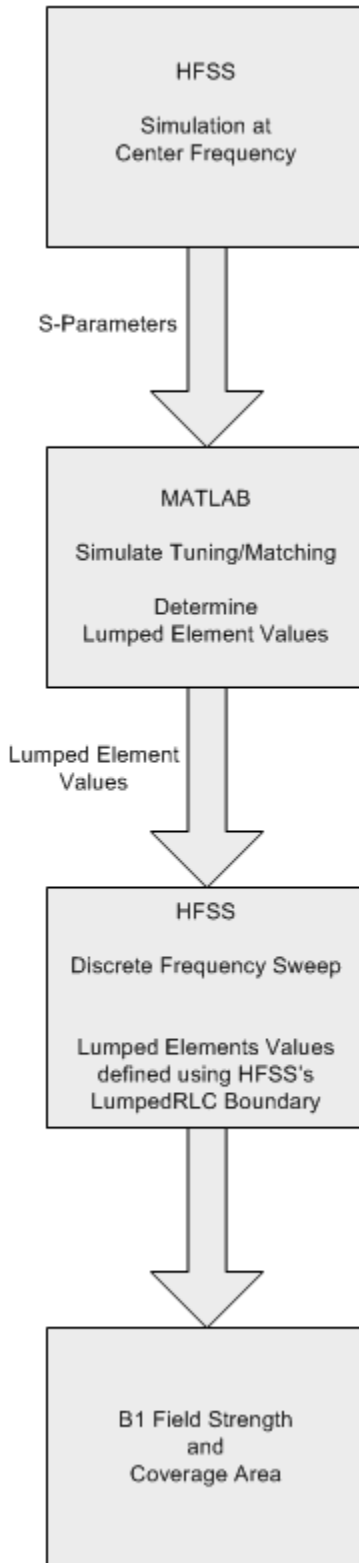


Figure 0.2: Initial Simulation Strategy Block Diagram

Problems with this Method

It was found that the use of Ansoft's "LumpedRLC" boundary condition resulted in many issues described in the following sections that questioned the accuracy of the results. This method is also very time consuming since multiple discrete FEM solutions must be done over a large band. Shown below in Figure 0.3 are the discrete sweep results of the return loss for the ring and strap channels. Each port is re-defined using the LumpedRLC boundary with the lumped element values determined in MATLAB. It can be seen that the results do not agree with the MATLAB predictions seen in Figure 0.4. Both S_{11} and S_{22} are not resonating at the predicted resonant frequency. The levels of matching, as well as quality factor are also much different from the MATLAB prediction.

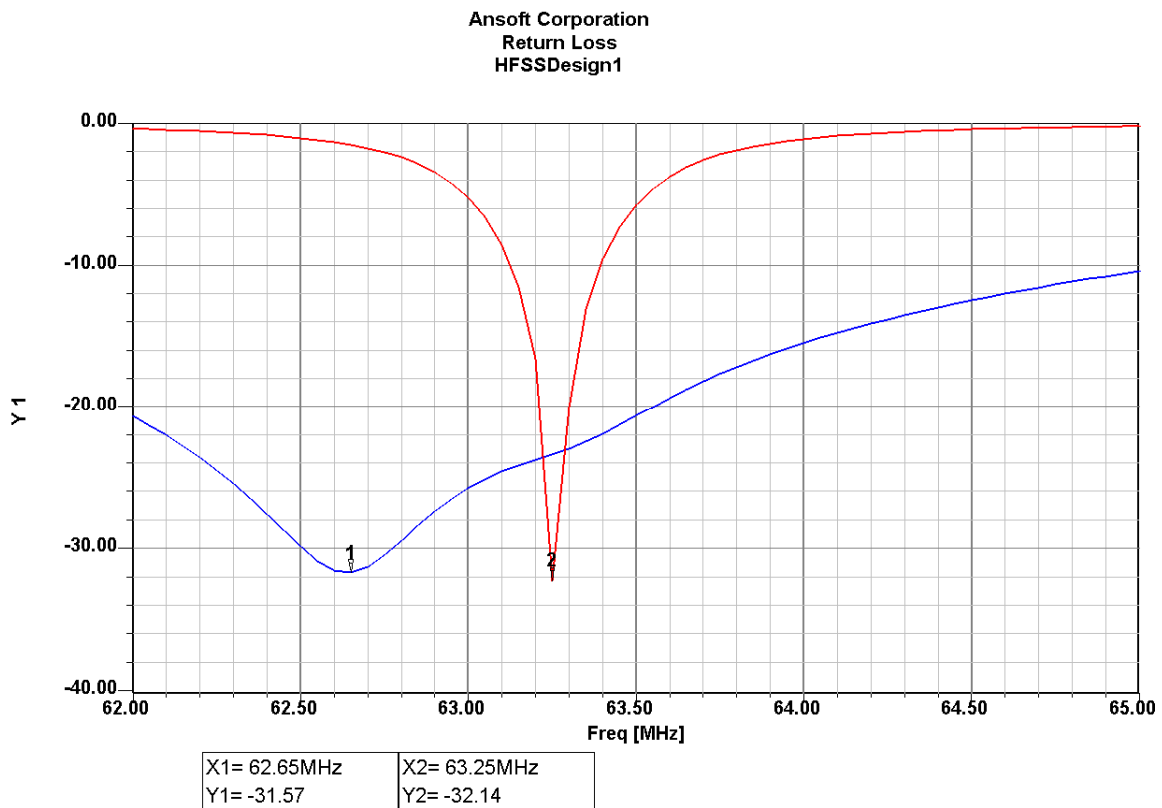


Figure 0.3: HFSS Frequency Sweep Results

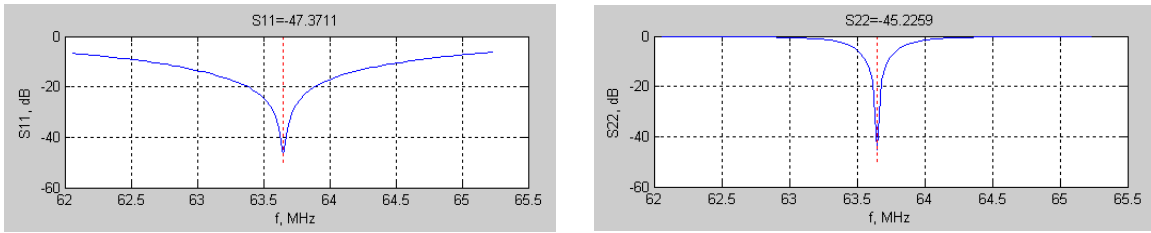


Figure 0.4: MATLAB Frequency Sweep Results

Initially it was thought that the discrepancy arose from the fact that the first single frequency simulation and second discrete sweep simulation use different meshes. HFSS includes the option to use the same mesh in both simulations. The results from this second simulation sweep with the same mesh as the initial simulation yielded no improvement.

To further explore this issue, another program made by Ansoft was used. This program is Ansoft Designer. Ansoft Designer is a circuit simulator, similar to Agilent ADS, but also has the ability to dynamically link with HFSS. For this experiment, the same S-Parameter data generated by HFSS that would be input into MATLAB to determine tuning and matching was now input into Ansoft Designer. Ansoft Designer then performs linear network analysis to determine the new S-Parameters of the system with lumped elements. The goal of this experiment is to determine if the problem is with the way that HFSS simulates lumped elements, or if there if the error is occurring within the MATLAB script that determined the lumped element values.

Shown in Figure 0.5 is the circuit schematic in Ansoft Designer. The black box in the middle is the S-Parameter Data from the HFSS structure simulation. Each of the ports is terminated with its associated lumped elements, except for the four real ports of the system which are the four channels of the coil array and terminated as ports.

To further confirm this, a discrete frequency sweep simulation of the initial 17 port system was done. This data was then used with Ansoft Designer to generate Figure 0.7. Comparing this data once again with Figure 0.4, it can be seen that the results agree with the estimated results from MATLAB.

Normally this type of long discrete sweep is not necessary since the MATLAB code can estimate the sweep outside the center frequency with good accuracy with only the center frequency data input into it. However if the MATLAB code did not exist, this Ansoft Designer simulation shows that Ansoft Designer could be used to perform tuning and matching in the same way as MATLAB. The caveat to this method is that a long HFSS frequency sweep simulation is required for Ansoft Designer to generate an S-Parameter sweep.

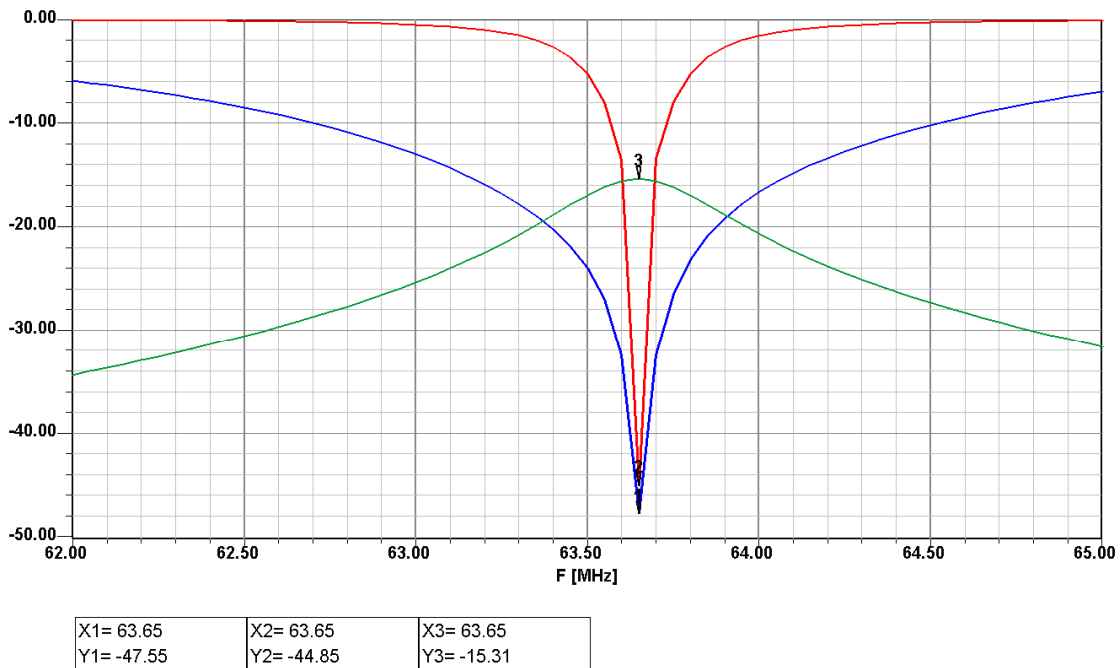


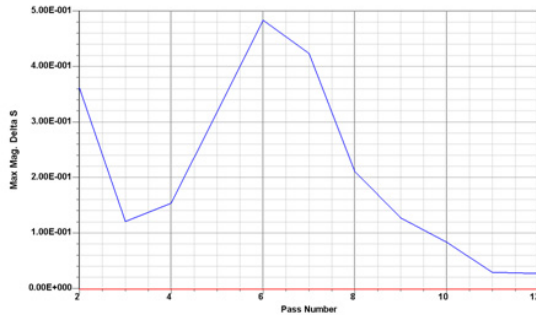
Figure 0.7: Ansoft Designer Simulation Result – Frequency Sweep

Convergence Comparison

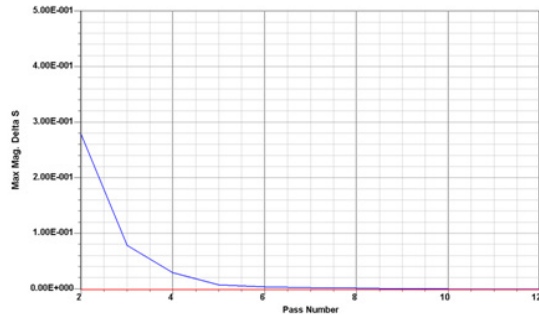
Another major improvement found with the method described in this thesis was the convergence of the solution. The LumpedRLC simulation method produced poor convergence of the simulation. Sample simulations were done using the same model. It can be seen that with the same amount of mesh elements (and RAM resources), the second method imploring ‘LumpedPort’ definitions as opposed to ‘LumpedRLC’ definitions produced more precise results that were able to converge to a smaller Max Mag. Delta S by a factor of 35x.

Pass Number	# Tetrahedra	Max Mag. Delta S
1	45777	N/A
2	52648	0.36199
3	60778	0.12199
4	70373	0.15439
5	81704	0.31811
6	95557	0.48352
7	112253	0.42361
8	132229	0.21235
9	156458	0.128
10	180246	0.084422
11	214350	0.030723
12	245439	0.028033

Pass Number	# Tetrahedra	Max Mag. Delta S
1	47313	N/A
2	54563	0.27834
3	63342	0.079498
4	73949	0.030547
5	86591	0.0087779
6	101639	0.0053562
7	119656	0.0032689
8	141367	0.0025563
9	167417	0.0018119
10	198738	0.0011648
11	236535	0.00089906
12	282000	0.00076634



Initial Method



Improved Method

Figure 0.8: Convergence Comparison of Simulation Methods

Appendix B: Human Body Model Datasets

Fat (ϵ_r):

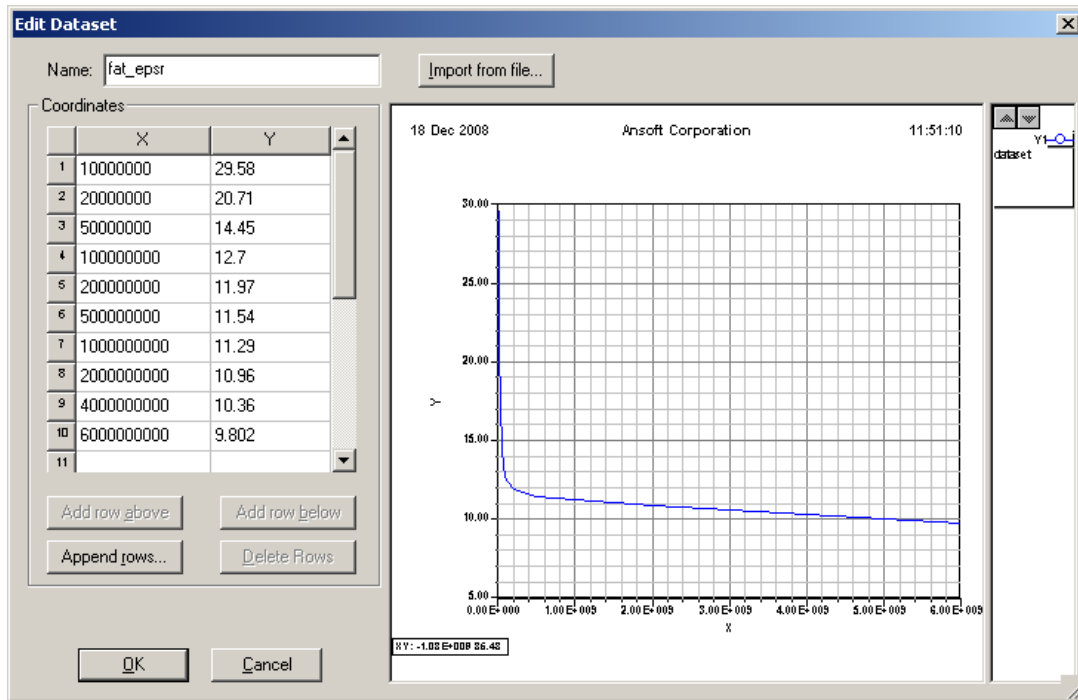


Figure 0.9: Relative Dielectric Constant of Fat vs. Frequency

Fat (σ):

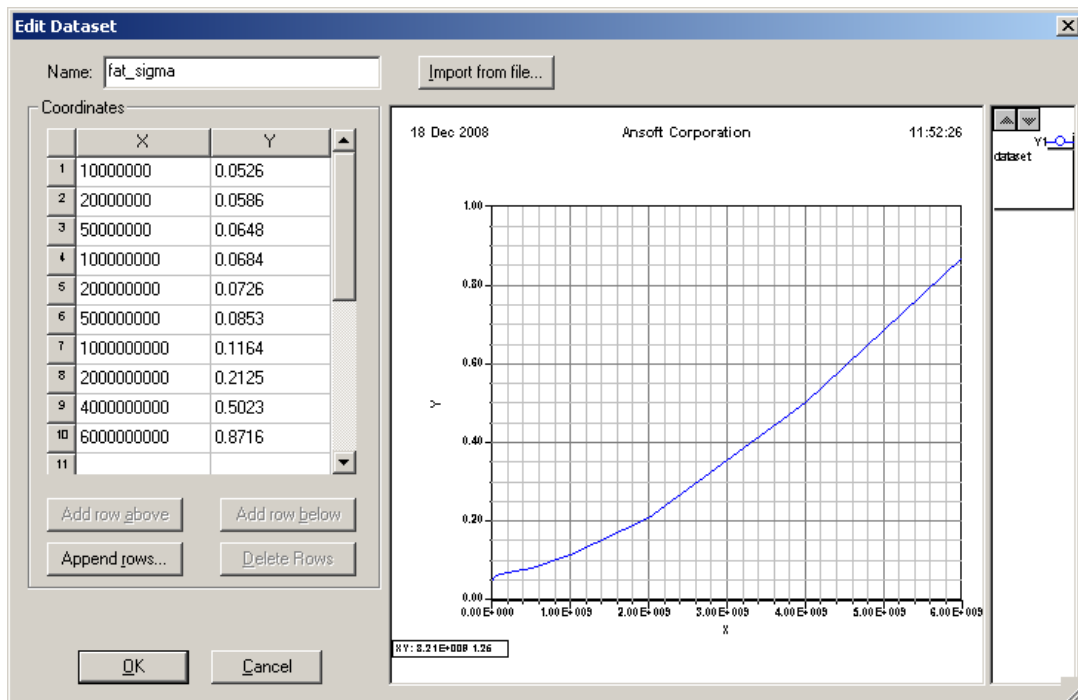


Figure 0.10: Conductivity of Fat vs. Frequency

Heart (ϵ_r):

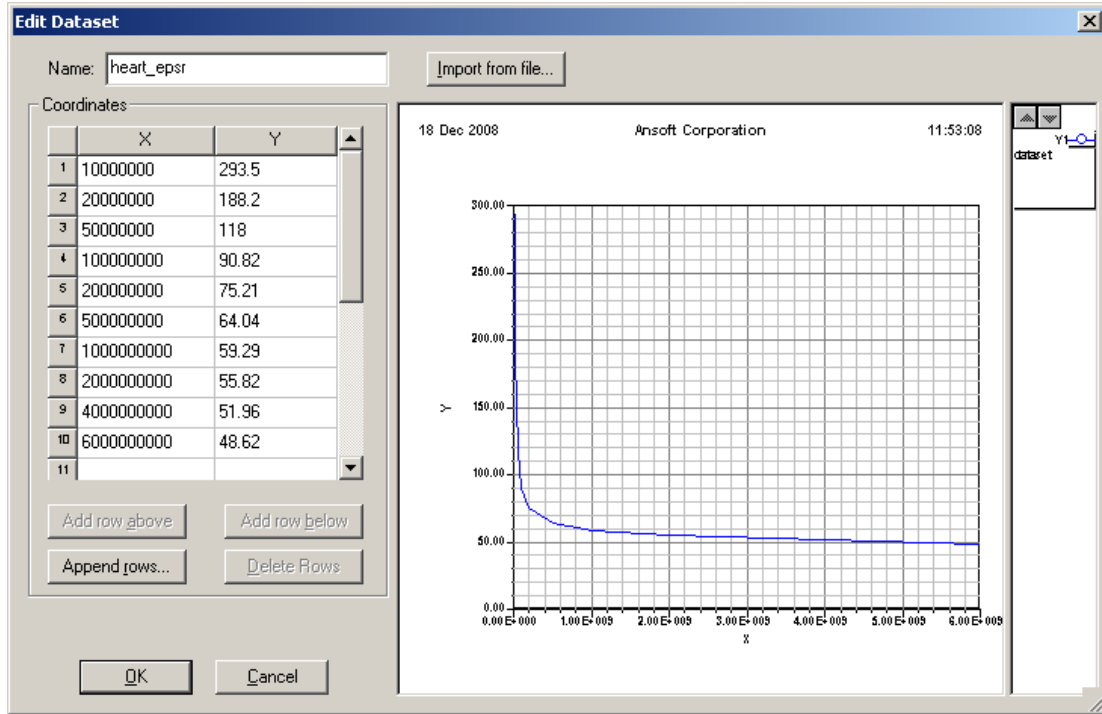


Figure 0.11: Relative Dielectric Constant of the Heart vs. Frequency

Heart (σ):

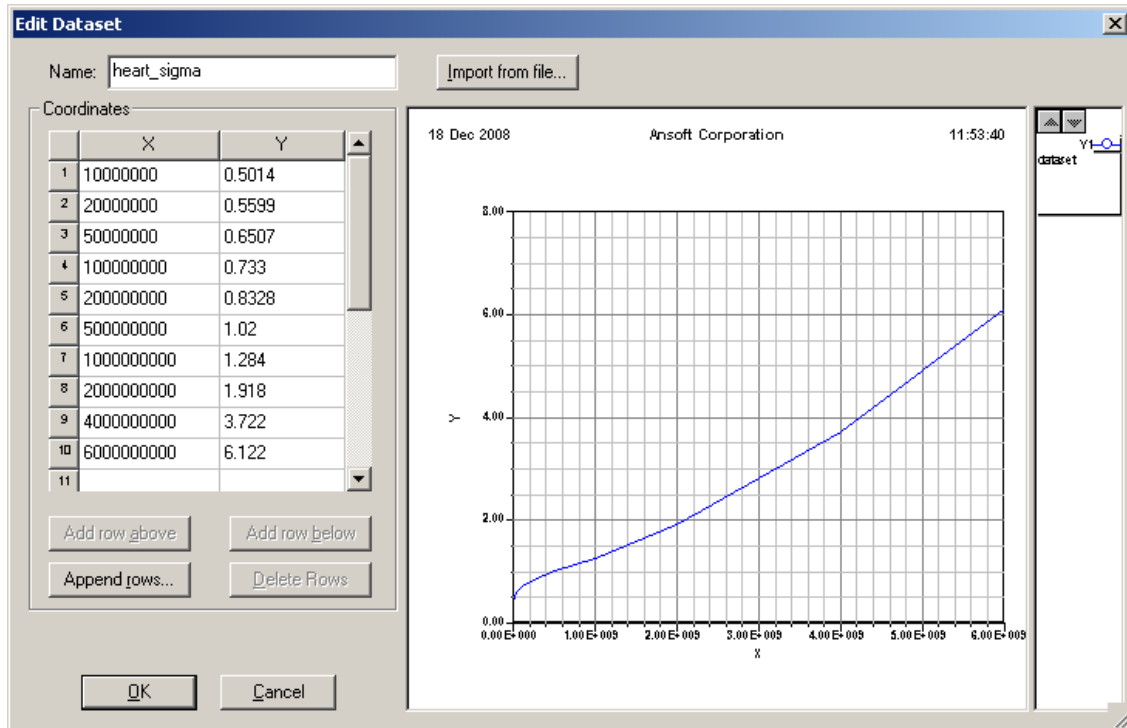


Figure 0.12: Conductivity of the Heart vs. Frequency

Muscle (ϵ_r):

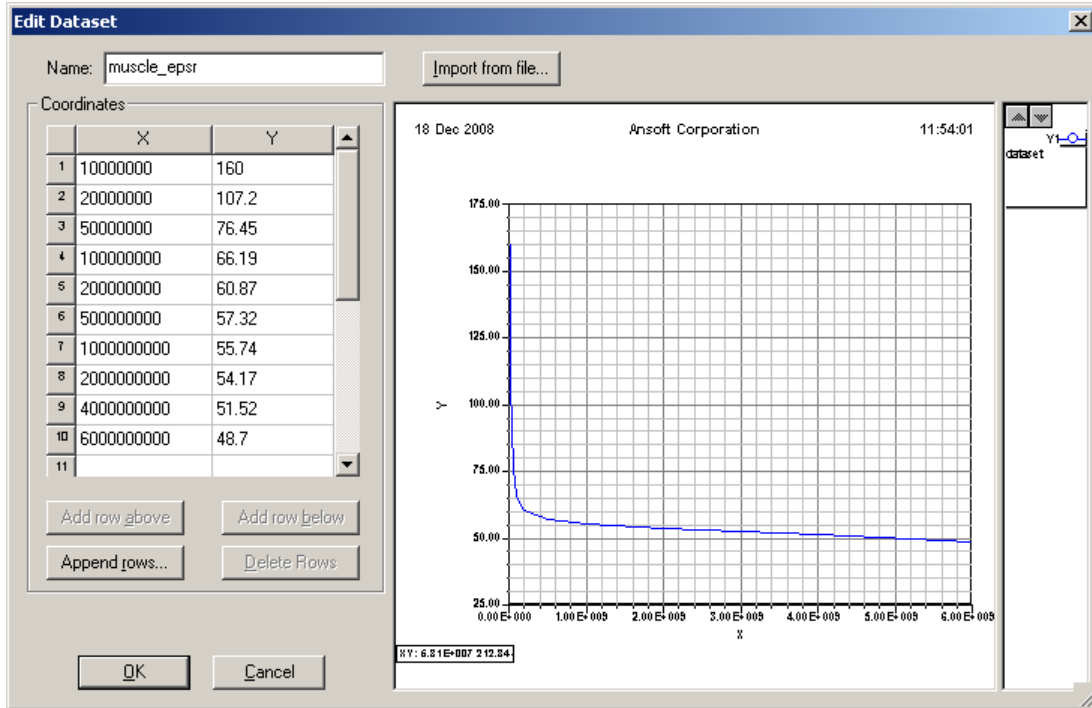


Figure 0.13: Relative Dielectric Constant of Muscle vs. Frequency

Muscle (σ):

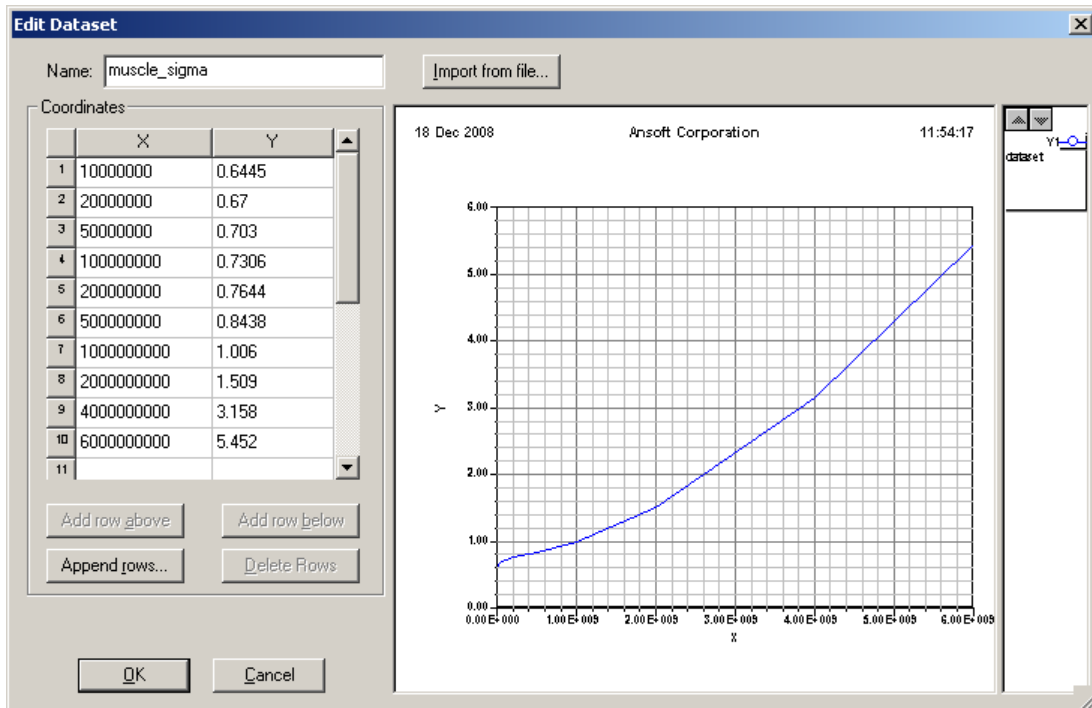


Figure 0.14: Conductivity of Muscle vs. Frequency

Appendix C: Simulation Power Scaling Values

Prototype Coil		Left Ring		Left Strap		Right Ring		Right Strap	
Port #	Lumped Element	Scaling Factor	Offset Phase						
1	C_Dec_Ring_Ring	1.4098	84.2435	2.5266	68.9303	0.0349	96.3607	0.0209	88.2883
2	C_Dec_Ring_Ring	1.3598	-96.1416	2.0790	72.4603	1.3649	83.6509	2.0701	72.8029
3	C_Dec_Ring_Ring	0.0341	-83.2212	0.0204	87.4622	1.4154	-95.9879	2.5243	68.5684
4	C Tune Left strap	0.0199	-94.1766	6.5952	40.5842	0.2727	-153.0008	0.0577	-74.7337
5	C Tune Right Strap	0.2711	27.4209	0.0550	-73.0303	0.0201	82.1695	6.5727	40.5638
6	C Tune Left Ring	1.6468	61.9754	3.0802	47.0172	0.1779	28.1864	0.1031	16.5929
7	C Match Left Ring	1.4828	110.2658	2.3869	73.9252	0.0754	31.5254	0.0607	14.1482
8	C Match Left Ring	1.4549	-69.6173	1.9673	81.8205	0.0916	21.7215	0.1110	13.5821
9	C Tune Left Ring	1.6040	-118.4161	2.5267	50.2351	0.1445	21.2747	0.1352	14.7568
10	L Match Left Ring	0.5593	-154.2127	0.0958	22.6465	0.0242	-13.0503	0.0538	12.5194
11	C Match Left Strap	0.0268	105.8484	4.3038	90.7496	0.0516	31.1925	0.0724	11.6885
12	L Match Left Strap	0.0032	40.2551	0.5039	-173.1428	0.0516	-148.4848	0.0724	-168.0725
13	C Tune Right Ring	0.1726	-158.4463	0.1583	14.1124	1.6113	61.3924	2.5153	50.5922
14	C Match Right Ring	0.0632	-156.6614	0.0860	12.8119	1.4569	110.1738	1.9644	82.1873
15	C Match Right Ring	0.1053	-148.9819	0.0728	14.0257	1.4856	-69.8898	2.3798	73.5987
16	C Tune Right Ring	0.1464	-151.0853	0.0875	15.6780	1.6533	-118.2784	3.0757	46.6907
17	L Match Right Ring	0.0409	-136.8997	0.0170	-170.9882	0.5580	-154.0938	0.0961	-157.9150
18	C Match Right Strap	0.0504	-149.1703	0.0744	11.2420	0.0269	-73.5809	4.2922	90.7307
19	L Match Right Strap	0.0505	31.1538	0.0743	-168.5142	0.0032	-138.9344	0.5049	-173.0921
20	Left Ring	1	0	0	0	0	0	0	0
21	Left Strap	0	0	1	0	0	0	0	0
22	Right Ring	0	0	0	0	1	0	0	0
23	Right Strap	0	0	0	0	0	0	1	0

New Coil Design		Left Ring		Left Strap		Right Ring		Right Strap	
Port #	Lumped Element	Scaling Factor	Offset Phase						
1	C_Dec_Ring_Ring	1.4830	79.6423	2.0742	68.2986	0.0005	122.3149	0.0004	-83.9033
2	C_Dec_Ring_Ring	1.4824	-100.2732	1.8942	71.6588	1.4883	79.6715	1.8875	71.3328
3	C_Dec_Ring_Ring	0.0005	-57.5977	0.0004	-85.6036	1.4891	-100.4217	2.0709	68.5071
4	C_Tune_Left_Strap	0.0099	-102.5874	5.2453	44.2834	0.0082	-141.0044	0.1273	1.2100
5	C_Tune_Left_Strap	0.0018	157.2822	5.2339	44.2690	0.0016	-117.4986	0.1197	0.3157
6	C_Tune_Right_Strap	0.0083	40.4175	0.1279	1.2693	0.0105	81.7822	5.2304	44.2582
7	C_Tune_Right_Strap	0.0013	89.5729	0.1213	0.4838	0.0023	-47.6984	5.2191	44.2437
8	C_Tune_Left_Ring	1.5994	70.1345	2.2375	58.7509	0.0230	42.2790	0.0083	-33.2326
9	C_Tune_Left_Ring	1.6253	-111.3025	2.0768	60.6087	0.0543	-145.4604	0.0064	-33.3268
10	C_Tune_Left_Ring	1.5823	69.9596	2.2209	58.7272	0.0076	96.7929	0.0155	-153.6728
11	C_Tune_Left_Ring	1.6044	-111.5682	2.0627	60.5045	0.1202	22.7505	0.1120	11.7423
12	C_Match_Left_Ring	1.5741	106.7560	1.9595	75.8799	0.0028	161.2079	0.0043	-33.1244
13	C_Match_Left_Ring	1.5737	-73.1997	1.8204	81.2038	0.0533	19.9780	0.0756	9.3937
14	C_Match_Left_Strap	0.0009	88.7764	3.7692	90.1034	0.0142	22.8186	0.0520	2.3149
15	L_Match_Left_Strap	0.0001	27.2531	0.5024	-171.9261	0.0142	-157.0260	0.0520	-177.5795
16	L_Match_Left_Ring	0.5451	-157.2737	0.0382	2.3276	0.0549	18.2216	0.0714	11.8133
17	C_Tune_Right_Ring	0.0552	35.4453	0.0061	-41.9257	1.6322	68.6151	2.0702	60.2520
18	C_Tune_Right_Ring	0.0232	-137.3916	0.0080	-31.9517	1.6063	-109.9522	2.2344	58.9297
19	C_Tune_Right_Ring	0.1375	-156.9754	0.1341	11.8585	1.6115	68.3638	2.0563	60.1506
20	C_Tune_Right_Ring	0.0070	-85.0170	0.0151	-156.8313	1.5894	-110.1310	2.2180	58.9051
21	C_Match_Right_Ring	0.0285	-158.9754	0.0438	8.5933	1.5776	106.6936	1.8104	80.9041
22	C_Match_Right_Ring	0.0107	3.6875	0.0095	-143.5932	1.5796	-73.2757	1.9592	76.1681
23	C_Match_Right_Strap	0.0212	-158.8057	0.0619	3.9887	0.0011	-76.7776	3.7600	90.0750
24	L_Match_Right_Strap	0.0212	21.3422	0.0619	-175.9035	0.0001	-135.6474	0.5031	-171.8708
25	L_Match_Right_Ring	0.0382	16.6722	0.0514	-166.0512	0.5447	-157.3165	0.0373	-178.5843
26	FUSE	1.3838	99.9085	1.9392	88.6329	0.0002	153.8302	0.0003	-67.1507
27	FUSE	0.0002	-26.2442	0.0003	-68.9834	1.3895	-80.1568	1.9361	88.8408
28	FUSE	0.0000	-51.0358	3.6627	90.2090	0.0001	-60.2970	0.0010	90.6860
29	FUSE	0.0001	121.3706	0.0010	90.7735	0.0000	130.2389	3.6540	90.1610
30	Left Ring	1	0	0	0	0	0	0	0
31	Left Strap	0	0	1	0	0	0	0	0
32	Right Ring	0	0	0	0	1	0	0	0
33	Right Strap	0	0	0	0	0	0	1	0